UNIVERSITY OF OKLAHOMA

GRADUATE COLLEGE

ADVANCES IN UNDERSTANDING POLYMER CHEMICAL RECYCLING REACTIONS

A DISSERTATION

SUBMITTED TO THE GRADUATE FACULTY

in partial fulfillment of the requirements for the

Degree of

DOCTOR OF PHILOSOPHY

By

ANA CAROLINA JERDY
Norman, Oklahoma
2023

ADVANCES IN UNDERSTANDING POLYMER CHEMICAL RECYCLING REACTIONS

A DISSERTATION APPROVED FOR THE

SCHOOL OF SUSTAINABLE CHEMICAL, BIOLOGICAL AND MATERIALS ENGINEERING

BY THE COMMITTEE CONSISTING OF

Dr. Steven Crossley, Chair

Dr. Lance Lobban

Dr. Daniel Resasco

Dr. Bin Wang

Dr. Mark Nanny

ACKNOWLEDGEMENTS

First, I would like to thank my research advisor, Prof. Steven Crossley. His unwavering support for his students not only allowed me to complete my doctoral journey, but also taught me to always be kind to others. He allowed me to pursue research directions that I thought were interesting, and always helped with great discussions and ideas. I am very grateful for having worked in his group and could not have asked for a better advisor.

I would also like to thank the members of my committee: Prof. Lance Lobban, for all the support, and the careful manuscript reviews; Prof. Daniel Resasco, for teaching me the fundamentals of kinetics and catalysis, and for always giving me ideas; Prof. Bin Wang, for the insights during meetings; and Prof. Mark Nanny, for his willingness to be part of my committee.

I thank the support of the members of my research group, from helping with equipment troubleshooting to discussing research: Han Chau, Alejandra Gomez, Caleb Bavlnka, Luis Trevisi, Reda Bababrik, Tram Pham, Ismaeel Alalq, Nabihan Rahman, and Nilson de Paula. In addition, I express my appreciation for my industrial collaborators, who assisted me with discussions, manuscript reviewing, samples and even experiments when it was necessary: Miguel Gonzalez, Masud Monwar, Steve Kelly, Ron Abbott, David Soules, and Pascale Attalah.

Finally, I would like to acknowledge my partner and best friend, Elton Lima Correia. Thank you for making things easier when times were hard. Thanks for discussing my research with me and listening to my presentations. I would not have gotten this far without your support. I am so grateful for being able to share my life with you.

TABLE OF CONTENTS

LIST OF TABLES

LIST OF FIGURES

ABSTRACT

Plastics revolutionized the world since the beginning of their mass production in the 1950's. Packaging, construction, and many other industries successfully substituted materials for plastics, or found in these novel materials a new business application. Plastic production – as well as demand – has continuously grown in the past decades. Consequently, the amount of waste generated has also increased. Without an effective way to give new life to plastic waste, discarded plastic has accumulated in earth and marine environments. Accumulation of such waste is detrimental to many forms of life, and a better way to address waste is necessary.

Mechanical recycling efforts began in the 1970's, consisting of sorting, washing, grinding, melting, and reshaping waste plastic. Although a good alternative for well-sorted polymer waste, it is not applicable to materials such as multilayer films or thermoset polymers. As such, mechanical recycling currently corresponds to less than 10% of the total plastic production. On top of that, this thermal process lowers the quality of the final products in such a way that products can only be recycled a limited number of times before their properties do not meet minimum standards, which inevitably leads to waste. Therefore, it has become clear that mechanical recycling alone is not able to tackle the challenge of waste plastics.

In order to complement mechanical recycling technologies, a new approach called chemical recycling is currently being developed. This process consists in selectively cleaving polymer molecules back into their building blocks, which are called monomers, that can then be manufactured into pristine plastic. There are many advantages involving the use of chemical recycling routes, such as that they yield products with identical performance to polymers manufactured from traditional feedstocks. There is even more potential to be unraveled as

chemical upcycling routes are also being investigated. As opposed to converting polymers back to monomers, this process consists in decomposing polymer molecules into products which are more valuable than monomers, such as gasoline, diesel or alkyl-aromatics. Still, there are many challenges to be overcome, such as the fact that performance additives are often present in plastics, augmenting the recycling complexity.

These depolymerization reactions may be carried out in the absence or presence of catalysts. However, it is important to highlight that most catalyst technologies available today were originally designed to convert molecules which are orders of magnitude lower in molecular weight than plastic waste feedstock. Hence, there is a need to understand how this new feedstock will interact with traditional catalysts, and to design new catalysts to optimize polymer conversion.

This work is dedicated to improving understanding of these novel chemical recycling and upcycling reactions. Here, we discuss the impact that common polymer additives may have when they are present in a polyolefin melt undergoing pyrolysis or catalytic decomposition. This is fundamental to grasp how real-world polymer products will behave when subject to these processes, since all commercial plastic products inherently contain additives. Next, we unveil how a common additive may deposit and alter the activity of different pore-sized catalysts. Additionally, we investigate the role that polymer structures may play in the decomposition of polymers over porous heterogeneous catalysts. Finally, new catalyst design approaches are discussed to improve polymer-catalyst interaction in order to increase perceived rates of reaction. Insights from this work may help inform the industry and be one more step towards the development of optimized chemical recycling processes, which will allow for a more circular plastics economy.

Keywords – chemical recycling, chemical upcycling, polyethylene, catalytic pyrolysis

Chapter 1: Introduction

Plastics revolutionized the industry and consumers everyday lives since the beginning of its mass production in 1950. [1] Advantages such as durability, low weight, and low cost to produce [2] made plastics be the new material of choice for many industrial applications. Packaging, construction, and many other industries successfully substituted materials for plastics, or found in these novel materials a new business application. The wide range of applications of all kinds of plastics and ever-growing demand have boosted production throughout the years. Currently, the global plastic production is estimated to be about 400 million tons per year [3], and it is estimated to double within the next 16 years.[4]

Plastics are polymers, which are synthesized mostly from petrochemical feedstocks. It can be argued that the use of plastics has improved many aspects of businesses and even decreased environmental impacts. For example, their intrinsic light weight has diminished transportation loads, reducing costs and fuel usage, and consequently resulting in lower carbon emissions.[5] Food packaging has also been forever transformed by the use of plastic materials, increasing the shelf life of products and improving food consumption safety.

However, continued increases in plastic production and constant discarding of such materials are resulting in terrible consequences for the environment. Thus, it is much necessary to change the current approach with plastic waste.

1.1. Motivation and goals

Plastics have created negative impacts on the environment primarily due to their forementioned durability and improper disposal. Most plastic materials can linger in the

environment for hundreds of years.[6] In aquatic ecosystems, plastic residue can be ingested by wildlife and get entangled with animals. The presence of such debris in aquatic environments may cause transport of non-native species, physical changes to habitats and even fatalities.[7] In terrestrial environments, the presence of plastic can contaminate soils. Furthermore, any additives contained in these materials can leach into water or soil, posing hazards to wildlife.[8]

Moreover, microplastics can easily spread everywhere and become incorporated into the food chain. Microplastics consist of any plastic residue with size smaller than 5 mm.[9] They have been found in water bodies, soil, human tissues, and even in the air.[10] Although the effects of microplastics in humans has not yet been fully assessed, it is known that they may cause detrimental effects to aquatic life.[8]

Currently, the vast majority of plastic waste is either recycled, incinerated or discarded in landfills, open dumps, or the open environment.[11] Discarding rates have been decreasing since 1980, with incineration and recycling becoming more popular. One estimate is that in 2017, about 55% of global plastic waste was discarded, whereas 25% was incinerated and 20% was recycled.[11]

Recycled plastic currently consists mainly of mechanical recycling. This process melts the plastic waste and remodels it into a new product. However, this thermal process leads to changes in the molecular structure of the polymers – chain scission, branching and crosslinking can occur.[12] These chain modification processes may result in lower molecular weights. Due to this, mechanical recycling consistently faces challenges with cost, worsened mechanical properties, and inconsistent quality of products.[13] On top of that, mechanically recycling plastic products only delays the disposal, rather than eliminating it.

In this context, new approaches to address plastic waste are being developed, which can be categorized into chemical recycling or chemical upcycling. Chemical recycling consists of technologies to decompose plastic waste into their original constituent molecules, so that new, pristine plastic can be synthesized from them. With this approach, the chemically recycled product has the exact same properties as polymers made from the traditional feedstocks.

Since generating monomers from polymers at high yields is not an easy task to accomplish in most cases, another strategy is to chemically transform polymer waste into other, higher value materials – which is called chemical upcycling. Polymers can be upcycled into products such as fuels[14], lubricants[15], or surfactants[16]. This strategy addresses plastic waste while providing an alternative feedstock to already established processes in the industry. Figure 1.1 illustrates the integration of chemical recycling and mechanical recycling to tackle the challenge of plastic waste accumulation.

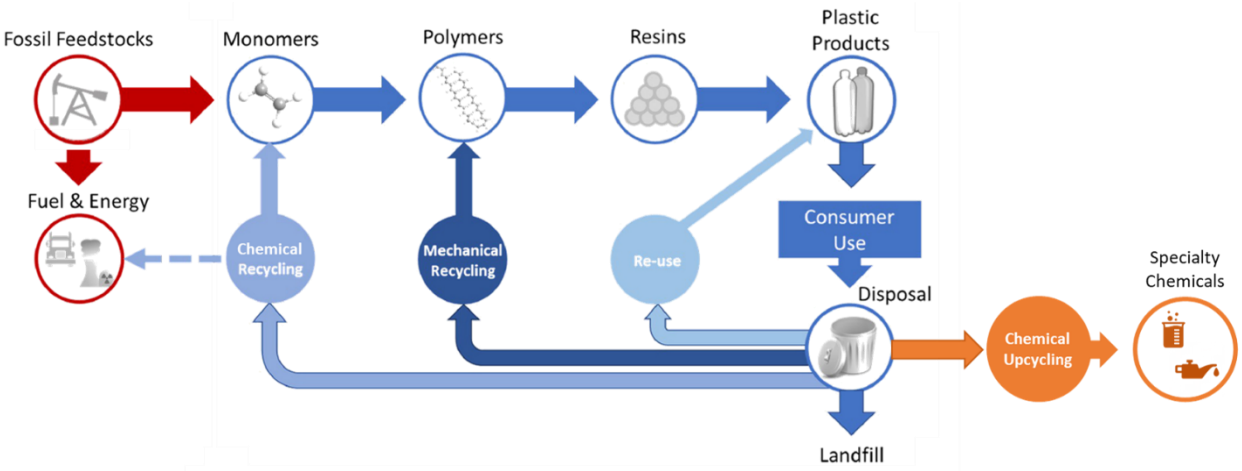

Figure 1.1. Scheme of the combination of mechanical recycling and chemical recycling/upcycling approaches to minimize the overall plastic waste generated. Modified from Ref [17].

Both chemical recycling and upcycling pathways can happen in the absence or presence of catalysts. The goal of this work is to fundamentally understand different aspects of chemical recycling/upcycling reactions, such as the effect of polymer additives or the role that branching can play in the decomposition of polymers, thermally and catalytically. Better understanding these reactions can help inform the industry and assist in designing effective processes to give new life to plastic waste.

1.2. Polymers' structure and challenges

The word *polymer* means "many parts". Polymers are macromolecules comprised of repeating units of smaller molecules – called *monomers*. Polymers can encompass many kinds of materials, ranging from synthetic plastics such as polypropylene to naturally occurring materials such as natural rubber.

In this work, two polymers were investigated: polyethylene (PE) and polystyrene (PS). Their molecular structures can be found in Figure 1.2. Both these plastics are used in a wide range of applications, including packaging, bottles, bags, plastic toys, among others. Polyethylene is commonly described using acronyms referring to their branching characteristics, such as HDPE (high density polyethylene, linear structures containing very few tertiary carbons), LDPE (low density polyethylene, branched structures) or LLDPE (linear low density polyethylene, linear structures with the presence of controlled size branches). A visual representation of the structure of these PE types is shown in Figure 1.3.

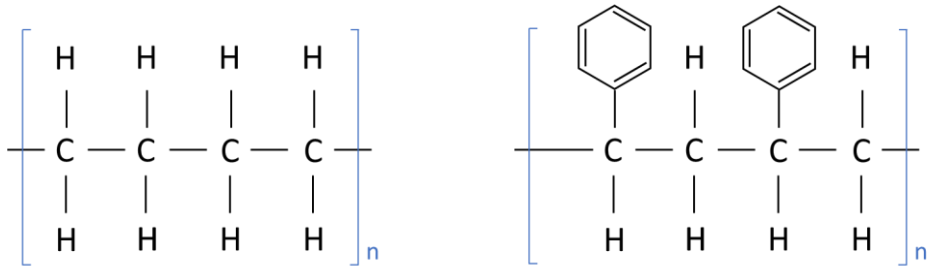

Figure 1.2. Molecular structures of polyethylene (left) and polystyrene (right).

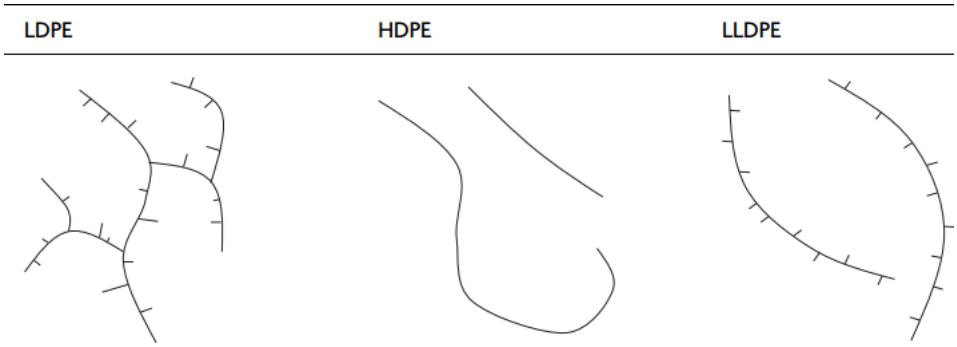

Figure 1.3. Polyethylene types: low density polyethylene (LDPE), high density polyethylene (HPDE), linear low density polyethylene (LLDPE). Source: Ref [18].

In general, polymer chains are randomly entangled in amorphous structures when in solid state. However, polymers can generate different microstructures, that is, ways that these long chains can be arranged in space, depending on their molecular structure. These conformations in space can, in turn, yield unique properties. For example, HDPE tends to form microcrystalline domains due to its lack of steric hindrance.[19] The higher the degree of crystallinity of a polymer, the higher its density and resistance to plastic deformation (hardness).[20] Another example of structure-property relationship on polymers is that crosslinked polymers (in which branches are chemically bonded, forming a three-dimensional structure) become more elastic.[21]

As the temperature of a plastic sample is increased, its amorphous domains become less hard and enter a viscous state when the *glass transition temperature* is achieved.[22] This is a reversible transition that takes place at temperatures below the melting point of the material. As the temperature is further increased and the melting point is achieved, the polymer chains form what is called a polymer melt – a viscous liquid, commonly non-Newtonian, consisting of somewhat entangled macromolecules that can elongate and align with flow given a shear stress.[23]

At higher temperatures and in the absence of oxygen, *pyrolysis* begins to happen. Pyrolysis consists of the thermal decomposition of materials. Polymer pyrolysis occurs by a complex network of free-radical reactions, and often results in a very broad product distribution profile, yielding very diverse products. [24] This reaction consists of initiation, propagation, and termination steps. Initiation takes place when enough energy is provided so that there is a homolytic bond cleavage, creating two radicals.[25] Propagation can involve unzipping (end-chain β-scission reactions), backbiting (intramolecular hydrogen transfer and subsequent mid-chain β-scission) or random scission (intermolecular hydrogen transfer followed by mid-chain β-scission).[26] Finally, termination steps consist in either two free-radicals recombining or disproportionation. Figure 1.4 displays pyrolysis reaction steps for high density polyethylene.

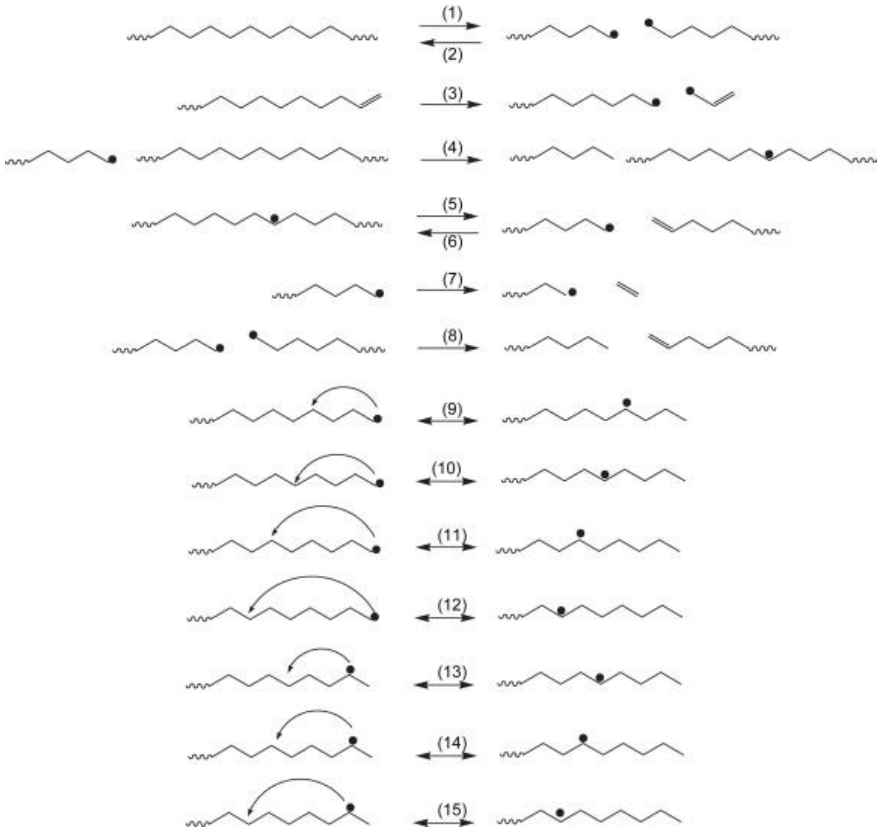

Figure 1.4. Pyrolysis steps for HDPE decomposition. (1) Bond fission, (2) radical recombination, (3) allyl bond fission, (4) hydrogen abstraction, (5) mid-chain β-scission, (6) radical addition, (7) end-chain β-scission, (8) disproportionation, (9-15) hydrogen shift reactions. Source: Ref. [26].

Given the complex rheological nature of polymer melts, the use of catalysts to convert polymers can be quite challenging. The high molecular weights associated with plastics render these molecules extremely prone to being diffusion-limited, that is, when the rate of diffusion to the catalyst surface or into the catalyst pores is slower than the rate of the surface reaction itself. More on that topic will be discussed throughout the document.

1.3. Catalysts nature and activity

Catalysts are materials that modify rates of reaction without being consumed in the process. This usually happens by providing a new chemical pathway for the reaction to happen.[27]

Catalysts may be homogeneous or heterogeneous, meaning that the catalyst can be in the same phase or in a different phase than the reactants and products. Typically, heterogeneous catalysts are solid while reactants and products are gas or liquid phase. The use of heterogeneous catalysts provides an easy separation of the product mixture from the catalyst, which is an important economic advantage since catalysts are often valuable and their reuse is many times necessary.[27]

Heterogeneous catalysts can be acids, metals, oxides, sulfides, carbides, among others. In this work, the main catalysts used are solid acids and metals, and all reactions involve hydrocarbons as feedstock. Hence, the catalytic reactions described in this dissertation may involve: i) cracking over acid sites, ii) hydrogenolysis over metal sites, and iii) hydrocracking over bifunctional acid-metal catalysts.

1.3.1. Hydrocarbon cracking over Brønsted acid sites

Cracking reactions consist of the cleavage of C-C bonds to yield shorter chains of hydrocarbons. One notable industrial application for this reaction is the fluidized catalytic cracking (FCC) process in oil refineries, in which vacuum gas oil (VGO), composed of long hydrocarbon chains, is cracked down to gasoline range molecules.

For many years, it was thought that reactions over solid acids occurred via carbenium ion intermediates, as is the case with acid-catalyzed reactions in liquids.[28] However, ab initio quantum chemical calculations have shown that such carbocations in solid acid catalysts are, in fact, transition states; alkoxy species formed by the hydrocarbon and the catalyst were found to be the intermediates in this process.[29]

When starting from an alkane, these molecules adsorb and receive a proton from the Brønsted acid site. This generates a non-classical pentacoordinated *carbonium ion*, which is

extremely unstable and quickly undergoes either protolytic cracking or dehydrogenation. Protolytic cracking gives rise to an alkane and a *carbenium ion*, whereas the dehydrogenation route results in a carbenium ion and H_2. As far as cracking reactions go, carbenium ions can: i) undergo β-scission, which is a C-C bond scission resulting in an olefin and another carbenium ion; ii) undergo hydride transfer, resulting in an alkane; or iii) desorb as olefins. [30-32] Figure 1.5 summarizes possible pathways for alkane cracking reactions.

When the reaction starts from an alkene, protonation by the Brønsted acid site results directly in a carbenium ion. Another possible pathway for the formation of carbenium ions is the abstraction of a proton from an alkane by a Lewis acid site.[30] Also, oligomerization and isomerization can also readily occur in these acid environments.

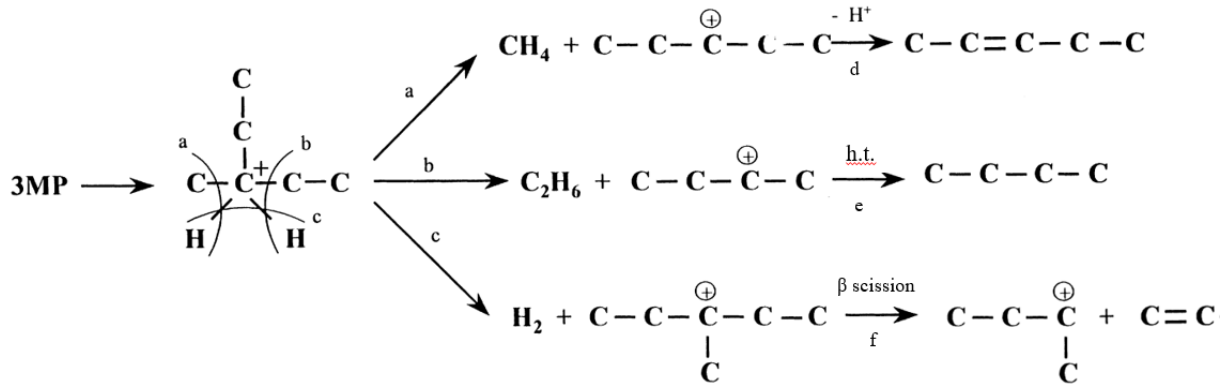

Figure 1.5. Cracking pathways for 3-methylpentane. After protonation into a pentacoordinated carbonium ion, it can undergo protolytic cracking (a, b) or dehydrogenation (c). All the carbonium ion pathways result in a carbenium ion, which can (d) desorb as an olefin, (e) receive hydride from another species, or (f) undergo β-scission. Figure modified from Ref. [30].

1.3.1.1. Zeolites

Zeolites are crystalline microporous solid acids widely used in industry for a variety of processes, such as cracking and alkylation. Their controlled pore sizes allow for a fine tuning of

product distribution control due to the concept of *shape selectivity*. Their constrained pore sizes will only allow for certain reactants and products to diffuse in and out of their pores, respectively. On top of that, their constrained voids generate *confinement effects*, as van der Waals interactions can modify transition states in a way to favor some and reject others.[33]

Zeolites are composed of tetrahedral silica and alumina, can happen naturally or be synthesized. They are mainly distinguished by the geometry of their structures and their Si/Al ratios. Lower Si/Al ratios zeolites are more acidic, since the Brønsted acid sites are formed due to a charge imbalance resulting from Al addition to the framework lattice.[34] Examples of framework types can be found in Figure 1.6.

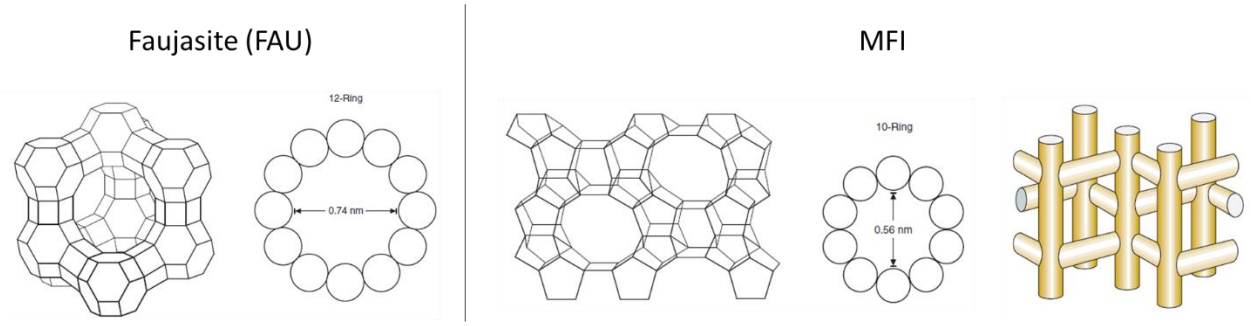

Figure 1.6. Examples of zeolite framework structures and their pore sizes: Zeolite Y (FAU) and ZSM-5 (MFI). Source: Ref. [34].

1.3.2. Hydrogenolysis over metal sites

Hydrogenolysis consists of the scission of C-C bonds and the formation of C-H bonds in a system containing hydrocarbons and H_2. It breaks long hydrocarbons down to shorter hydrocarbons, mostly alkanes. As opposed to cracking over acid sites, hydrogenolysis is an exothermic reaction due to the formation of C-H bonds. These reactions are catalyzed by a variety of transition metals, such as Ru, Pt, Rh, and Ir, on which H_2 can readily be dissociated.

When the alkane adsorbs onto the metal surface, the C-C bonds weaken by the formation of surface intermediates that replace the C-H bond by a C-metal bond, increasing the number of electrons in antibonding orbitals in C-C bonds.[35] C-C bond scission then happens by a reactive surface intermediate when two neighboring carbons are bonded to the metal.[36] The position where the C-C bond cleavage happens depends on factors such as temperature, alkane and H_2 partial pressures, coordination numbers of exposed metal atoms and their chemical identity.[37] Hydrogenolysis is thermodynamically disfavored by high H_2 pressures since the transition state formation consists of dehydrogenation of hydrocarbons. An example for hydrogenolysis reaction steps can be found in Figure 1.7.

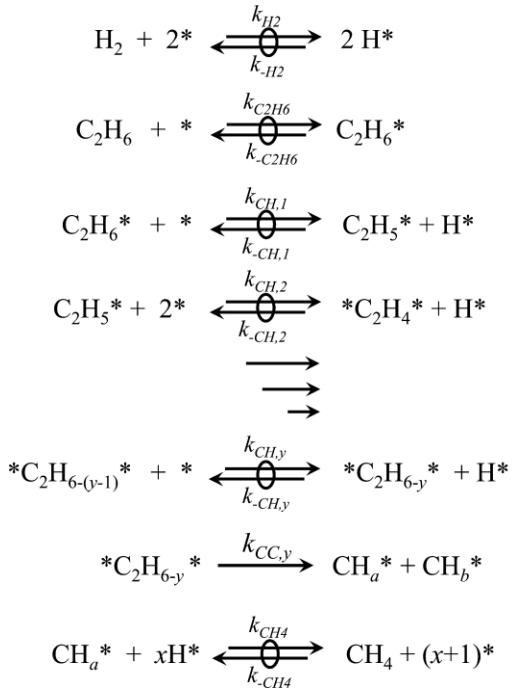

Figure 1.7. Steps for ethane hydrogenolysis, where * represents vacant surface sites. Source: Ref. [36].

1.3.3. Hydrocracking over bifunctional catalysts

When combining acid and metal functions in a catalyst, hydrocracking reactions can take place. Hydrocracking is extensively employed in refineries to convert VGO into middle distillate

fuels.[38] These reactions unite the hydrogenation/dehydrogenation capabilities of metals with isomerization/cracking reactions that take place over acid sites. Figure 1.8 illustrates the dynamics of hydrocarbon conversion over bifunctional catalysts.

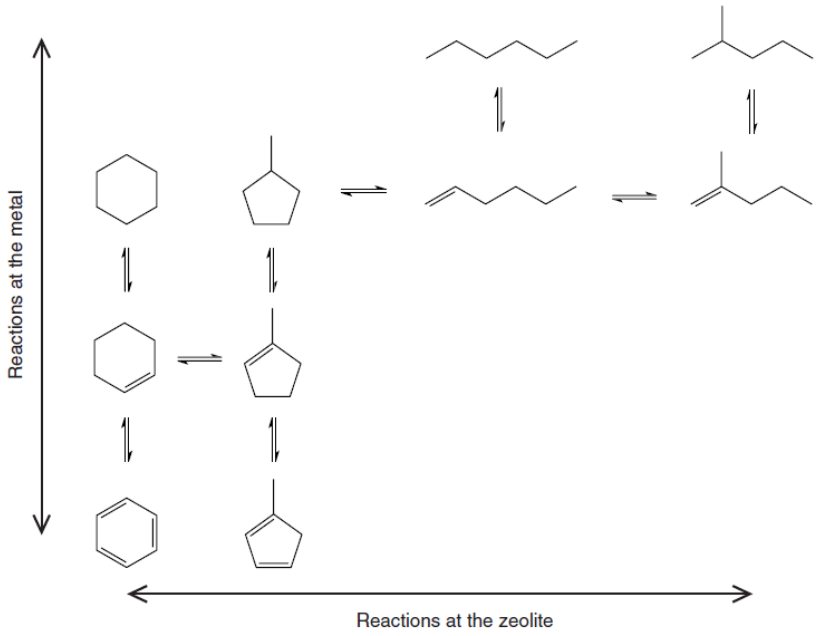

Figure 1.8. Isomerization and hydrogenation/dehydrogenation reactions on bifunctional acid-metal catalysts. Source: Ref [34].

The general rationale for these reactions is that alkanes are dehydrogenated over metal sites, creating olefins that will then be converted onto acid sites (isomerization and/or cracking); finally, these cracking products, which have become shorter chains and more unsaturated, are hydrogenated over the metal function.[38] One important consideration is that this reaction mechanism does not require close proximity between the acid and the metal sites since the intermediates are in the gas phase. This can be demonstrated by the high activity of metal/acid physical mixtures.[39]

Chapter 2: Effect of polymer additives in polyethylene decomposition reactions

2.1. Introduction

Due to consumer demand and performance advantages of plastics over competing materials [40], worldwide plastic production has been growing in recent years. [41] The generation of plastic waste is also growing. Mechanical recycling will not be a comprehensive solution for this problem, as it does not generate a final product of the same quality as the original one. [42] Furthermore, mechanical recycling is not suitable for many regulated applications such as food or pharmaceutical packaging.

Companies are developing technologies complementary to mechanical recycling to chemically recycle and/or upcycle polymers. Chemical recycling is a means to break down plastic waste molecules into their original chemical constituents which is forecast to help meet plastics recycling targets. [43] As a result, the number of publications regarding chemical recycling and upcycling has dramatically increased in the past few years. [44]

Two commonly explored pathways to recycling are pyrolysis – i.e., thermal degradation in the absence of oxygen [45] – and catalytic pyrolysis. Many other approaches have been proposed as well, such as hydrogenolysis, solvolysis and dissolution/precipitation. [16, 44, 46] Pyrolysis occurs via a free-radical mechanism with random scission generating thousands of species, and causing very broad product distributions. [47] The use of catalysts provides lower energy barriers, allowing for conversion at lower temperatures, and targets enhanced selectivity towards the products of higher value. [48]

Delferro and coworkers [15] have recently carried out hydrogenolysis of PE at 300 °C over platinum supported on SrTiO3, and achieved yields of over 90% towards liquid products, in the range of motor oil and waxes. In a subsequent work [49], they housed Pt nanoparticles at the base of silica mesopores and were able to convert PE to a narrow distribution that could be separated into fuel, solvents and lubricating oil. By placing the active site only in the interior of the pores, their products formation was likely governed by diffusion. They found that shorter-chain products would be formed in narrower pores.

The Vlachos group used hydrocracking to decompose polyolefins (PE and polypropylene, PP) into light naphtha- and distillate-range products. [14] They combined equal parts of $Pt/WO_3/ZrO_2$ and acid catalysts at 250 °C to convert low density polyethylene (LDPE). Their results show that the conversion followed the order of pore size: HY > HBEA > HMOR > HZSM-5. Also, they found that HY favors gasoline-range products, whereas HZSM-5 provides high yields of light products (C1-C4). Slower diffusion through the narrower pores in ZSM-5 causes the molecules to undergo more subsequent cracking reactions, hence favoring light gases.

Standalone acid catalysis has also been explored to convert polyolefins. Vollmer et al. carried out a series of PP decomposition reactions using fluidized catalytic cracking (FCC) catalysts at 420 °C. [50] The product distributions showed that the presence of pristine FCC catalyst (containing clay matrix, amorphous silica alumina and HY zeolite) increased C4-C5 production when compared to thermal pyrolysis, which mostly yielded C_5+ alkenes. Moreover, reaction over the FCC catalyst produced aromatics, which were not present after thermal pyrolysis. Interestingly, they found that use of ECAT (equilibrium catalyst, i.e., spent FCC catalyst) gave the same yield of aromatics as fresh FCC catalyst, even though the ECAT had reduced microporosity.

ECAT aromatization capabilities were attributed to the metal impurities (Ni, Fe) that accumulate over time during fluidized catalytic cracking.

There are many publications in the literature that study polymer decomposition reactions, aiming to find efficient ways to recycle waste. However, most studies employ relatively simple polymer systems, whereas commercial plastics are often far more complex, comprising multilayered films and/or including dyes, coatings, catalyst residues, and functional additives. In fact, most commercial polymers by necessity contain a range of additives required to meet the performance requirements of their intended application. Such additives include primary and secondary antioxidants, UV stabilizers and acid scavengers to name a few. [51] These additives can potentially create new challenges to any recycling approach that involves use of heterogeneous catalysts, as they can interact with the catalyst being used or react with the active species in the system.[52] While such additives are well documented, no one to our knowledge has explored the impact of such additives on acid-catalyzed pyrolysis – which we have found to yield both significant and surprising results.

In this study, we analyze the effect of four commonly used polymer additives in the thermal and catalytic decomposition reactions of polyethylene (PE) – which alone accounts for roughly 30% of all plastics produced worldwide. [3] The molecular structures of the additives used are depicted in Figure 2.1: (A) Cyasorb UV-3346, a hindered amine light stabilizer (HALS), referred hereafter as “aminic”; (B) Irganox 1010, a phenolic primary antioxidant, “phenolic”; (C) Irgafos 168, a phosphite secondary antioxidant (i.e., a hydroperoxide scavenger), “phosphite”; and (D) zinc stearate, which works as an acid scavenger [53], “ZnSt”.

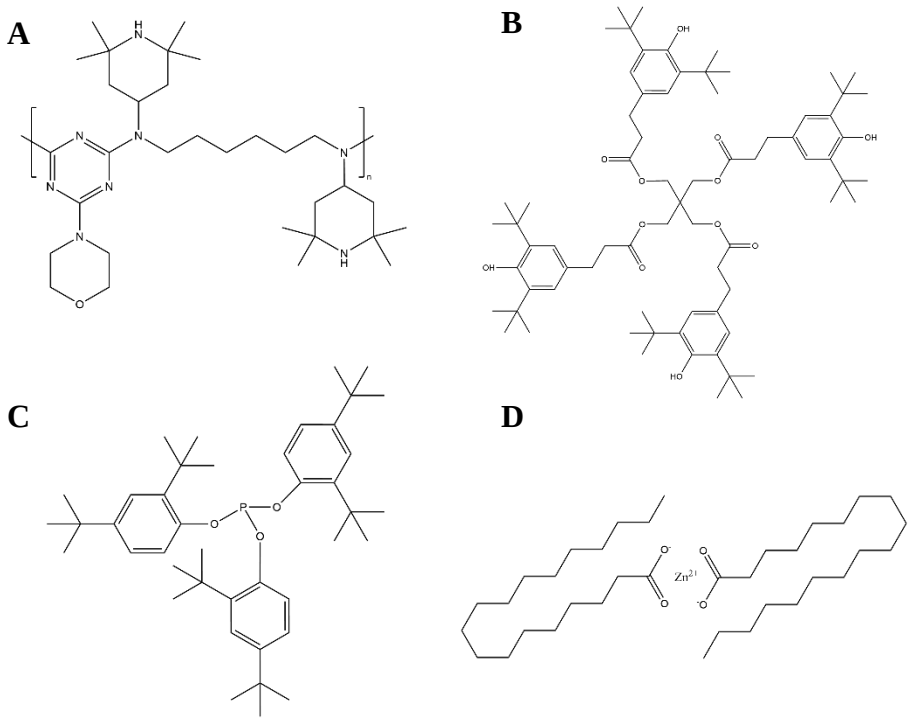

Figure 2.1. Molecular structure of all additives used. (A) UV-3346, aminic additive; (B) 1010, phenolic additive; (C) 168, phosphite additive; and (D) zinc stearate (ZnSt).

2.2. Experimental

2.2.1. Polyethylene samples preparation

Commercial high density polyethylene (HDPE) resin was provided by Chevron Phillips Chemical. Additives were incorporated into the polyethylene by use of a heated mixer. The mixtures of plastic and additive were heated to 190 °C under N2 flow and stirred for 10 minutes at a rate of 47 rpm. Then, the molten samples were pressed into their final disc form to speed up cooling. Each sample consisted of polyethylene plus one additive only, yielding 5 plastic samples in total: pure PE ("PE 0%"); PE + 10% aminic; PE + 10% phosphite; PE + 5% phenolic; and PE + 5% ZnSt.

2.2.2. Catalyst preparation

NH4-ZSM-5 (framework type MFI), Si/Al = 40, was obtained from Zeolyst International. The catalyst was calcined at 600 °C for 5 hours, under 40 ml/min flow of compressed air (80% N_2/20% O_2). The ramp rate used to achieve the calcination temperature was 2 °C/min. This calcined zeolite is hereafter referred to as fresh HZSM-5.

In order to obtain regenerated catalyst, 1 g of each plastic sample was decomposed over 100 mg of HZSM-5 in a ceramic boat inside a horizontal flow reactor. Reactions were carried out under 40 ml/min N2 flow, with the temperature ranging from 25 to 500 °C at a rate of 5 °C/min, then keeping the final temperature for 2 hours. After the reaction was complete and the reactor cooled down, the coked catalyst was regenerated by calcination under 40 ml/min air. The calcination temperature ranged from 25 to 500 °C at a rate of 1 °C/min, and the final temperature was kept for 2 hours.

2.2.3. Catalyst characterization

2.2.3.1. IPA-TPRx

The Brønsted acid site density was determined by isopropylamine temperature programmed reaction (IPA-TPRx). For each experiment, a bed of 50 mg of catalyst was mounted in a 0.25 in. OD quartz reactor. The zeolite was pretreated for 1 hour under He flow, at 300 °C, to eliminate any adsorbed water. Then the temperature was lowered to 100 °C, and 20 µL of IPA was injected (ten 2 µL injections, 5 min between pulses). After finishing the IPA injections, the bed was kept at 100 °C for one more hour, in order to desorb any physisorbed IPA. The reaction was then initiated by increasing the reactor temperature at 10 °C/min, up to 600 °C. Downstream of the reactor, an MKS Cirrus mass spectrometer recorded the evolution of gases. At elevated temperatures, IPA (tracked by m/z = 44) breaks into propylene (m/z = 41) and ammonia (m/z = 17) over Brønsted acid sites.[54] The area of the propylene peak generated by each sample along

with the calibration peak was used to quantitatively determine the number of Brønsted acid sites.[55]

2.2.3.2. SEM

Catalysts were mounted to the SEM stubs by use of a conductive carbon tape. The samples were then sputter-coated with ~5 nm iridium to render them conductive. Samples were imaged using a Zeiss Neon 40 EsB scanning electron microscope (SEM) equipped with an INCA Energy 250 electron dispersive spectroscopy (EDS) detector. Electrons were produced by a field emission source with an accelerating voltage of 20 keV. X-ray signal was acquired in order to get elemental composition and generate composition maps.

2.2.3.3. XPS

X-ray photoelectron spectroscopy (XPS) was run on modified zeolites in a Physical Electronics PHI 5800 ESCA system equipped with an Al Kα X-ray anode. Quantitative elemental composition near the surface and speciation of the atoms deposited onto the catalyst were acquired.

2.2.4. Decomposition reactions

Polymer decomposition reactions were carried out in a NETZSCH STA Jupiter 449 F1 thermogravimetric analyzer (TGA) system, under 40 ml/min flow of Argon. The evolved gases were analyzed by a coupled QMS Aeolos 403 C mass spectrometer (MS). Crucibles used were made of Al_2O_3. About 20 mg of polyethylene were reacted in each run, with 2% ZSM-5 (0.4 mg) in the catalytic runs, except when specified otherwise.

Hexane cracking was performed in a gas-phase 0.25-in. OD quartz tube micropulse reactor. Catalysts were pre-treated at 480 °C under 75 ml/min flow of helium. Several pulses of hexane were sent to the catalyst bed, with 0.48 μmol of C_6/pulse, 3.7 mol% of C_6 in He. Reactions were carried out at 480 °C. The composition of the gas downstream to the reactor was analyzed in a

Shimadzu QP-2010 GC-MS/FID system equipped with an HP-PLOT/Al_2O_3/S column (30 m x 0.25 mm x 0.25 μm).

For product distribution analysis, polymer decomposition reactions were carried out in a CDS Analytical 5250T micropyrolyzer system, connected online to a Shimadzu QP-2010 GC-MS/FID system equipped with a 30 m HP-5 column. 0.5-1.0 mg of sample were used in each pyrolysis tube.

2.3. Results and Discussion

2.3.1. Effect of additives in the polymer: thermal and catalytic degradation rates

The thermogravimetric analysis (TGA) degradation profiles for pyrolysis of different plastic samples can be found in Figure 2.2 (A). Five samples are presented: one consists of polyethylene only, “PE 0%”, and each of the other four PE samples contain high concentrations of one of the four additives under study. It is noteworthy that these additive concentrations are much higher than commercial concentrations which are on the order of parts per million. Such high concentrations were used to assess long-term effects of accumulation of these species, as well as to better identify possible reactions that would occur in a negligible rate otherwise.

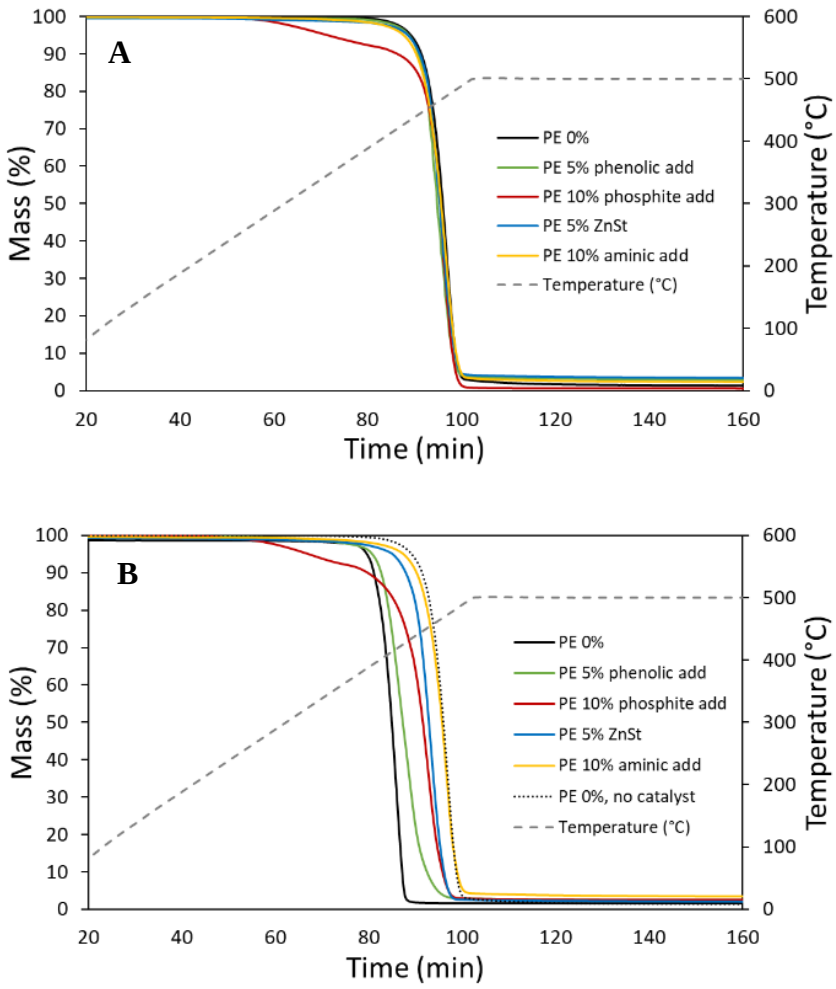

Figure 2.2. TGA profiles for (**A**) thermal degradation and (**B**) catalytic degradation, in the presence of 2% fresh ZSM-5 (40).

In the absence of catalyst, all the curves overlap. This implies that the degradation profile is not affected by any of the additives under study. Even though some of these species (aminic, phenolic) act as H-donors to free radicals [56], and are in much higher concentrations than in commercial polyethylene, they do not hinder rates of reaction in the temperature range above 400 °C. This could imply that these additives may be forming clusters with low surface area in the polymer melt, thus not influencing the pyrolysis.

The phosphite additive, though, seems to be decomposing and volatilizing before any PE decomposition happens, as denoted by the ~10% mass loss before the plastic decomposition. Mass spectrometry analysis of the evolved gas shows that this initial 10% weight loss is indeed from the branched aromatic groups in the additive (Figure 2.3). However, none of the characteristic mass fragments corresponding to phosphorus groups were observed in the gas phase. Hence, the phosphorus itself most likely remains in the melt after this first step of degradation.

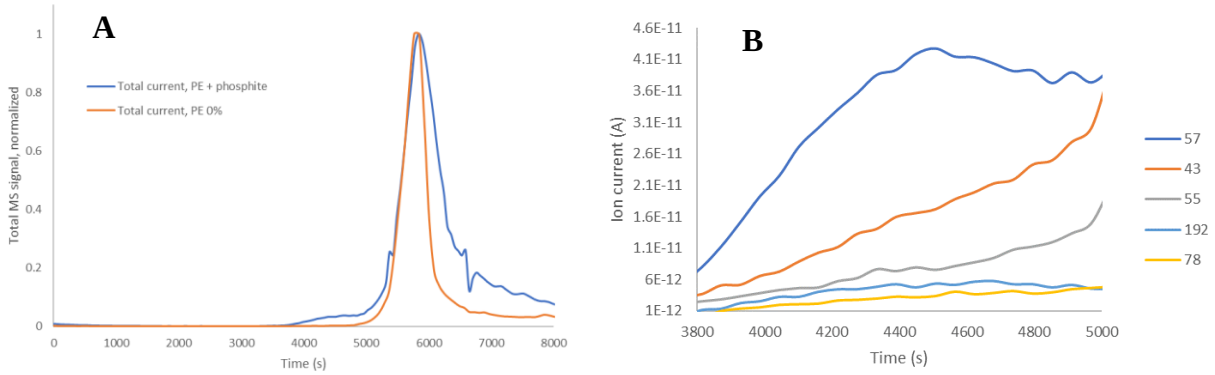

Figure 2.3. Mass spectroscopic analysis of the evolved gases during the TGA pyrolysis. (A) Total ion current detected for PE + 10% phosphite additive (blue) and for PE 0% (orange). From 3800s to 4800s (corresponding to the region between 63 min and 80 min in Figure 2.2(A), there is appreciable signal for the phosphite-containing sample, but no signal from pure polyethylene. (B) m/z signal intensities for the evolved gases from PE + 10% phosphite, from 3800s to 5000s. m/z = 57 is a signature from tert-butyl groups, m/z = 78 is a characteristic signal from benzene rings. This indicates that the organic fragments of the phosphite additive (see Figure 2.1.C) are thermally cleaving and going into the gas phase.

The degradation profiles for each of the plastic samples over 2% fresh HZSM-5 (Si/Al = 40) can be seen in Figure 2.2 (B). The zeolite decreases the temperature of maximum degradation of the pure PE (PE 0%) from 470 °C to 415°C. However, it can be noticed that the catalytic decomposition curves for all the additive-containing samples are shifted to higher temperatures when compared to the pure polymer. This denotes that the presence of all additives hinders the rate of reaction at different levels.

The aminic additive has the most prominent effect in neutralizing the catalyst, since it contains several nitrogen-containing functional groups that can serve as basic titrants to the acidic sites in the zeolite. Zinc stearate also considerably lowers the catalytic rate of reaction, which agrees with the fact that its use in PE resins is to neutralize free acidity from catalyst residue.

Phosphorus is known to lower the acidity of zeolites, both by reducing the number of total acid sites and by diminishing the strength of remaining sites.[57] Phosphorus is purposefully added to commercial ZSM-5 catalysts to improve long term catalyst stability. Modifying the stronger portion of the acid sites and leaving the weaker ones may minimize coke forming reactions. One indication that phosphorus is being exchanged in the zeolite is that the residual catalyst from the phosphite runs is the only one that does not turn completely black. Instead, it shows a gray coloration, indicating less coke formation.

The phenolic additive lowers the reactivity less than the others, because it is the only additive tested that does not contain inorganic species that can exchange with surface sites, or basic functional groups that are expected to strongly bind to them. In fact, this additive's role in modifying reaction rates is likely to simply compete for adsorption sites, instead of killing acid sites.

2.3.2. Effect of additives in the polymer: product distribution

Figure 2.4 shows conversion results for thermal and catalytic decomposition of PE 0% at 400-500 °C in a micropyrolyzer system. These experiments had no pre-melting step, and the reaction temperature was kept for 15 seconds. On the thermal decomposition, conversion grows exponentially with temperature, as is predicted by Arrhenius law. Nonetheless, the conversion for

the catalyzed reaction changes linearly with temperature, which denotes that the reaction taking place is external mass-transfer limited.[27]

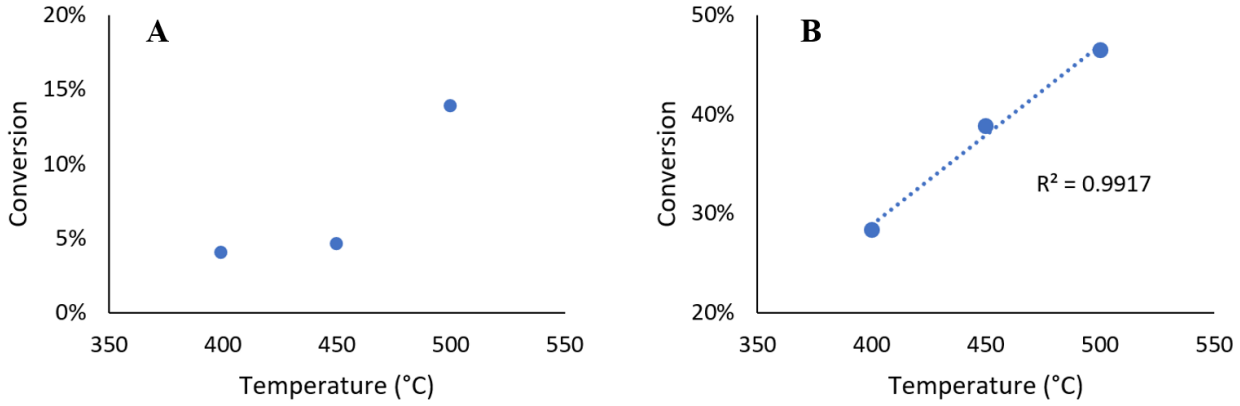

Figure 2.4. Conversion after a 15-second reaction as a function of reaction temperature for (A) PE0%, and (B) PE0% + 2% ZSM-5 (40).

For the subsequent experiments in this system, the pyrolysis program consisted of a pre-melting step of 200°C for 30 seconds, followed by 30 seconds of reaction at 500°C for runs with no zeolite, or at 350°C for runs with ZSM-5 (Si/Al = 140). The higher Si/Al ratio corresponds to a lower acid site density per gram of catalyst, lowering the contribution of diffusion on the measured reaction rates. The reason for running at such low temperature with catalyst is that the first reactions carried out for 2 minutes at 500°C had conversions approaching 100%, which is not ideal for assessing reaction rates and product distributions. Also, having the reactions take place at 350°C would avoid simultaneous thermal depolymerization.

Table 2.1 summarizes conversion results for each of the plastic samples, with and without catalyst. *Conversion* is calculated as the weight difference of the pyrolysis tube before and after reaction, and the values displayed are the average result of triplicate runs. The same trend seen in TGA runs is present in the pyroprobe results: the presence of all additives hinders catalytic

decomposition. Consistently, the additives which hinder the most the catalyst activity are the aminic and ZnSt, respectively. However, in these experiments, the phenolic additive has shown lower increase in conversion (catalytic vs. thermal) than the phosphite one. This may be due to the fact that the zeolite used in the pyroprobe (Si/Al = 140) has a lower acid density than the one used in the TGA (Si/Al = 40), hence making the competitive adsorption more important.

Table 2.1. Conversions in the micropyrolyzer system for different polyethylene samples after 30 seconds at the reaction temperature.

Sample	Conversion (%)		Increase ($X_{catalytic@350}/X_{thermal@500}$)
	No catalyst	10% ZSM-5 (140)	
PE 0%	3.6	9.1	2.55
PE 5% phenolic	11.1	18.5	1.67
PE 10% phosphite	3.2	7.8	2.46
PE 5% ZnSt	2.9	3.5	1.21
PE 10% aminic	7.5	8.4	1.12

Plastic samples thermally pyrolyzed at 500 °C generated mainly alkanes and olefins vapors. Some samples also produced aromatics, nitrogenated compounds and others, likely resulting from the decomposition of the additive present. The overall product distribution for each sample can be found in Table 2.2. Alkanes and olefins carbon number distribution for all samples is shown in Figure 2.5.

Table 2.2. Overall production in pyrolysis system for different PE samples with no catalyst. Pyrolysis program: 30 s pre-melting at 200 °C, 30 s reaction at 500 °C.

	Alkanes and Olefins	Aromatics	Nitrogenated	Oxygenated	Unknowns
PE 0%	99.2%	-	-	-	0.8%
PE 5% phenolic	92.3%	-	-	-	7.7%
PE 10% phosphite	71.8%	24.4%	-	-	3.8%
PE 5% ZnSt	95.9%	-	-	-	4.1%
PE 10% aminic	75.0%	0.6%	6.5%	1.8%	16.1%

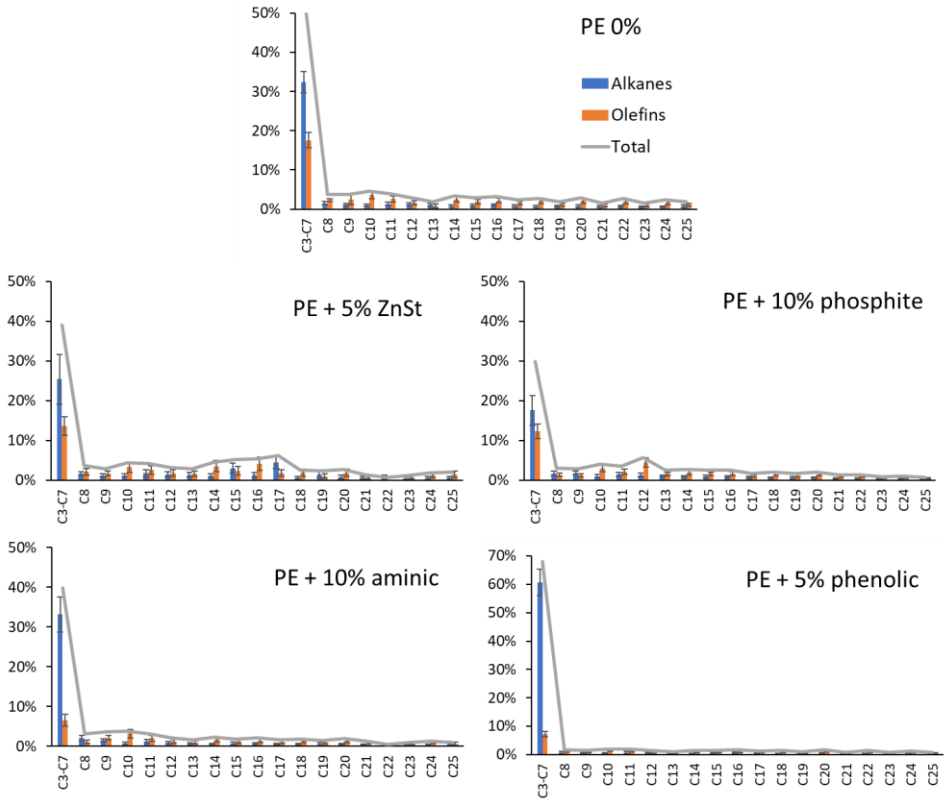

Figure 2.5. Alkanes and olefins distribution for PE samples, after 30 s pre-melt at 200°C and 30 s reaction at 500°C.

When the samples were reacted in the presence of 10% ZSM-5 (140) at 350 °C, a very narrow product distribution range was observed. All the samples presented only one peak representing light olefins (propylene, isobutylene). In the case of PE 5% phosphite, additive fragments were also observed in small quantities due to this additive's low decomposition temperature. It is reasonable to observe light gases as the only product since the energy barrier for protolytic cracking is not achieved. At 350 °C, the reaction that is most likely to happen in the zeolite is isomerization followed by β-scission, which leads to propylene (when the carbocation is a secondary carbon) and isobutylene (when the carbocation is the tertiary carbon formed in the isomerization).

In order to observe a wider range of product carbon numbers, reactions were performed over ZSM-5 (40) at 500 °C for 2 minutes. The product distributions for thermal and catalytic pyrolysis are displayed in Figure 2.6 and Figure 2.7, respectively. The presence of ZnSt does not seem to have an impact on product distribution for thermal pyrolysis. On the other hand, the presence of zinc in the zeolite-containing system seems to shift the product distribution towards aromatic products. The role of zinc in zeolite systems will be further discussed in the next sections.

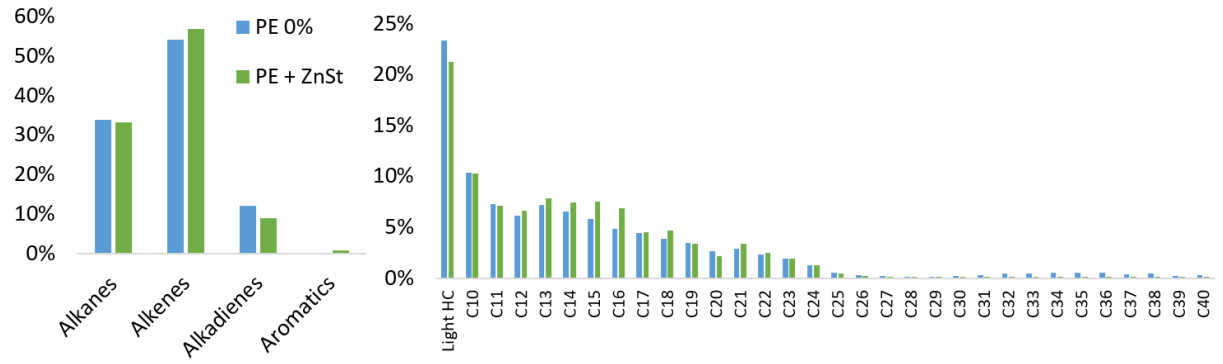

Figure 2.6. Product distribution for PE0% and PE 5% ZnSt after 2 minutes of thermal pyrolysis at 500 °C.

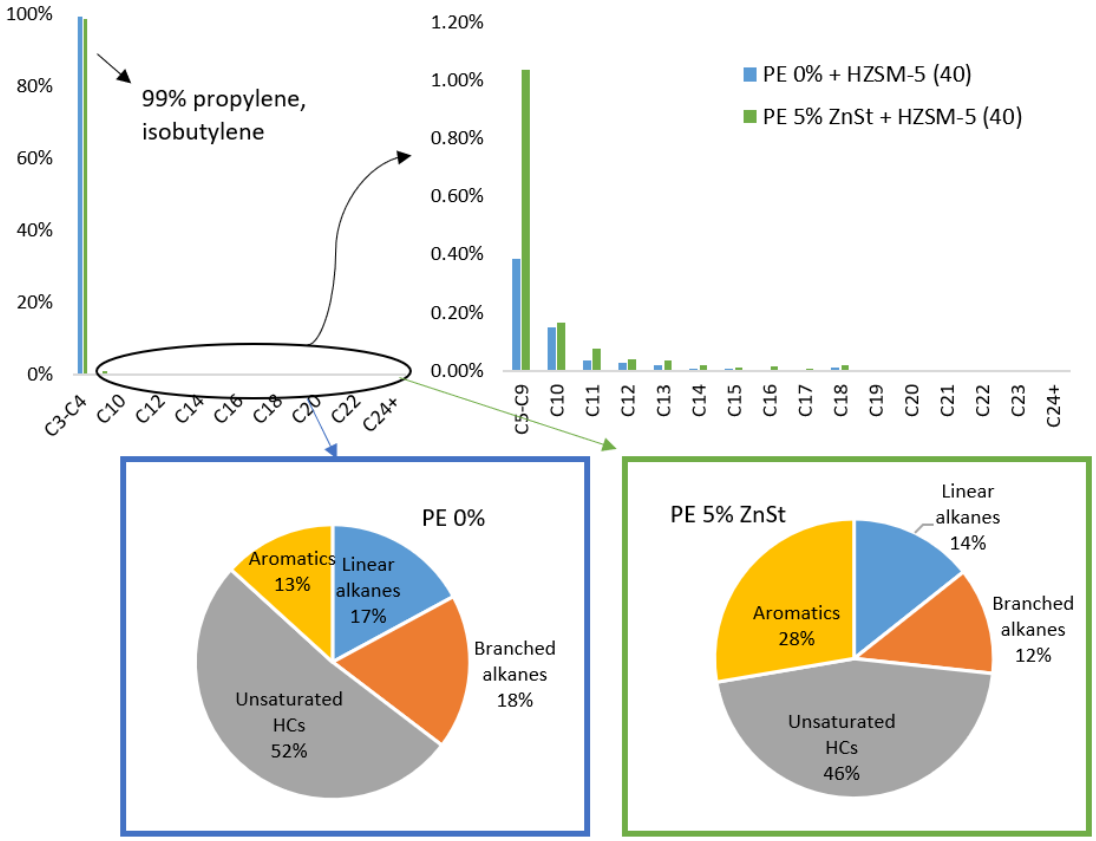

Figure 2.7. Product distribution for PE0% and PE 5% ZnSt after 2 minutes of catalytic pyrolysis at 500 °C.

2.3.3. Understanding how the presence of additives modify catalysts over time

To assess how these different additive molecules can modify the zeolite in the long term, isopropylamine temperature-programmed reaction (IPA-TPRx) was performed for catalysts (see section 2.2.3.1) after plastic conversion. The results obtained are depicted in Figure 2.8 and summarized in Table 2.3. The Brønsted acid site density determined for fresh ZSM-5 (40) was 0.386 mmol/g cat (Figure 2.8 A). After undergoing PE 0% reaction under an inert environment with a catalyst-to-polymer ratio of 1:10, this number drops to 0.165 mmol/g cat (Figure 2.9 A), meaning that 0.221 mmol/g cat were deactivated after reaction (which corresponds to 57% out of

the total Brønsted sites). After regeneration (see section 2.2.2), the number of accessible sites was 0.333 mmol/g cat (Figure 2.8 B), indicating that the calcination was able to recover 76% of the deactivated sites.

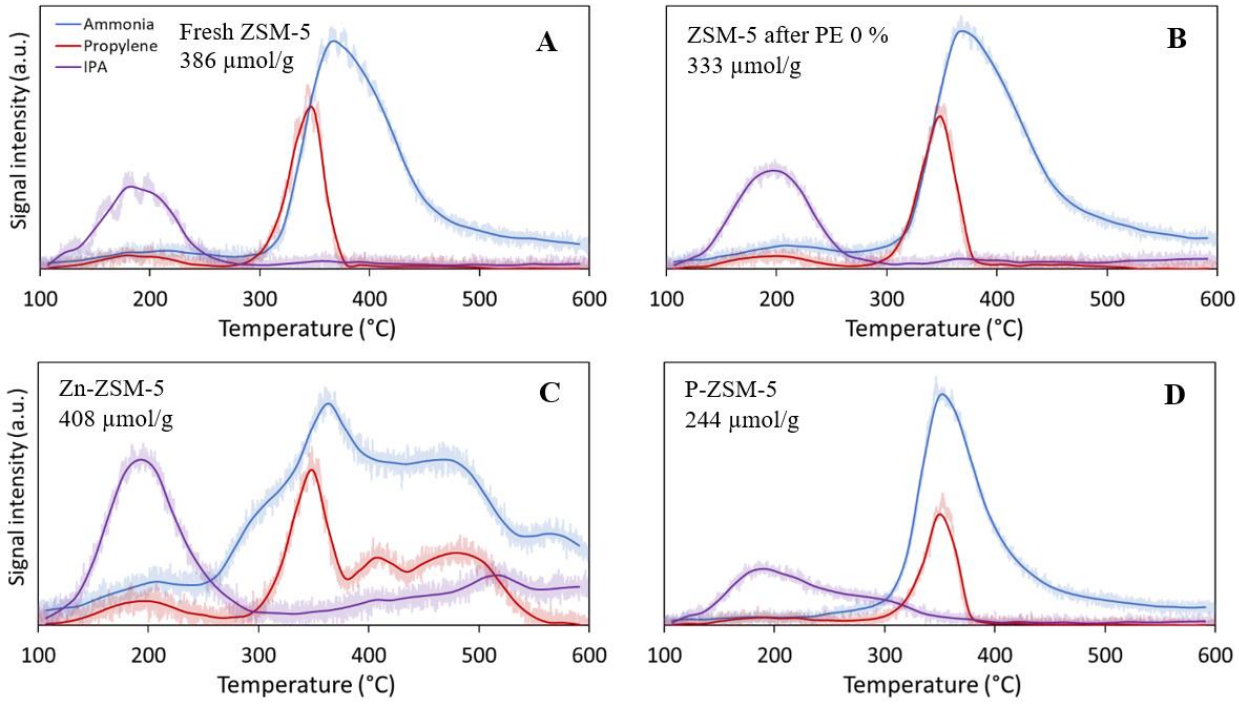

Figure 2.8. IPA-TPRx profiles for (A) fresh ZSM-5, (B) ZSM-5 after PE 0% decomposition and subsequent regeneration, (C) ZSM-5 after PE + 5% ZnSt decomposition and subsequent regeneration, and (D) ZSM-5 after PE + 10% phosphite additive reaction and subsequent regeneration.

Table 2.3. Brønsted acid site density for different zeolite samples: fresh ZSM-5 and regenerated samples after reaction with different plastic samples.

Sample	Brønsted acid site density obtained by IPA-TPRx (mmol H^+/g cat)
Fresh ZSM-5	0.386
ZSM-5 after PE 0% reaction	0.165
Regenerated ZSM-5 after PE 0% reaction	0.333
Regenerated ZSM-5 after PE + 10% aminic reaction	0.339
Regenerated ZSM-5 after PE + 10% phosphite reaction	0.244
Regenerated ZSM-5 after PE + 5% phenolic reaction	0.344
Regenerated ZSM-5 after PE + 5% ZnSt reaction	0.408

Very similar TPRx profiles and acid densities are observed for zeolites that were in contact with polymer containing the aminic and phenolic stabilizers, and were subsequently regenerated (Figure 2.9). This means that, despite these additives interacting with acid sites during reaction, they can be fully removed from the surface via calcination. Nitrogen is most likely converted into NO_x, whereas the phenol groups are burned to CO_2 and water. It is noteworthy that not only is the phenolic additive easily removable from the catalyst surface, but it is also the impurity that displayed the least detrimental effect in the TGA catalytic decomposition curves.

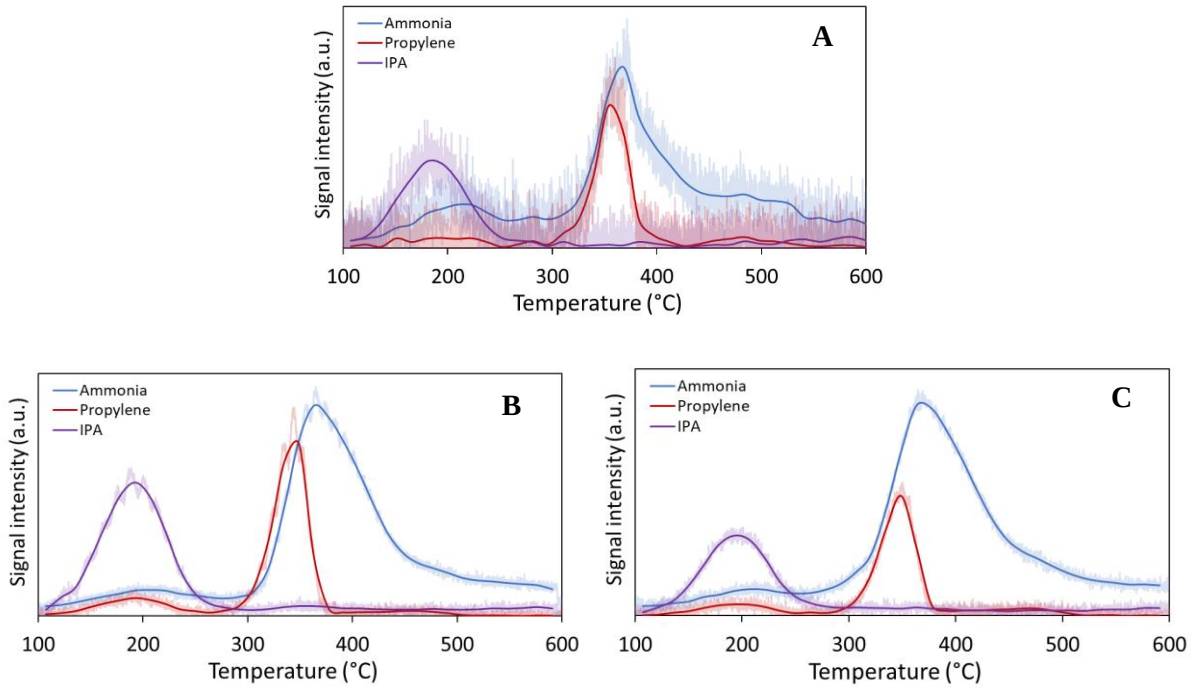

Figure 2.9. IPA-TPRx profiles for zeolites after catalytic PE decomposition reaction. (A) ZSM-5 (40) after contact with PE 0%, before regeneration. Brønsted acidity = 0.165 mmol/g cat. (B) ZSM-5 (40) after contact with PE + 5% phenolic additive, regenerated by calcination. Brønsted acidity = 0.344 mmol/g cat. (C) ZSM-5 (40) after contact with PE + 10% amine additive, regenerated by calcination. Brønsted acidity = 0.339 mmol/g.

The zeolite that contacted the Zn-bearing plastic, though, displays a distinctive TPRx profile after regeneration, as seen in Figure 2.8 (C). The zinc deposits and modifies acid sites,

apparently creating new Brønsted sites that release propylene at higher temperatures, presenting one peak at ~400 °C and another at ~480 °C. The total Brønsted acidity for this sample was 0.408 mmol/g cat. This IPA-TPRx curve is much similar to the one displayed by ZSM-5 that is ion exchanged with different zinc precursors, such as $Zn(NO_3)_2$, to generate Zn-modified zeolites.[58, 59] The traditional propylene peak appearing at 350 °C decreases in this sample (see Figure 2.10 for peak deconvolution), implying some degree of exchange with framework sites at the expense of newly created Zn^{2+}, $Zn(OH)^{+}$, $(Zn\text{-}O\text{-}Zn)^{2+}$ and ZnO sites.[59] About 47% (0.180 mmol/g cat) of the acid sites present in the fresh ZSM-5 are preserved after contact with Zn, whereas the other sites are modified.

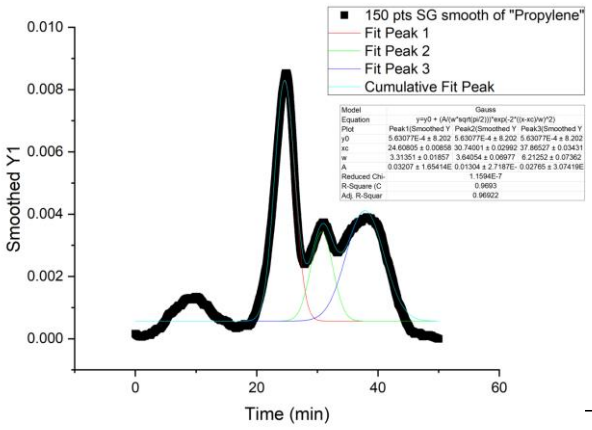

1st peak	180
2nd peak	73
3rd peak	155
Total (umol/g)	408

Figure 2.10. Peak deconvolution for IPA-TPRx for Zn-ZSM-5.

It can also be argued that zinc in fact forms zinc oxide during calcination and plugs the pores of the zeolite to some extent, making it more difficult for the products from the Hofmann elimination to diffuse out – thus the propylene peaks at higher temperatures. This hypothesis could also explain the peak of IPA appearing at higher temperatures. Tamiyakul et al. have reported BET

data comparing ZSM-5 and Zn-ZSM-5 [58], and they found that the addition of 0.87 wt% Zn lowers the surface area by 11%, and the microporous volume by 22%. In this study, the zinc loading is 4.9 wt%, therefore one may expect that the impact in surface area and microporous volume be even higher. However, it is important to note that deposition of other species that also incur some degree of pore plugging, such as phosphorus [60, 61], does not generate new peaks at higher temperatures in IPA-TPRx experiments.

The zeolite used to convert phosphorus-containing polymer was also modified even after calcination, yielding an acidity of 0.244 mmol/g cat (Figure 2.8 D) – that is 27% fewer sites when compared to MFI following PE 0% conversion (Figure 2.8 B). This greater decrease in acidity is expected since phosphorus should exchange with Brønsted acid sites.[57] It can also be noticed that the physisorbed IPA requires higher temperatures to fully desorb from the surface, presenting a new peak at ~300 °C. This could imply the formation of new weak acid sites – P-OH groups, silanol nests or extra-framework alumina – which may not be strong enough to catalyze the Hofmann elimination. Alternatively, the new species formed could be plugging pores and increasing the diffusion path for IPA, which might explain the higher temperature required for full physical desorption.

These results suggested that only zinc and phosphorus were being permanently deposited onto the catalyst. In order to investigate this further, we analyzed all modified samples using scanning electron microscopy – energy dispersive X-ray spectroscopy (SEM-EDS). The only regenerated catalysts which presented elements other than Si, Al, O and C were the ones in contact with the zinc stearate and the phosphite additives – hereafter denoted by *Zn-ZSM-5* and *P-ZSM-5*, respectively. Both elemental maps can be found in Figure 2.11. It was observed that both Zn and

P are well dispersed throughout the sample, and do not seem to form big clumps of these impurities.

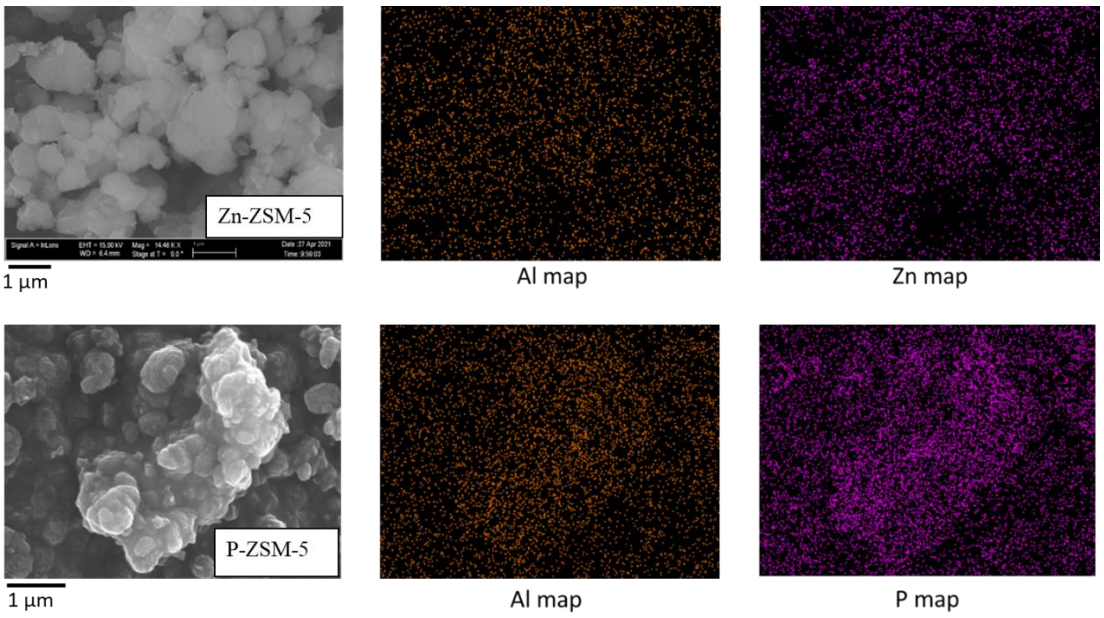

Figure 2.11. SEM-EDS images of Zn-ZSM-5 (top) and P-ZSM-5 (bottom).

X-ray photoelectron spectroscopy (XPS) data reveals the atomic composition of the outermost atomic layers, as well as the speciation of the inorganic impurities in each of the samples (Figure 2.12). The zinc, which according to XPS comprised 2.0% of the probed sample, presents one peak at 1022.74 eV. This binding energy is very close to 1023.0 eV, which is characteristic of $Zn(OH)_2$ [62, 63], and we attribute it to the catalytically active $Zn(OH)^+$ sites. On the sample that had contact with the phosphite additive, phosphorus accounts for 0.6% of the atomic composition on the outer layers. The phosphorus-containing species were determined to be mostly phosphates and polyphosphates, with peaks at 134.88 eV [64] and 135.64 eV.

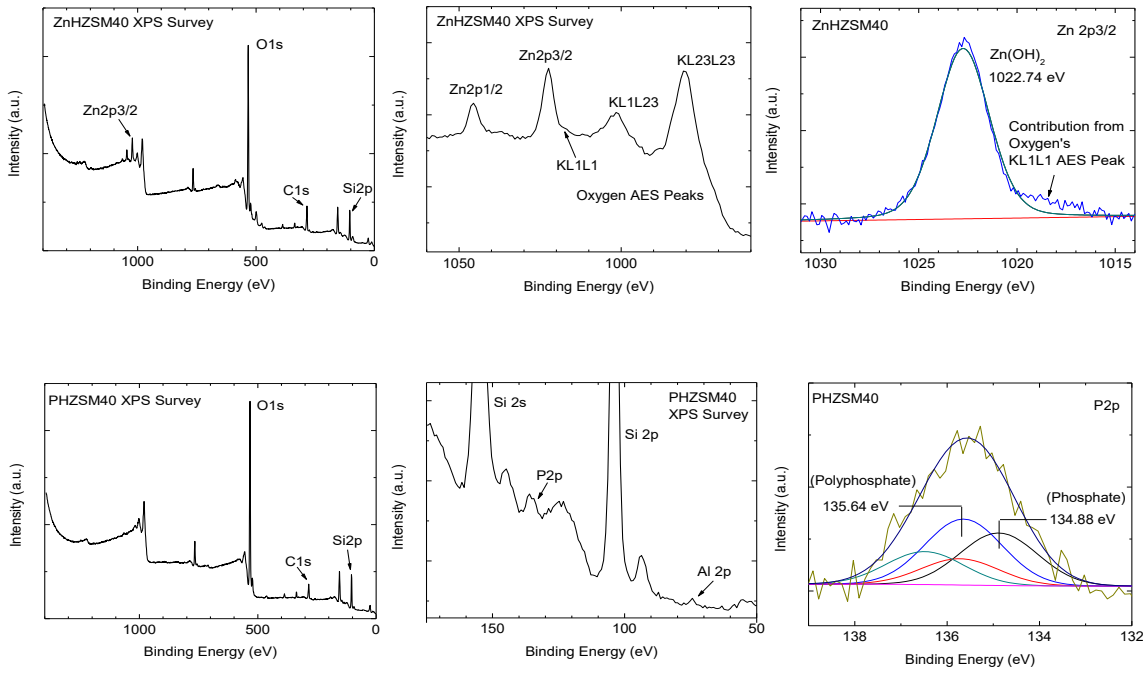

Figure 2.12. XPS survey spectra (left, middle) and high-resolution spectra (right) for Zn-ZSM-5 (upper plots) and P-ZSM-5 (lower plots).

From Table 2.4, both samples show some carbon deposits. Whereas some of this carbon may be contamination from exposure to ambient air [65], certainly a fraction of it comes from unburned coke as carbon is also observed in appreciable quantities in the EDS data (Figure 2.13). P-ZSM-5 presents a lower carbon content when compared to Zn-ZSM-5 (13.4% *vs.* 21.2%). This can be a direct result from the P deposition onto the zeolite, that can reduce coke formation by decreasing the amount of the strongest sites.

Table 2.4. Atomic composition of regenerated catalysts according to XPS analysis

Element	Atomic composition (%)	
	Zn-ZSM-5	*P-ZSM-5*
C	21.2	13.4
O	56.9	63.6
Al	0.2	0.5
Si	19.7	22.0

Zn	2.0	
P		0.6

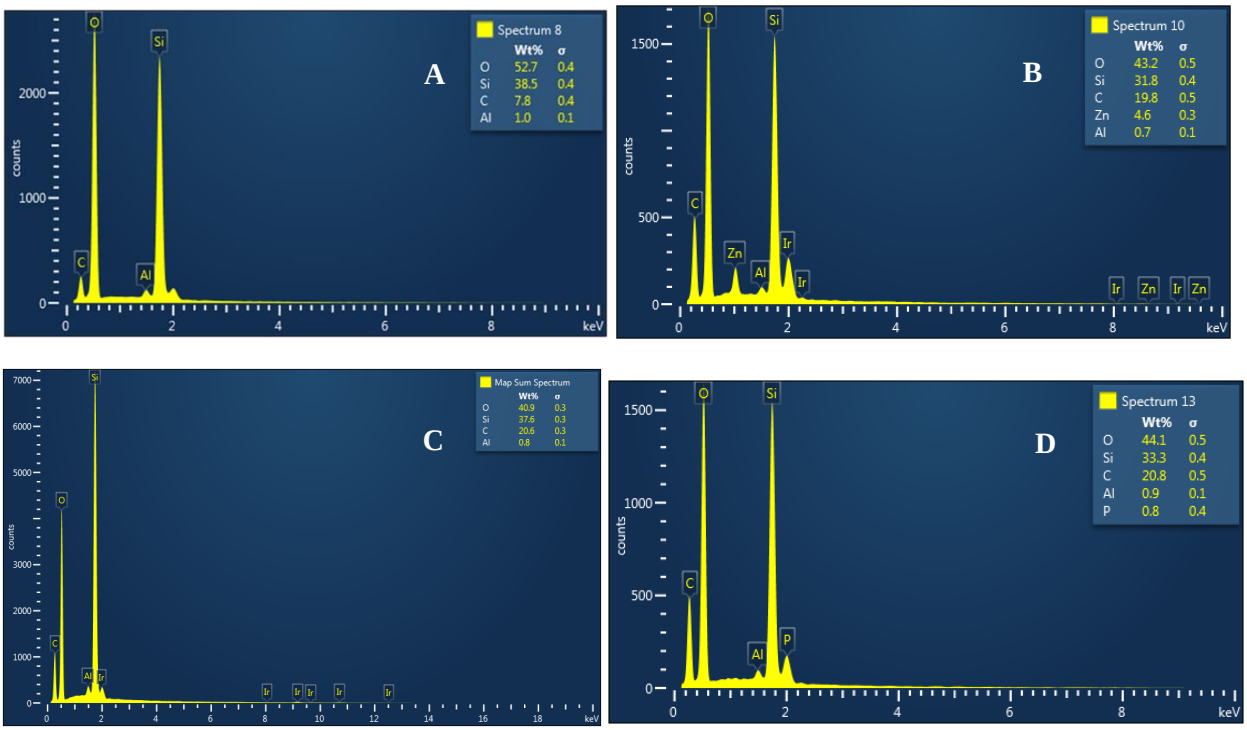

Figure 2.13. SEM-EDS elemental compositions for (A) fresh ZSM-5 (40); (B) Zn-ZSM-5; (C) regenerated ZSM-5 after reaction with PE + amine additive; (D) P-ZSM-5. The fresh ZSM-5 is shown as a baseline for carbon (the signal arises from the carbon tape used to mount the sample). All the other samples, post reaction and calcination, present carbon levels around 20 wt%.

Table 2.5 displays theoretical atomic ratios, and atomic ratios measured by XPS. Theoretical ratios are calculated by dividing the total number of these atoms present in the reaction vessel (in the plastic sample, when preparing the regenerated catalysts) by the total number of Al or Si atoms present in the reaction vessel, considering the weight of catalyst added and the Si/Al ratio provided by the manufacturer. Thus, if all impurities from additives were homogeneously deposited onto the catalyst, the measured XPS ratios would match these theoretical ratios.

Table 2.5. Theoretical and actual atomic ratios from XPS analysis. Theoretical ratios were calculated by dividing the number of inorganic atoms that contacted the sample divided by the theoretical Al and Si number of atoms calculated from the Si/Al ratio provided by the manufacturer.

Atomic ratios	Zn-ZSM-5		P-ZSM-5	
	Theoretical	*Measured*	*Theoretical*	*Measured*
Zn/Al	1.89	9.38	-	-
Zn/Si	0.05	0.10	-	-
P/Al	-	-	3.52	1.42
P/Si	-	-	0.09	0.03
Si/Al	40	94	40	49

The XPS-measured Zn/Al ratio is much higher (~5 times) than the theoretical value, whereas the measured Zn/Si ratio is only twice the theoretical ratio. This suggests that Zn is depositing around the aluminum atoms and, since the XPS probes only the first few atomic layers, the deposited Zn "hides" the aluminum present in the zeolite – thus the measured Si/Al is also higher than expected since the Si is not equally concealed. It can then be concluded that zinc deposits preferentially near aluminum atoms.

Phosphorus, on the other hand, shows lower measured P/Al and P/Zn than the theoretical values, with the measured P/Al ratio being about 40% of the theoretical value and the measured P/Si, about 33% of the theoretical value. This difference denotes that phosphorus encapsulates alumina as well, but in a different fashion than zinc, it apparently deposits on silica almost as much as it deposits on alumina. At first glance, one would think that the measured ratios should always be higher than the theoretical since deposition occurs from the outside of the particle to the inside. Our hypothesis for why the measured values are actually lower than expected is that, as the high resolution XPS showed, most of the P is deposited as polyphosphates. Polyphosphates are large

molecules comprising many phosphates, and these polyphosphates form three-dimensional clumps that “hide” some phosphorus from the XPS, which only probes about three atom layers.

Considering the reaction data and characterization results obtained, we depict proposed additive interactions in Figure 2.14. These additives have much lower molecular weight than the polymer they are dispersed in. Hence, at temperatures above the melting point of the plastic (140 °C in this case, as measured by differential scanning calorimetry – see Figure 2.15), these impurities can easily diffuse to the catalyst surface and quickly interact with the acid sites before most of the cracking chemistry takes place.

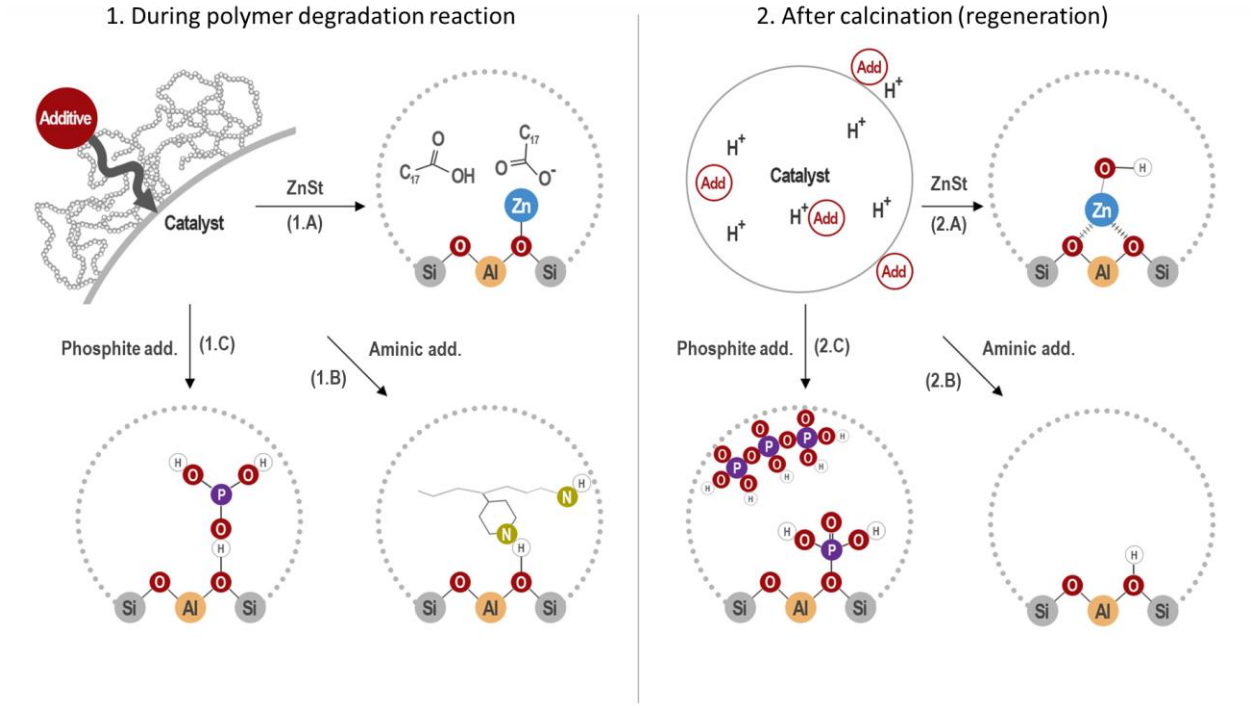

Figure 2.14. Proposed additive-catalyst interactions.

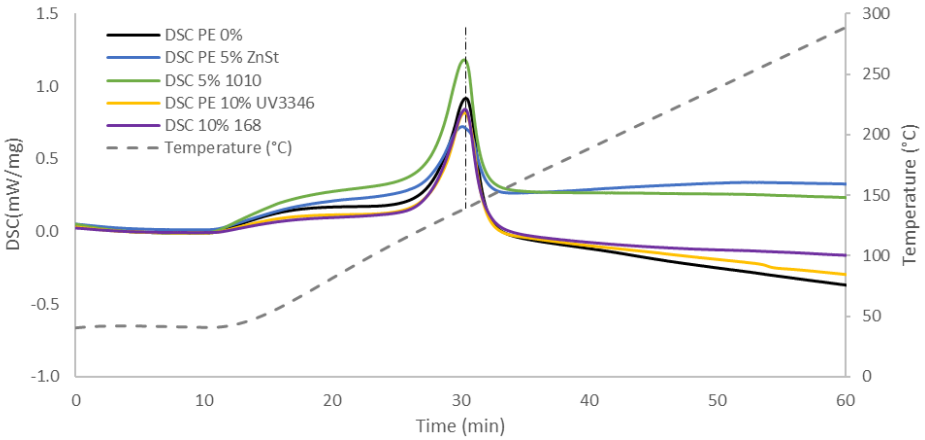

Figure 2.15. Differential scanning calorimetry for different plastic samples under a heating ramp rate of 5 °C/min. Melting point = 140 °C.

Some additives may generate small species – such as the phosphite additive, in which the organic part of the additive decomposes and leaves the melt, leaving behind a small phosphorus group (Figure 2.14 (1.C)) – that will better diffuse into the catalyst particles. Others, such as the polymeric aminic additive, may also incur diffusion limitations and will likely deposit more preferentially near the external surface of the crystallites (Figure 2.14(1.B)). After calcination, these deposited groups will either leave (e.g., NO_x being produced by any amine groups possibly left after depolymerization reaction) or become new sites, like phosphates (Figure 2.14 (2.C)) and zinc sites (Figure 2.14 (2.A)).

There is no evidence that the phenolic additive can modify the zeolite at any stage. Nitrogen-containing groups present in the aminic additive quickly titrate acid sites, rendering them inactive for catalysis. After calcination, however, all the nitrogen is burnt off – as evidenced by EDS and XPS elemental analyses – and the catalyst should regain its activity (Figure 2.14 (2.B)). On the other hand, zinc stearate exchanges with Brønsted acid sites and does not leave after calcination, rather forming active $Zn(OH)^+$ species.

During the plastic decomposition reaction, the hydrogen atoms in the P-OH groups depicted in Figure 2.14 might come from different sources: water from the zeolite, hydrocarbons being decomposed, or from the organic part of the additive itself – there is evidence in the literature that thermal decomposition of this phosphite additive (Irgafos 168) will generate C-C coupling products [66], which can then be hydrogen donors. This structure is speculative, and the phosphorus group interaction with the Brønsted acid site is proposed to occur by a mechanism similar to the model proposed by Blasco, Corma and Martínez-Triguero [60], in which a partially negatively charged oxygen interacts with the proton.

2.3.4. Exploring the role of deposited Zn on ZSM-5

The TPRx profile for Zn-ZSM-5 and the XPS data showing zinc speciation were very similar to zinc-exchanged MFI in the literature.[58, 59] This implied that Zn-ZSM-5 could potentially have great alkane activation and aromatization capabilities. We carried out polyethylene decomposition over different regenerated catalysts, ramping up to 500 °C (Figure 2.16 A). No significant differences in rate were observed when comparing fresh and any of the regenerated catalysts given the rapid decomposition at elevated temperatures. This is likely due to the highly diffusion-limited nature of this system; hence we only observe the diffusion rate, not the intrinsic reaction rate, and can see no appreciable differences between different catalysts that share the same framework.

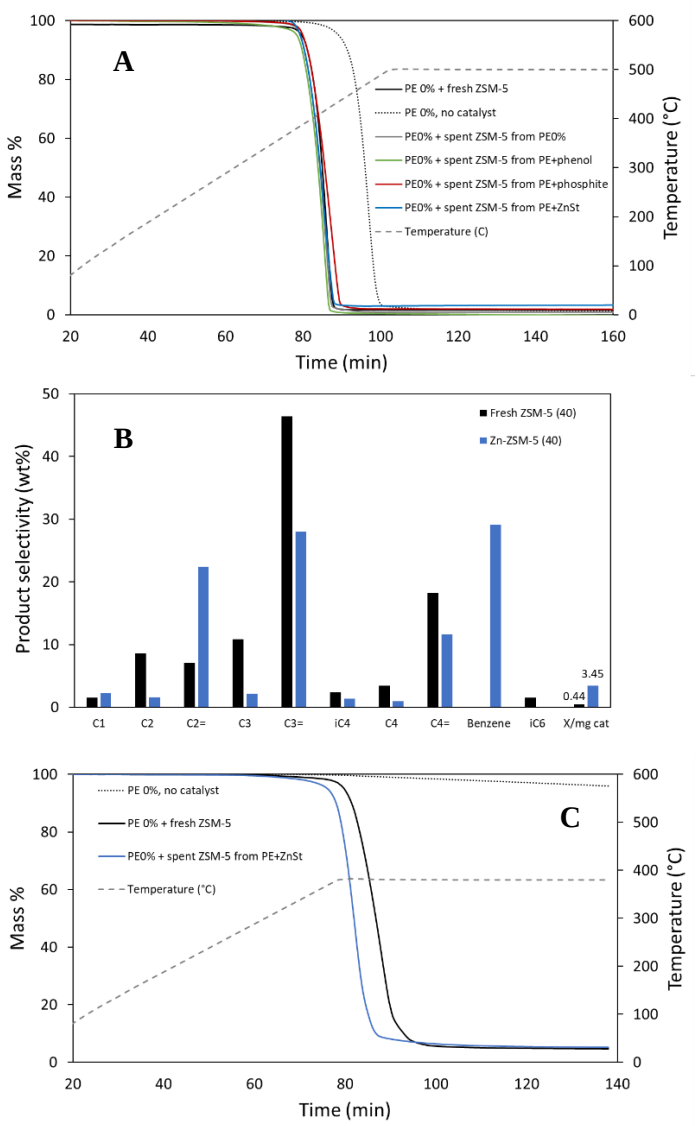

Figure 2.16. (A) TGA profiles for PE 0% decomposition, thermal and over 2% catalysts: no catalyst, fresh HZSM-5 and regenerated catalysts after contacting different plastic samples. Ramp rate of 5 °C/min up to 500 °C. (B) Micropulse reactions comparing fresh ZSM-5 and Zn-ZSM-5: product selectivity and conversion per mg of catalyst. (C) TGA profiles for PE 0% decomposition, thermal and over 5% catalysts: no catalyst, fresh ZSM-5 and regenerated ZSM-5 after exposure to Zn-bearing plastic. Ramp rate of 5 °C/min up to 380 °C.

In order to assess the influence of this modified catalyst on alkane activity in the absence of diffusion limitations, n-hexane cracking experiments were performed at 480 °C in a micropulse reactor to observe the differences in activity and selectivity between fresh MFI and Zn-ZSM-5.

The results for activity and selectivity are shown in Figure 2.16 (B). Hexane conversion was 18.6% over 42.5 mg of fresh ZSM-5, and 86% over 25 mg of Zn-ZSM-5. Since these conversion levels were dissimilar, extra runs with lower loadings of Zn-ZSM-5 were performed (see Figure 2.17), and the trends of higher activity and aromatic yields for Zn-MFI were confirmed.

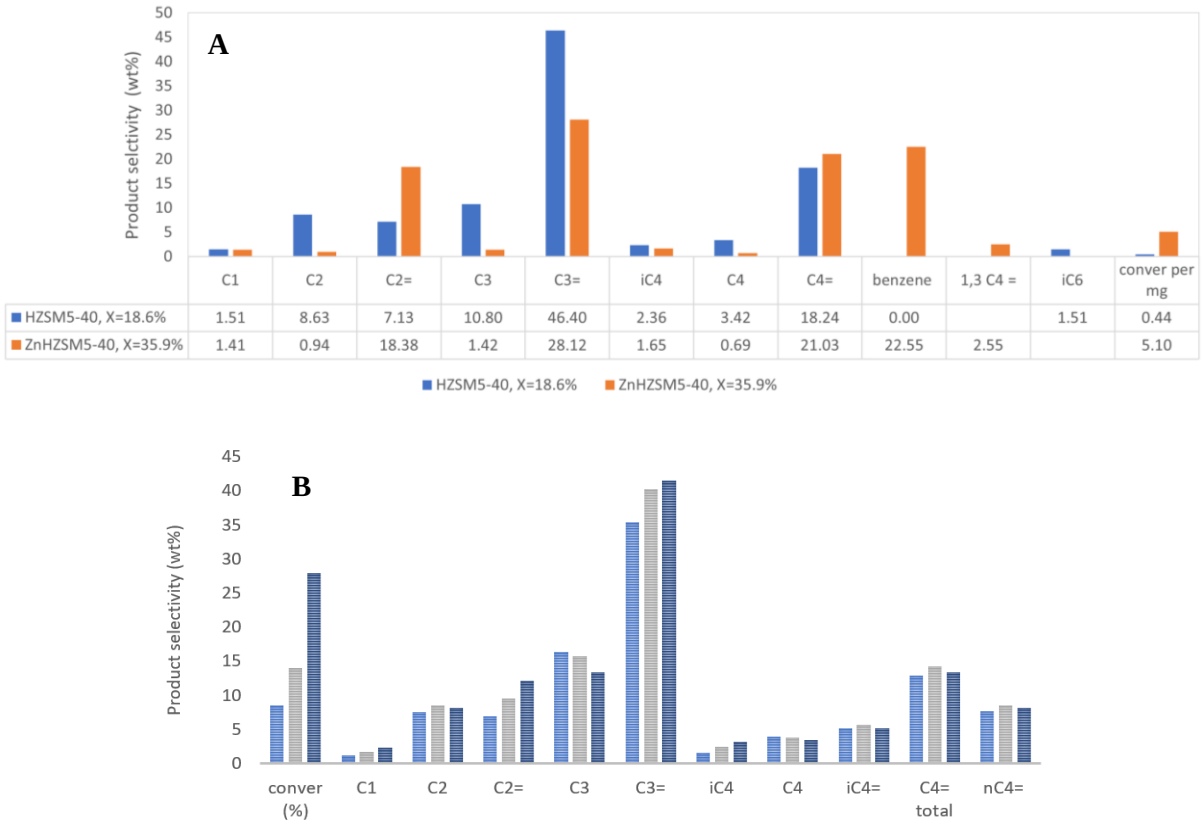

Figure 2.17. (A) Hexane cracking activity and selectivity over 7 mg of Zn-ZSM-5 (40) vs. 42.5 mg HZSM-5 (40) at 480 C; (B) Hexane cracking activity and selectivity over HZSM-5 (Si/Al = 11.5), from Pham et al. [67]. At lower conversion when compared to Fig. 5.B (36% vs. 86%), the Zn-modified still presents higher activity per mg of catalyst and a high selectivity towards benzene. Fig. 8.B shows that hexane cracking selectivities do not change significantly when varying conversion over MFI catalyst.

These results show that the Zn-modified zeolite can indeed activate alkanes much easier than the parent zeolite – conversion per mg was 7.8 times higher over Zn-ZSM-5 when compared to the fresh ZSM-5 (Figure 2.16 B). Also, the product distribution dramatically shifts towards the production of aromatics (benzene), which was nonexistent for the parent zeolite. This result

suggests that not only do the zinc sites play an important role in increasing the reaction rates, but they are also of utmost importance to facilitate aromatization reactions during alkane cracking. [68, 69]

One may speculate that these active sites would facilitate polymer cleavage if conditions were such that diffusion limitations were less pronounced. To assess this possibility, the TGA experiment shown in Figure 2.16 (A) was repeated but holding the reaction temperature at 380 °C, very close to the onset of chemical reactivity – rates of thermal decomposition are negligible when compared to catalytic runs. These results are reported in Figure 2.16 (C), showing a distinct enhancement in activity for the Zn modified sample upon operating under milder reaction conditions. These results illustrate the potential for these additives to positively modify conversion rates of real waste polymer streams.

Also, contrasting Figure 2.16 (C) with Figure 2.2 (B) (where Zn does not enhance rates but hinders rates) we hypothesize that the difference is due to the form of the Zn, with $Zn(OH)^+$ being the active form while the exchangeable Zn^{2+}, or Zn still tethered to the carboxylic acids in the additive that is deposited during the initial conversion step simply exchanges with sites without facilitating alkane activation.

2.4. Conclusions

The findings presented in this work reveal the profound impact that several common additives can have on subsequent catalytic upgrading. The presence of additives will not significantly affect the rate of pyrolysis of polyethylene at high temperatures. When decomposition happens over an acid catalyst, the presence of all tested additives will hinder rates of reaction due to exchange with the Brønsted acid sites, titration, or simply competitive adsorption. It is important

to notice, though, that the concentration of additives in commercial plastic is much lower than the ones used in this work; therefore, it is more likely that such effects will not be significant in commercial samples.

On the other hand, even dilute samples will show very significant effects of additives deposition onto catalyst over many cycles of reaction. Some additives, such as HALS and phenolic antioxidants, do not modify the zeolite permanently (i.e., regeneration by calcination can fully clean the surface of the catalyst post-reaction). Others, such as zinc stearate and phosphites, will permanently deposit zinc and phosphorous over the studied catalyst. The presence of these extra-lattice species will have profound effects in further reactivity and selectivity of these modified zeolites. This knowledge may be used to design polymer recycling processes and modify catalytic processes to better respond to these impurities.

Chapter 3: Confinement effects of Zn deposition onto acid catalysts

3.1. Introduction

Much research has been carried out on Zn-modified zeolites, especially ZSM-5 [58, 59, 70]. As was demonstrated and discussed in the previous chapter, zinc additives present in waste plastics can have a positive effect on the activity of catalysts used for chemical recycling processes. However, bulky molecules such as polymers do not easily diffuse into the micropores of zeolites – this is further discussed in Chapter 4:. Hence, it would be much beneficial if Zn could be deposited onto mesoporous catalysts to perform the same role of improving turnover frequencies and selectivity towards aromatics, but with a network of larger pores that facilitate polymer diffusion.

In this work, we deposited zinc onto mesoporous acid catalysts (amorphous silica alumina and fluorinated mullite) via additive-containing polymer decomposition. Nonetheless, the active $Zn(OH)^+$ sites were not formed and no improvement in activity was observed, even though they present Brønsted acidity as well.

Literature shows that silicalite-1 can be successfully modified by $Zn(NO_3)_2$ via incipient wetness impregnation[59] – that is, new Brønsted acid peaks are present at the range of 375 – 475 °C after zinc deposition. Silicalite-1 is an inorganic material that has the same framework structure as ZSM-5 (MFI) but contains silica only and therefore has no Brønsted acid sites. The fact that silicalite-1 can be exchanged with Zn to form new sites shows that the presence of paired Brønsted sites is not necessary for the formation of the $Zn(OH)^+$ sites. Hence, the inability of zinc to form active sites on mesoporous catalysts might be due to the lack of a confined environment.

There is evidence in the literature that zeolites having larger pores (BEA, 6.7 Å pores) or big cavities (CHA, 7.4 Å cage) do not show enhanced alkane cracking conversions after exchange with zinc.[59] Publications in which Y zeolite (FAU, 11.2 Å cage) was exchanged with zinc do not demonstrate any enhancement in conversion or aromatics yield.[71] On the other hand, there is evidence that Zn-exchanged ZSM-22 (TON, 5.7 Å pores) present higher alkane cracking conversion and aromatics selectivity.[72]

This suggests that more confined structures (MFI, 6.4 Å pores; TON) may be more appropriate for zinc atoms to form active sites such as $Zn(OH)^+$. Here, different zeolite topologies were exchanged with Zn via incipient wetness impregnation (IWI). These modified zeolites were then analyzed by IPA-TPRx and had their reactivity probed by hexane cracking pulse reactions. We also assess the effect of pre-existing paired Brønsted sites on the Zn exchange by using different Si/Al ratio zeolites within the same framework structure (MFI, FAU).

3.2. Experimental

Amorphous silica-alumina grade 135 (Si/Al = 6) was acquired from Aldrich and used as received. Zeolites MFI (Si/Al = 11.5, 40, 140), BEA (Si/Al = 150), MOR (Si/Al = 10), FAU (Si/Al = 2.6, 15) were acquired from Zeolyst International. TON (Si/Al = 32.5-40) and CHA (Si/Al = 10-15) were acquired from ACS Material. Catalysts which were supplied in the ammonium form were pre-calcined under 40 ml/min of air (80% N_2/20% O_2) flow at 600 °C for 5 hours, using a ramp rate of 2 °C/min. A summary of the zeolites used can be found in Table 3.1. Si/Al ratios and surface area values are displayed as provided by the manufacturers. Diameters of spheres that can be included and can diffuse along the largest axis were extracted from the International Zeolite Association database of structures.

Table 3.1. Zeolites properties.

	Si/Al ratio	Max. diameter of sphere that can be included (Å)	Max. diameter of sphere that can diffuse (Å)	Surface area (m2/g)	Supplier code	Form
TON	32.5-40	5.71	5.11	>180	MSZ22H12	H^+
MFI	11.5	6.36	4.7	425	CBV 3414	NH_4^+
	40			425	CBV 8014	NH_4^+
	140			400	CBV 18014	NH_4^+
BEA	150	6.68	5.95	620	CP811C-300	H^+
MOR	10	6.7	6.45	500	CBV 21A	NH_4^+
CHA	10-15	7.37	3.72	670	MSZ13015	NH_4^+
FAU	2.6	11.24	7.35	925	CBV 300	NH_4^+
	15			780	CBV 720	H^+

1 gram of polyethylene containing 5% ZnSt was fully decomposed over 238.4 mg F-mullite and over 113.5 mg ASA (both reactions were performed over a quantity of Brønsted acid sites that is equivalent to 100 mg of MFI-40) at 500 °C under 40 ml/min N_2 flow. The spent catalysts were subsequently calcined under 40 ml/min air flow in order to regenerate their activity. The calcination was performed at 550 °C for 6 hours, and these regenerated samples are referred to as *Zn-ASA* and *Zn-mullite*.

The zeolites were exchanged with zinc via incipient wetness impregnation. The incipient wetness volumes of each sample were calculated by measuring the volume needed to saturate 1 gram of the catalyst powers with water. $Zn(NO_3)_2 \cdot 6\ H_2O$ (reagent grade, 98%, from Sigma Aldrich) aqueous solutions were prepared in order to achieve a Zn/Al atomic ratio of 2 for each of the zeolites. After adding the $Zn(NO_3)_2$ solution dropwise to the zeolites, the samples were dried overnight under vacuum at 80 °C. Finally, they were calcined under 40 ml/min air flow at 500 °C for 2 hours. These samples are referred to as *Zn-[framework code]*, e.g., *Zn-MOR*.

IPA-TPRx was perfomed as described in Section 2.2.3.1, except for CHA samples which were probed using n-propylamine. Due to chabazite's very small pore size, n-propylamine is preferred over isopropylamine as the former presents a smaller kinetic diameter. Hexane cracking was performed in a 0.25 in. OD micropulse reactor connected to an HP 6890 GC-FID equipped with an HP-PLOT column. Reactions were performed using pulses of 0.32 µmol of hexane (0.5 ml/min C_6 flowing into a 500 µL loop along with 100 ml/min N_2), at 480 °C under 100 mL/min flow of N_2. This reaction setup was chosen in lieu of a flow mode to avoid deactivation effects resulting from coking. 15-120 mg of pelletized catalyst (250-425 µm) were packed in the reactor, as well as enough glass beads to complete 150 mg total bed weight. Zeolites were pre-treated under nitrogen flow at the reaction temperature for 1 hour prior to the first pulse injection.

3.3. Results and Discussion

3.3.1. Zn deposition onto mesoporous acid catalysts

After promising results with Zn-ZSM-5, Zn-containing polyethylene was decomposed over mesoporous catalysts in an attempt to combine the enhanced alkane activation capabilities of Zn-modified acid catalysts with an improved polymer diffusivity provided by their mesoporosity. Following the reaction in which Zn had been deposited, the spent ASA and F-mullite were regenerated at 550 °C for 6 hours under 40 ml/min air flow.

Figure 3.1 compares TGA profiles of polyethylene decomposition under inert gas flow over fresh mullite (solid blue line), regenerated mullite after PE 5% ZnSt decomposition (solid green line), fresh ZSM-5 40 (black), and thermal pyrolysis in the absence of catalysts (dotted blue line). Catalysts were added to the system on the basis of the same number of total Brønsted acid sites. At a first glance, it is noticeable that mullite is less effective at depolymerizing PE than the

ZSM-5 catalyst. Although mullite provides the advantage of mesoporosity for improved polymer diffusion, these reactions are likely external mass transfer limited, as shown in Chapter 2. Hence, this trend is reasonable when taking into consideration that mullite particles are considerable larger than ZSM-5 particles used in these experiments. (See Figure 3.2)

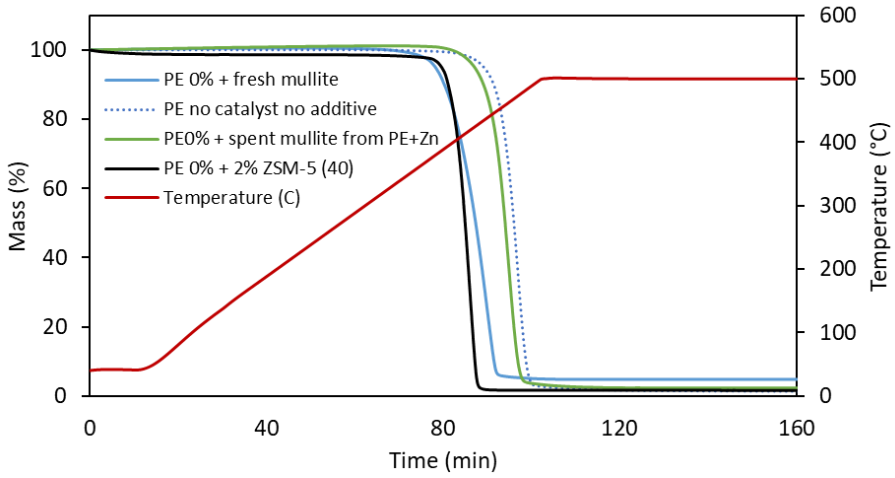

Figure 3.1. TGA profiles for polyethylene decomposition under inert gas flow: thermal decomposition, and catalytic conversion over ZSM-5, F-mullite, and Zn-mullite.

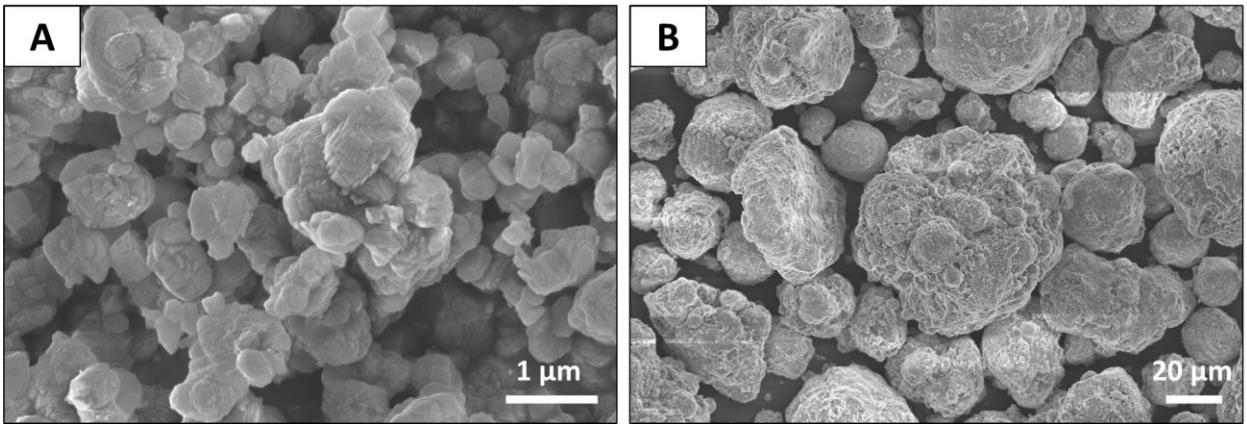

Figure 3.2. SEM images of (A) ZSM-5, Si/Al = 40, 1-micron scale bar; and (B) fresh F-mullite, 20-micron scale bar.

Interestingly, Zn-mullite presented a much worse performance than the parent catalyst, nearing the curve of thermal decomposition. IPA-TPRx was then used to characterize the acid site density of this sample and verify the formation of new $Zn(OH)^+$ sites that catalyze IPA decomposition at higher temperatures than the traditional BAS of zeolites. As shown in Figure 3.3, Zn-mullite presents 92% of the total BAS present in the original sample. However, no $Zn(OH)^+$ peaks at 400 and 500 °C were observed. Nonetheless, elemental mapping displayed in Figure 3.3 (C) indicates that zinc was indeed homogeneously deposited on the catalyst sample and did not form large, low surface area clusters. This implies that Zn deposited as a different species on the mesoporous sample, possibly mainly as zinc oxide.

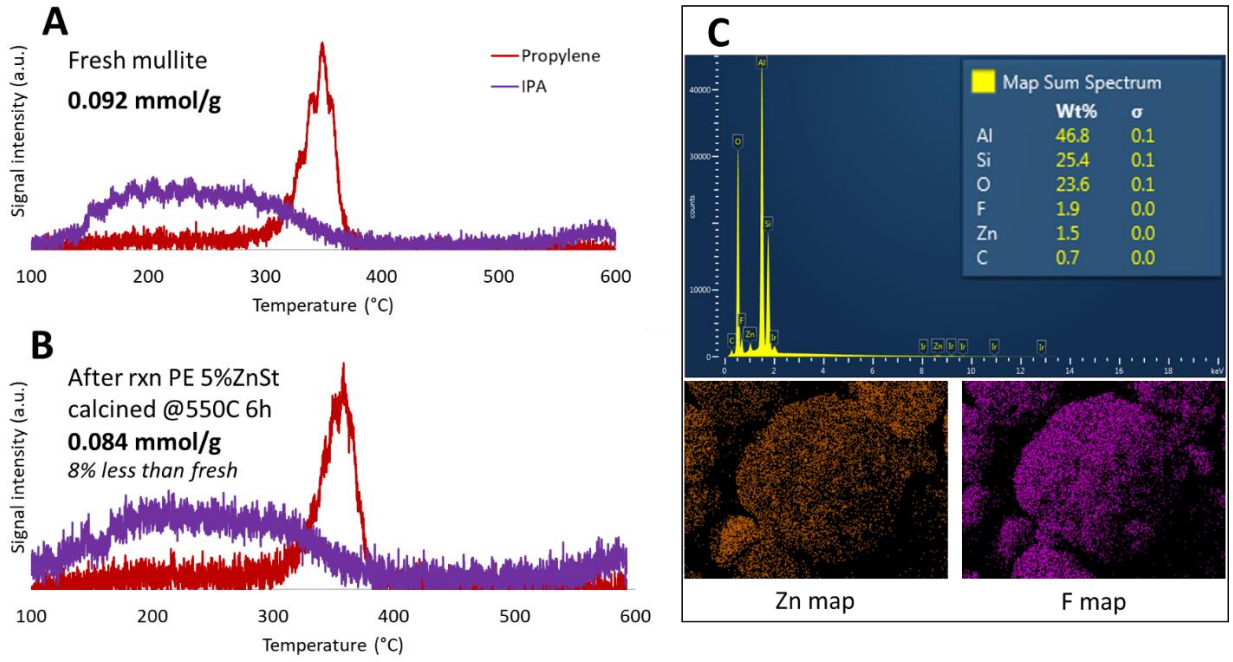

Figure 3.3. IPA-TPRx results for (A) fresh F-mullite, and (B) Zn-mullite. (C) SEM-EDS data displaying the elemental sum spectrum, and Zn and F elemental maps.

The same characterization was performed for Zn-ASA, and the findings can be seen in Figure 3.4. After catalyst use to convert Zn-containing polyethylene and subsequent regeneration,

ASA presents permanent loss of a higher quantity of Brønsted acid sites than mullite – Zn-ASA acid site density was equivalent to 57% only of the original BAS density. Similarly to the case of mullite, Zn-ASA also does not display IPA-TPRx peaks at higher temperatures whereas its SEM-EDS imaging reveals an even distribution of Zn throughout the sample.

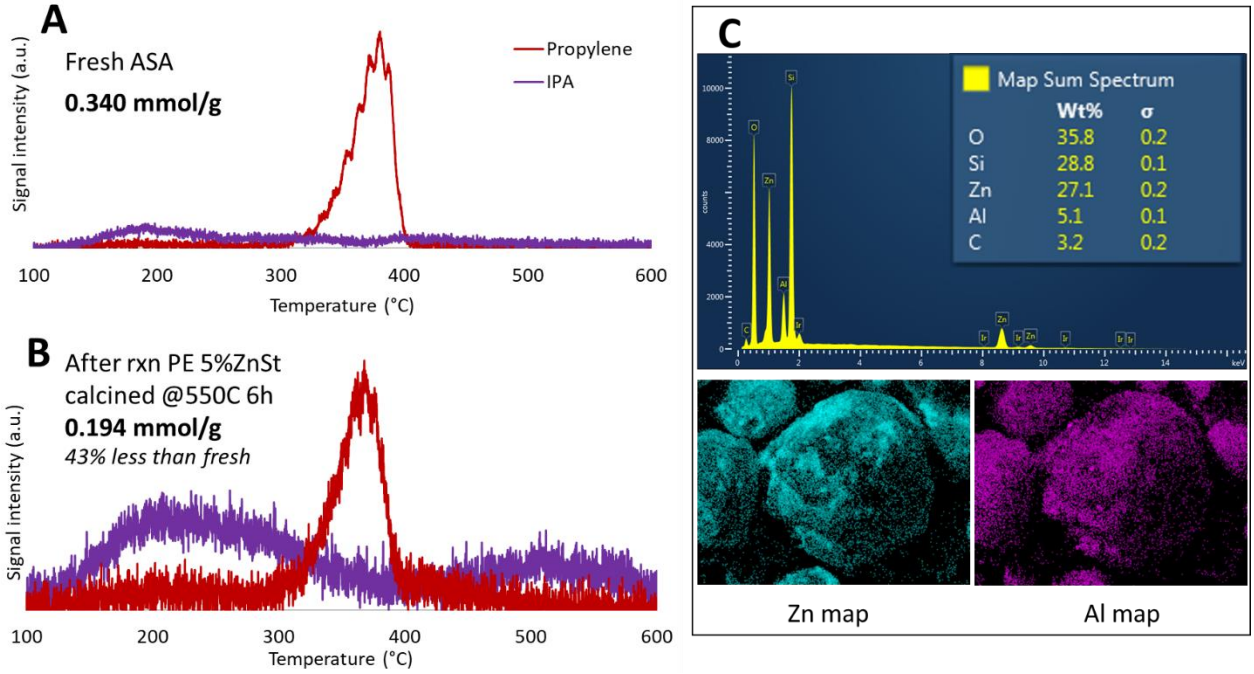

Figure 3.4. IPA-TPRx results for (A) fresh ASA, and (B) Zn-ASA. (C) SEM-EDS data displaying the elemental sum spectrum, and Zn and Al elemental maps.

It might be argued that active Zn sites possibly formed in these mesoporous materials have been destroyed due to harsh regeneration treatment – Zn-ZSM-5 had been calcined at 500 °C for 2 hours, whereas ASA and mullite were heated to 550 °C for 6 hours. Mesoporous catalysts were calcined at higher temperatures because they would remain visually black after treatment at 500 °C for 2 hours. Indeed, temperature programmed oxidation of coked Zn-ASA and coked Zn-ZSM-5 (Figure 3.5) reveal that not only does the mesoporous catalyst accumulate more coke during the PE 5% ZnSt decomposition reaction, but also the nature of the coke deposited is more graphitic.

Consequently, these samples demand higher temperatures and longer times to burn off the coke, resulting in the need for a more severe calcination program.

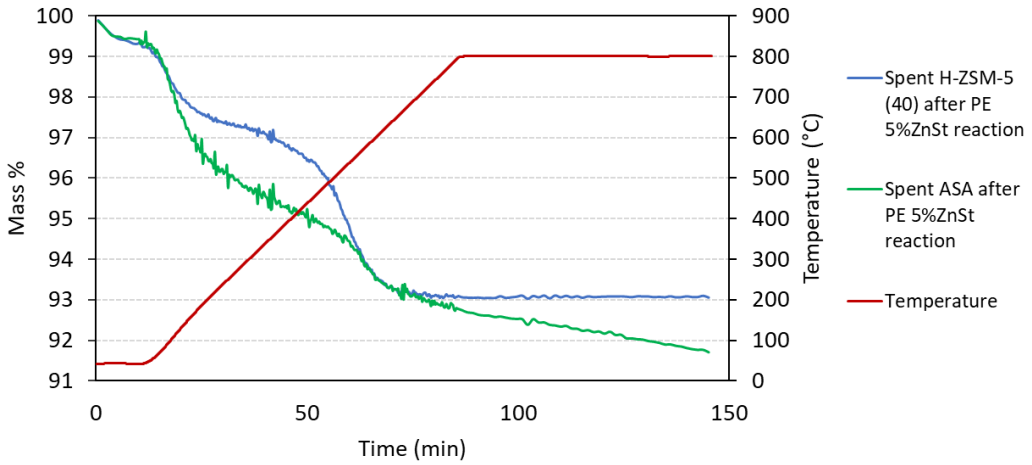

Figure 3.5. Temperature programmed oxidation in the TGA for spent ZSM-5 and ASA, after being used to decompose 1 g of PE 5%ZnSt and before regeneration.

In order to verify whether the harsher calcination program might be decomposing supposedly formed active zinc sites or not, a Zn-ZSM-5 sample was prepared following the same procedure but calcined at 550 °C for 6 hours for regeneration. Both the shape of the IPA-TPRx curve and the total count of BAS remained unchanged. Therefore, we conclude that active zinc sites do not get destroyed at these higher temperatures or longer calcination times. In fact, Zn active sites appear not to be formed on mesoporous catalysts whatsoever, and Zn deposits as an unactive species, even though the chemical nature of all samples is based on silica and alumina.

3.3.2. Zn deposition onto different zeolite frameworks

After deposition of Zn over the different zeolite topologies, IPA-TPRx reveals that $Zn(OH)^+$ are formed regardless of pore size – new peaks at higher temperatures were found in TON, MFI, BEA, and FAU samples. Interestingly, though, the new peak positions were different

for every sample – these results can be found in Figure 3.6. TON presented one new peak at 530 °C, MFI presented two peaks at 415 °C and 490 °C. In these cases, the original BAS peaks at ~360 °C and and ~350 °C, respectively, remained unaltered in position.

For the BEA sample, it is noticeable that there is a new broad peak that ranges from lower temperatures to up to 560 °C. But also, the highest peak position moves from 360 °C (H-form) to 390 °C (Zn-form). This may denote that the Zn-BEA peak at 390 °C is in fact due to the presence of Zn, whereas the original BAS peak at 360 °C has become convoluted with the other two peaks. A similar behavior is seen with the H-FAU and Zn-FAU samples: the BAS peak appears at 355 °C in the H-form, whereas the Zn-FAU sample presents a shoulder at ~340 °C (presumably being the original BAS sites), with two (presumably zinc) peaks at 390 °C and 455 °C.

TPRx was not able to characterize Zn-CHA and Zn-MOR samples, both yielding propylene curves that suggested zero or near zero acidity. However, these samples will be later shown to present considerable hexane cracking activity. One possible explanation for this behavior is a strong degree of pore narrowing, resulting from the high amounts of Zn deposited on these samples. The amount of zinc added to each sample was determined according to their Si/Al ratio, since Zn/Al ratio was kept constant at 2. Hence, more acidic samples such as MOR (Si/Al = 10) and CHA (Si/Al = 10-15) received higher zinc loadings, which likely contributed to pore narrowing. Although bulkier isopropylamine and n-propylamine were not able to reach BAS, hexane was able to react over these catalysts due to its smaller kinetic diameter.

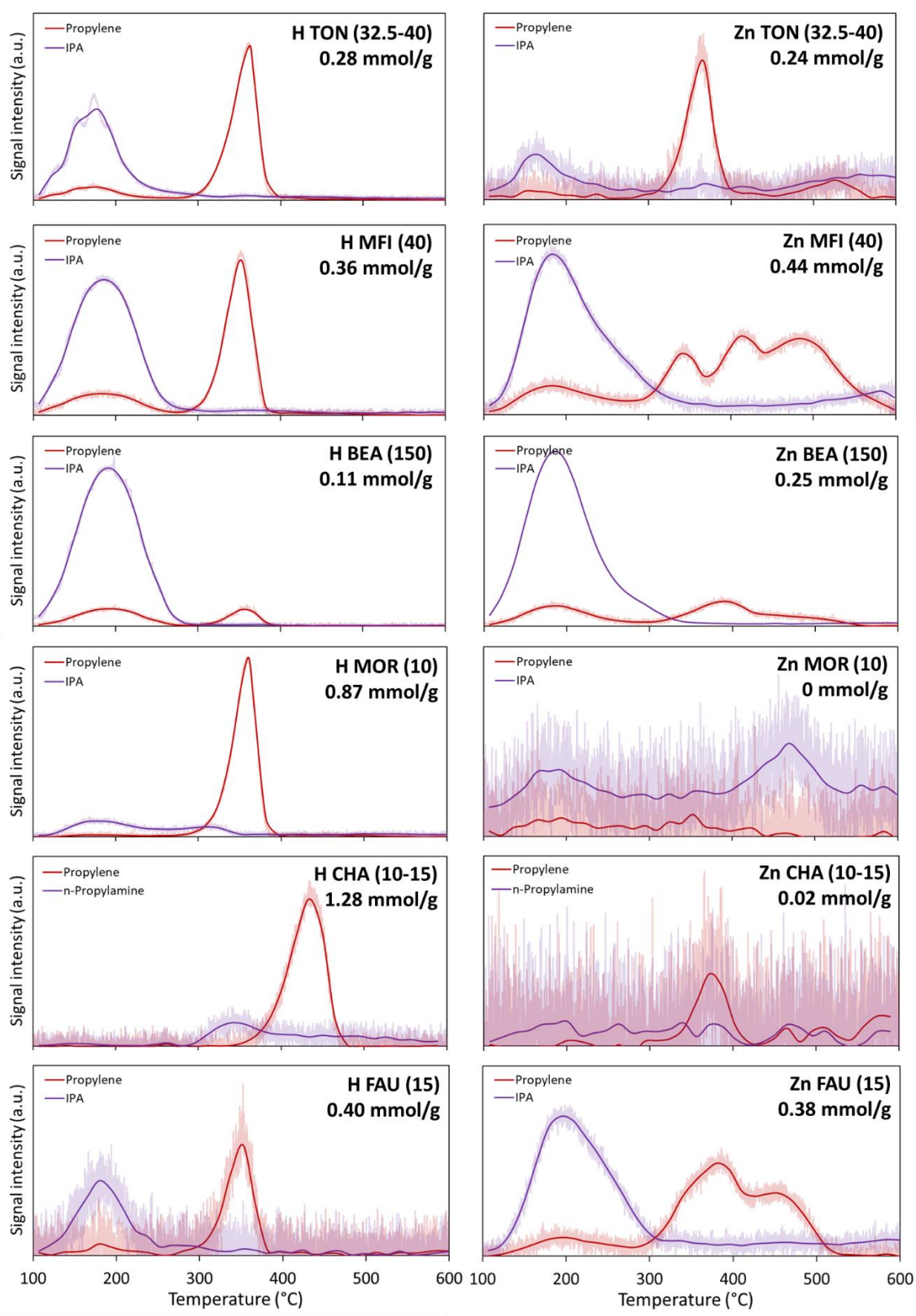

Figure 3.6. IPA-TPRx curves and calculated BAS density for zeolites before and after Zn impregnation.

Figure 3.7 displays the conversions per mg of catalyst and the overall conversions for pulses of hexane cracking at 480 °C for all tested zeolites. It can be seen that Zn improves the activity of all zeolites, regardless of pore size. The only exception to this is the MOR sample, which presented a 43% decrease in conversion/mg after Zn impregnation. Again, this can be explained by the high Zn loading (16.7 wt%) in this sample, which likely caused pore narrowing and some degree of pore plugging.

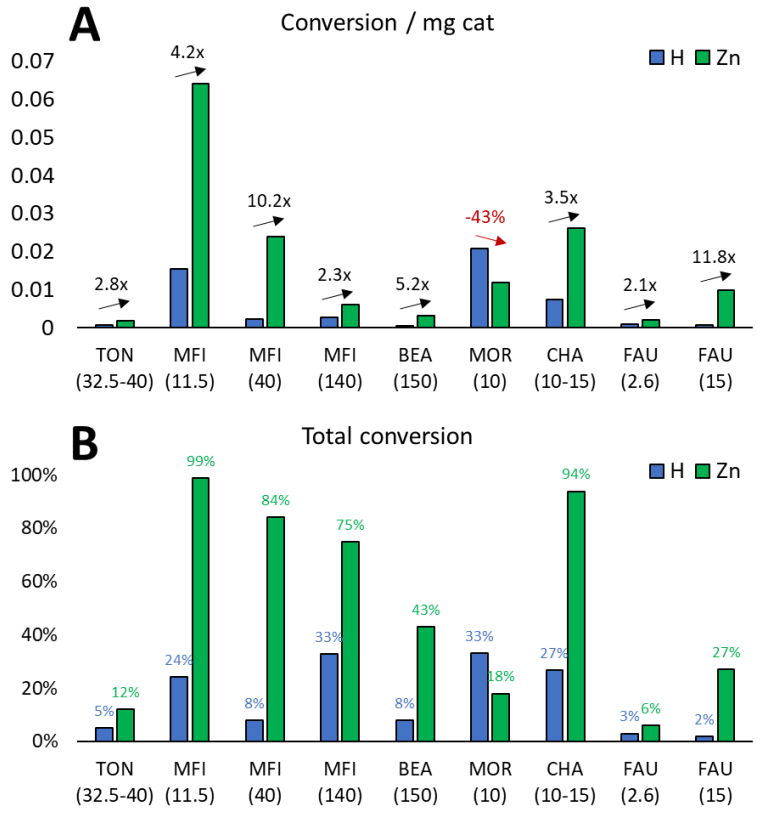

Figure 3.7. Hexane pulse conversion at 480 °C: (A) per milligram of catalyst, and (B) total conversion.

Although the results displayed in Figure 3.7 are useful to assess the ability of zinc to improve activation capabilities throughout the whole range of pore sizes, the only samples that can have their activities directly compared are the ones that have similar and low conversions in their

parent form: TON (5%), MFI 40 (8%), and BEA (8%). Even though FAU samples also presented low conversions with their H forms, deactivation effects were observed even in pulse mode, which compromises any comparison with other samples.

Figure 3.8 compares the improvement in conversion post Zn impregnation vs. the maximum diameter of a sphere that can be included in the TON, MFI and BEA frameworks. This volcano-like trend suggests that MFI may have an optimal pore size to accommodate zinc sites in a manner that maximizes reaction turnover rates. The exact reason why pore size might be important for the formation and activity of Zn sites is not entirely clear yet. One possibility may be that some degree of confinement is necessary to enthalpically stabilize the transition state during the formation of active zinc sites, but too much of a confined environment entropically jeopardizes the formation of such sites. Hence, we observe no $Zn(OH)^+$ sites formation on mesoporous catalysts.

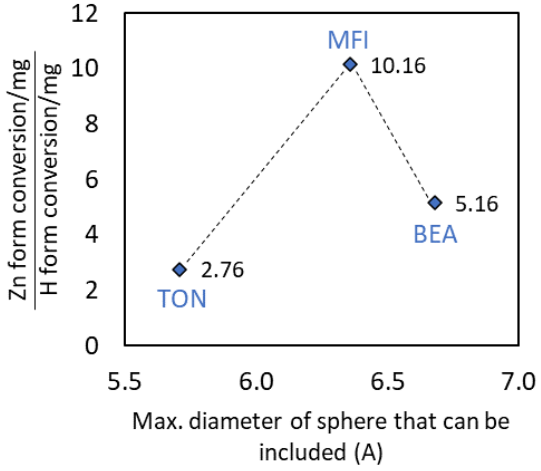

Figure 3.8. Activity enhancement of zinc addition vs. pore size of zeolite samples.

Analyzing product distributions (see Table 3.2), it is evident that Zn increases the selectivity towards aromatics for all samples, likely due to the higher availability of olefins for oligomerization and aromatization reactions when Zn is present. The benzene selectivity is highest on intermediate pore sizes (Zn-MFI and Zn-BEA), whereas bigger cavities seem to favor alkylbenzenes – Zn-CHA presents only 32% of the total carbon injected as C_6^- compounds, likely favoring toluene and other alkylaromatics.

Table 3.2. C_6^- compounds quantified in the online GC after reaction over the total amount of nC_6 injected, and benzene selectivity for hexane cracking pulses at 480 °C.

	C_6^- compounds /nC_6 injected (%)		Benzene selectivity (%)	
	H	Zn	H	Zn
TON (32.5-40)	98	98	0	7
MFI (11.5)	93	58	0	25
MFI (40)	96	71	0	22
MFI (140)	72	77	0	17
BEA (150)	93	82	0	18
MOR (10)	91	84	0	2
CHA (10-15)	88	32	0	0
FAU (2.6)	97	94	0	1
FAU (15)	98	77	0	2

3.3.3. Aging effects on Zn-ZSM-5

The effect of ambient conditions over storage time was assessed for Zn-ZSM-5 that had been prepared by PE 5% ZnSt decomposition and subsequent regeneration at 500 °C for 2 hours. IPA-TPRx (Figure 3.9) reveals that the $Zn(OH)^+$ sites are metastable, and the Zn seems to be mobilized over time, migrating out of the vicinity of the Al atom and forming another species. Immediately after preparation, the peaks corresponding to $Zn(OH)^+$ sites (2^{nd} and 3^{rd} peaks in Figure 3.9) correspond to 56% of the total area of the propylene curve; after 6 months of storage

in ambient conditions, this number decreased to 25% of the total. It is noteworthy that the total number of BAS remains unchanged. As Zn migrates, the original Brønsted acidity (referred to 1st peak) is restored proportionally.

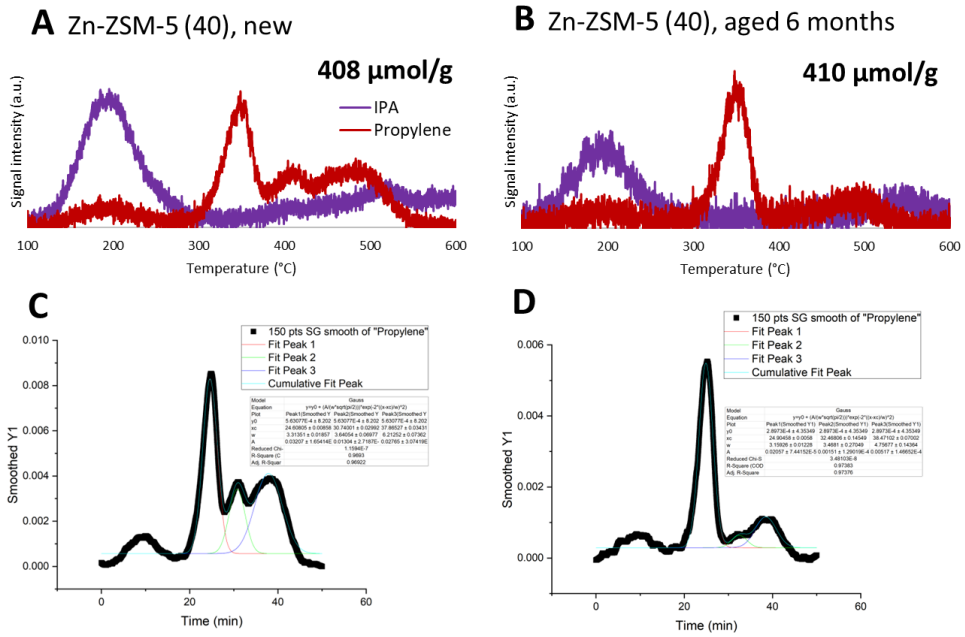

E

	Zn-ZSM-5, new	Zn-ZSM-5, 6 months
1st peak	180	309
2nd peak	73	23
3rd peak	155	78
Total (umol/g)	408	410

Figure 3.9. IPA-TPRx profiles and BAS density results for: (A) Zn-ZSM-5 freshly prepared from PE 5%ZnSt decomposition and subsequent regeneration, and (B) Zn-ZSM-5 after 6 months of storage at room temperature and pressure. (C) and (D) display the peak deconvolution for samples shown in (A) and (B), respectively. (E) Number of BAS corresponding to each of the three peaks present in both samples.

The $Zn(OH)^+$ sites count decrease over time is accompanied by a concomitant decrease in the catalyst activity. Figure 3.10 compares high density polyethylene decomposition curves in the TGA at 380 °C, thermally and over 5% ZSM-5, Zn-ZSM-5 (fresh), and Zn-ZSM-5 aged for 6 months. The rates of decomposition over the aged Zn-ZSM-5 are lower than over the fresh Zn-ZSM-5, and the aged sample displays a performance more similar to the parent sample H-ZSM-5.

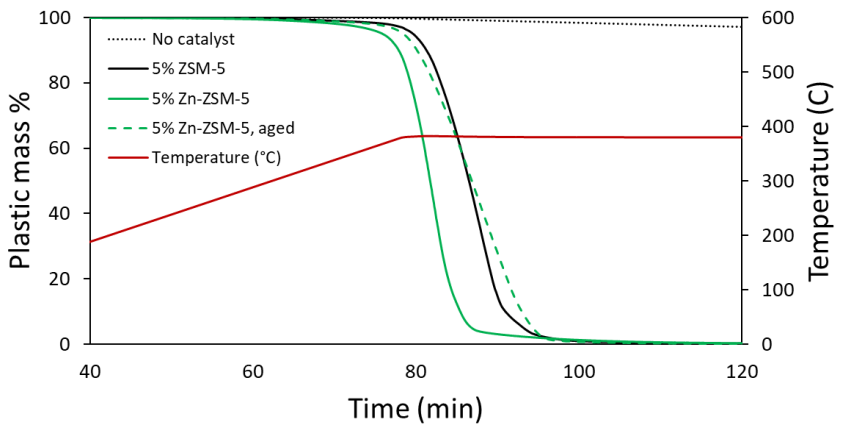

Figure 3.10. TGA decomposition profiles comparing HDPE decomposition over: no catalyst, 5% ZSM-5, Zn-ZSM-5 and 6-month aged Zn-ZSM-5. Reaction temperature = 380 °C, ramp rate = 5 °C/min.

These findings show that Zn speciation and location appear to be changing over time under ambient conditions. One possible reason for this might be that water molecules from ambient moisture are able to hydrolyze $Zn(OH)^+$ sites into different Zn species that rearrange in the zeolite framework, exposing the original BAS once again. A similar phenomenon has been reported to occur in phosphorus species on zeolites which were exposed to ambient moisture – see Appendix.

This change in activity accompanied by the disappearance of $Zn(OH)^+$ also indicates that the Zn contained in these species might be the major responsible for dehydrogenation activity, which is in agreement with recent reports that show that $Zn(OH)^+$ is highly active for propane dehydrogenation.[73] We speculate that aging in the presence of moisture causes $Zn(OH)^+$ species to be mobilized and form zinc oxide clusters, which are much less active for hydrogenation/dehydrogenation. Nonetheless, further studies are necessary to confirm this hypothesis.

3.4. Conclusions

The findings in this work reveal that Zn impregnation did not create active $Zn(OH)^+$ on mesoporous acid catalysts (ASA, mullite) even though these samples initially presented Brønsted acidity, similarly to zeolites. $Zn(OH)^+$ sites formed after Zn deposition on zeolites are highly active for dehydrogenation reactions[73]. When performing alkane cracking reactions, these $Zn(OH)^+$ sites generate olefins in-situ. Olefins can then be directly protonated into carbenium ions, avoiding the highly energetic carbonium ion pathway, thus requiring lower energies to be activated on Brønsted acid sites. This hydrocracking-like mechanism results in much increased rates of alkane cracking for Zn-exchanged zeolites when compared to non-exchanged samples.

However, Zn likely deposits mostly as zinc oxide on mesoporous catalysts, having detrimental effects to their alkane cracking activities instead of increasing rates of reaction. We showed that Zn is able to form active sites and improve activity and selectivity towards aromatics over zeolites regardless of pore size, although there seems to be an ideal pore size range to maximize the improvement in activity after zinc deposition.

Finally, we show that active $Zn(OH)^+$ sites formed in ZSM-5 are metastable, and they undergo rearrangement under storage conditions over the course of months. This process results in a shift in catalytic performances, yielding results more similar to the parent zeolite before Zn deposition.

Chapter 4: Effect of branching and unsaturation for polyolefin upcyling

4.1. Introduction

Although the chemistry of catalytic polymerization has been studied for several decades [74], the field of depolymerization is much less explored and has only gained a great deal of attention in the past few years. [75] Catalytic decomposition of waste plastic presents new challenges – and opportunities – to the industry. Important questions include whether macromolecules will readily react over catalysts that were traditionally designed to convert much smaller molecules, and what polymer properties govern such reactions.

Regarding non-catalytic pyrolysis, high density polyethylene (HDPE) and low density polyethylene (LDPE) generally display similar decomposition curves, but HDPE tends to require slightly higher temperatures to be decomposed. [76] Marcilla et al. compared the reactivity of HDPE and LDPE over ZSM-5, and found that LDPE decomposed at faster rates. [77] This result was attributed to the fact that LDPE branches were able to penetrate the zeolite pores, thus increasing the activity. Uddin et al. also reported that LDPE and linear low density polyethylene (LLDPE) degraded at faster rates than HDPE over solid acid catalysts. [78]

Zeolites have been extensively researched as catalysts to decompose polymers into short chain molecules. [79-83] It is important to notice that these are microporous materials, which, along with the fact that polymers are macromolecules and form highly viscous melts, implies in strong mass transfer constraints.[84] The structural properties of polyolefins, such as the branching degree and their length, can play an important role on granting access to different active sites in microporous catalysts. Aguado et al. showed that nanocrystalline ZSM-5 presented enhanced

activity for polyethylene conversion when compared to standard ZSM-5 [85], indicating that higher external surface area, and its consequent enhancement in diffusion, is an important factor for polyolefin conversion.

The mechanisms by which polyolefin upcycling reactions happen over a porous acid catalyst surface should be governed by the same energetics that define alkane cracking, due to their similar chemical nature. Polymers are, however, orders of magnitude higher in molecular weight than alkanes commonly studied in the literature. Hence, polymer decomposition reactions are expected to be heavily influenced by external and internal diffusion limitations, and the influence that double bonds and tertiary carbons actually exert on the reaction rates should be reassessed for such molecules. One may expect that the presence of branches in polyethylene will enhance rates of cracking over acid catalysts, since tertiary carbons are known to generate more stable transition states when compared to secondary carbons.[32] However, branches will also hinder diffusion of the main polymer chain into the catalyst pores – on the other hand, if they are long enough, branches may separately diffuse into different pores.

The inherent presence of double bonds would also be expected to increase reaction rates over acid catalysts, since the activation energy for protonating olefins is lower than that for protonating paraffins due to higher proton affinities.[29] Conk et al. have recently demonstrated partial dehydrogenation of polyethylene as a strategy to induce C-C bond cleavage, providing a promising pathway to produce propylene from waste plastic.[86]

Finally, another factor that will influence the rates perceived for polymer decomposition is the molecular weight. It has been observed that higher molecular weights result in lower catalytic reaction rates.[87-89] This could be due to higher viscosities associated with higher molecular weights and lower diffusion rates throughout the polymer melt. This work aims to understand what

role the degrees of branching and unsaturation play on the reactivity of polyolefins over acid catalysts.

4.2. Experimental

4.2.1. Polymer samples

Additive-free HDPE (M_n ~20,000 Da) and LLDPE (M_n ~48,000 Da) samples were provided by Chevron Phillips Chemical in powder form. For the analysis of the effect of unsaturation, *hydrogenated HDPE* was prepared. The hydrogenation reactions were carried out in a Parr batch reactor equipped with a Teflon liner and a turbine-type impeller. Plastic, solvent and catalyst – 1.2 g HDPE, 40 g cyclohexane (suitable for HPLC, ≥99.9%, acquired from Sigma Aldrich) and 600 mg Pd/Al_2O_3 (0.5 wt% Pd, 3.2 mm pellets, acquired from Sigma Aldrich) – were added to the reactor and the system was flushed with hydrogen. The reactor was pressurized to 300 psig H_2, stirring was set to 350 rpm, and the temperature was slowly ramped up to 150 °C. After the system reached the set temperature, the reaction was allowed to proceed for 1 h, under a total pressure of 380 psig. After quenching, the reactor was depressurized, and the catalyst pellets were separated out. Finally, the resulting hydrogenated HDPE was separated from the solvent, and dried overnight in a vacuum oven at 60 °C.

4.2.2. Polymer characterization

Molecular weights (MW) and molecular weight distributions (MWD) were obtained from high temperature gel permeation chromatography (GPC) using a PL 220 high temperature GPC/SEC unit (Agilent). Samples were dissolved in 1,2,4-tricholorobenzene (TCB) by heating at 150 °C for about 4 hours with gentle, occasional stirring. BHT (2,6-di-tert-butyl-4-methylphenol) at a concentration of 0.5 g/L was used as a stabilizer in the TCB. An injection volume of 400 µL

was used with a nominal polymer concentration of 0.5 mg/mL and a flow rate of 1.0 mL/min was maintained. Three Waters Styrogel HMW-6E columns were used and were calibrated with the integral method using a broad linear polyethylene standard (Chevron Phillips Chemical's Marlex® RTM BHB 5003 polyethylene resin) for which the molecular weight distribution had been determined. An IR4 detector (Polymer Char, Spain) was used for the concentration detection.

The concentration of various types of unsaturation in the polymer samples were quantified by a method based on proton nuclear magnetic resonance (NMR).[90-92] Polymer samples for NMR data collection were prepared by dissolving polymer powder samples in deuterated 1,1,2,2-Tetrachloroethane-d_2 (TCE-d_2, ≥ 99.5 atom %D). 0.035 g of powder of the polymer samples were added to 0.7 ml of TCE-d_2 solvent in a 5mm NMR tube. The sample and solvent mixture was heated in a heating block at 130 °C for 4 – 5 hours. The mixture was occasionally stirred with a stainless-steel stirrer to ensure homogeneous mixing. The resulting solution was then left overnight (for 15-16 hours) in the heating block at 110 °C to ensure complete disentanglement of the polymer chains. The final concentration of the sample solutions was ~3.0 wt%. The NMR data were collected at 125 °C (398K) in the Bruker 500 MHz NMR instrument fitted with a Bruker 5 mm BBI probe which was equipped with z-gradient. The sample was equilibrated inside the probe at 125 °C for 15 minutes before starting the data collection. Regular proton NMR data was collected with *zg* pulse sequence from Bruker's pulse program library using the following acquisition parameters: 5.0 s relaxation delay, 7.4 μs pulse width, 14 W pulse power, 4 dummy scans, 5.0 s acquisition time, 1024 scans and 9 ppm spectral window. The pre-saturation proton NMR data was collected with *zgpr* pulse sequence using the following acquisition parameters: 5.0 s relaxation delay, 7.4 μs pulse width, 14 W pulse power, 2.74×10^{-5} W pre-saturation pulse power, 4 dummy scans, 5.0 s acquisition time, 1024 scans and 20 ppm spectral window. The transmitter offset was

placed at the center of the proton peak arising from the backbone proton atoms of polyethylene (PE) for efficient suppression of that peak. This PE backbone peak appears at ~1.35 ppm. All the data were processed with 0.3 Hz line broadening, zero filled with 4X of time domain data points and referenced to the residual proton peak of TCE-d_2 which was calibrated at 6.0 ppm. The data were collected and processed with Bruker's Topspin software (version 3.2 pl 6).

For ^{13}C NMR data collection, 0.55 g of polymer sample was dissolved in a mixture of 1,2,4-trichlorobenzene (TCB) and 1,4-dichlorobenzene-d_4 (DCB-d_4) solvents to achieve a concentration of ~10 wt%. The ^{13}C NMR spectra of the polyethylene samples were collected with standard pulse program using the standard parameter set including: a 13.0 µsec 90° pulse width, a 21.7 kHz spectral window, 7.0 sec relaxation delay, 3.0 sec acquisition time. 8k transients were collected in an overnight experiment and full NOE was exploited during data collection to improve the S:N ratio at a reasonable amount of time. The data was zero filled to 131k data points and exponentially weighted with a 1.0 Hz line-broadening before Fourier transformation. The spectrum was referenced to backbone -CH_2- peak which was calibrated at 30.0 ppm.

4.2.3. Catalyst samples

NH_4-ZSM-5 catalysts (framework type MFI), with Si/Al = 40 (CBV 8014) and Si/Al = 140 (CBV 28014), were obtained from Zeolyst International. To render them acidic, the zeolites were calcined under 40 ml/min of air (80% N_2 / 20% O_2) at 600 °C for 5 hours, with a ramp rate of 2 °C/min. When used in flow reactors, the H-ZSM-5 was pelletized between 250 and 425 microns.

In order to assess diffusion properties, a core-shell zeolite (active ZSM-5 core, inert silicalite shell) was prepared based on the procedure described by Ghorbanpour et al. [93] In our work, however, we used Zeolyst MFI seeds to grow the silicalite layer, instead of synthesizing the

zeolite entirely. Also, the annealing step was not performed, which considerably lowers the time necessary for this sample preparation. 750 mg of NH_4-ZSM-5 (Si/Al = 40) were added to a dilute growth solution – 1.3 ml tetraethyl orthosilicate (TEOS) 98 %, and 2.8 ml tetrapropylammonium hydroxide 40 % in 65 ml of water, in which TEOS was added dropwise –, and left reacting at 100 °C for 24h in a rotisserie oven. The mixture was then centrifuged, and the zeolite was washed with deionized water 5 times. The solids were dried in a vacuum oven overnight at 80 °C, and subsequently calcined under 40 ml/min air flow according to the following temperature program: 1 hour isothermal at 350 °C (ramp rate = 1 °C/min) to clean the surface of any remaining water, followed by 5 hours at 600 °C (ramp rate = 2 °C/min). The resulting catalyst is referred to as *ZSM-5@Silicalite-1*.

Amorphous silica-alumina (ASA) catalyst support grade 135, Si/Al = 6, was obtained from Aldrich and used as received.

4.2.4. Catalyst characterization

The number of Brønsted acid sites (BAS) in the catalysts was determined by isopropylamine temperature-programmed reaction (IPA-TPRx) – the detailed procedure has been reported elsewhere.[94] Zeolites were imaged by a Zeiss Neon 40 EsB scanning electron microscope (SEM).

Nitrogen physisorption analysis was conducted using a TriStar II 3020. The samples were degassed under vacuum at 350 °C (ramp rate of 5 °C/min) for 10 h to remove moisture and volatile impurities. The catalyst weight was measured after degassing, and the samples were cooled down under liquid nitrogen for the adsorption-desorption analysis. Total surface areas and external

surface areas were calculated using the Brunauer-Emmett-Teller (BET) method and the t-plot method, respectively.

To verify the formation of the silicalite shell on ZSM-5, two probe reactions were performed in a flow reactor: acetic acid ketonization at 320 °C, and triisopropylbenzene (TIPB) cracking at 400 °C. The reactor consisted of a 0.25-in. OD quartz tube in a furnace, and the products were analyzed in a Hewlett Packard 6890 gas chromatograph (GC) equipped with an INNOWax column (30 m x 0.25 mm x 0.25 µm) and a flame ionization detector (FID). Both inlet and outlet lines were heated to avoid condensation of reactants and products. Reactions were performed under a 62.5 ml/min flow of helium and using 35 mg of fresh catalyst. W/F was 0.2 h for TIPB cracking, and 0.3 h for acetic acid, where F is the reactant feed rate. The zeolites were pretreated under the same flow of helium at the reaction temperature for 1 hour prior to the reaction start.

4.2.5. Polymer decomposition reactions

Reactions were carried out in a NETZSCH STA Jupiter 449 F1 thermogravimetric analysis (TGA) system, under 40 ml/min flow of argon. Catalyst powder, when used, was added to the bottom of the Al_2O_3 pan, and 20 mg of polymer sample were added on top of the catalyst.

For the product distribution analysis, 20 mg of polymer were mixed with the catalyst and packed in a quartz micropyrolysis tube. The micropyrolysis tube was then inserted into a 0.25 in. OD quartz tube, which was placed in a horizontal reactor furnace. This setup allows for the carrier gas to flow around the micropyrolysis tube, avoiding the polymer melt to plug the tube, which could cause overpressure. N_2 was used as the carrier gas, at a flow rate of 40 ml/min. The reactor temperature was increased from room temperature to 350 °C at a ramp rate of 2 °C/min, and the

final temperature was held for 30 minutes. Gas bags were used to sample evolved products downstream of the reactor, and no condensation was observed in the bags after sampling. The gas samples were analyzed in a Shimadzu QP2010 GC-FID/MS system, equipped with a HP-PLOT/Al_2O_3/S column.

4.3. Results and Discussion

4.3.1. Effect of branching on reactivity

The results of polymer samples characterization can be found in Table 4.1. HDPE and LLDPE were chosen to assess the importance of branching in the decomposition reaction due to their disparity in short chain branching (SCB): 0.7 vs. 16.6 per 1000 total carbon atoms. Hence, LLDPE has ~24 times more tertiary carbons per mole of carbon than HDPE does.

Table 4.1. Polymer samples characterization. Short chain branching (SCB) and M_n were calculated from ^{13}C-NMR data. M_n was determined via GPC, and unsaturation values were calculated from proton NMR data.

				Unsaturation /10^6 C				
Sample	**SCB** /1000 C	**M_n** (Da)	**M_w** (Da)	Vinylene −CH=CH− *internal*	Trisub −C=CH− *internal*	Vinyl −CH=CH2 *terminal*	Vinylidene −C=CH2 *terminal*	**Total**
LLDPE	16.6	48,190	112,150	108	87	40	15	250
HPDE	0.7	20,263	157,170	728	4	175	0	907

Figure 4.1 shows the decomposition curves for HDPE and LLDPE at a temperature ramp rate of 5 °C/min up to 500 °C followed by holding the final temperature for one hour. It can be noticed that, when comparing thermal decomposition curves for both samples, LLDPE depolymerizes slightly faster than HDPE. This is likely because tertiary alkyl radicals are more stable than secondary alkyl radicals, and the rate limiting step for thermal pyrolysis is usually the initiation step [95] – hence, rates are slightly faster for the branched polymer.

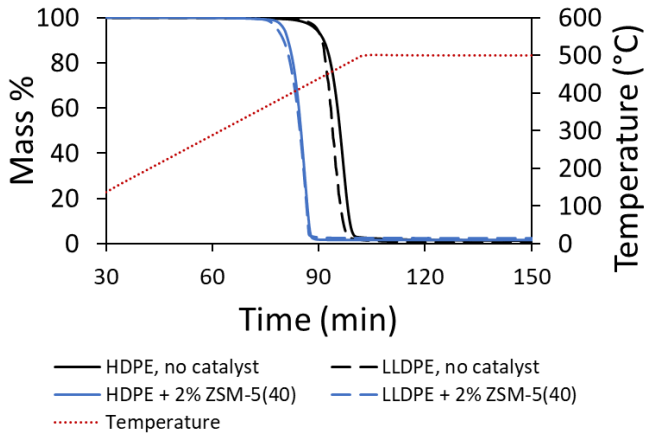

Figure 4.1. TGA curves for HDPE (full lines) and LLDPE (dashed lines) decomposition under inert environment, thermally (black lines) and over 2% ZSM-5 (Si/Al = 40, blue lines). Ramp rate = 5 °C/min up to 500 °C, followed by a 1-hour isothermal.

The addition of 2% catalyst reduces the temperature of maximum degradation by ~50 °C for both samples. However, the HDPE and LLDPE decomposition curves still overlap, indicating no significant difference in rates between these samples. Our group has discussed in a previous work [94] that performing polyethylene depolymerization at this ramp rate up to high temperatures (500 °C) did not allow for differences among catalysts to be noticed in the decomposition curve. Similarly, in this case, working at high temperature does not allow us to perceive differences in rate between these polyethylene samples.

The temperature ramp rate was then decreased to 2 °C/min, and the final (hold) temperature set to 350 °C. At this temperature, no significant decomposition occurs in the absence of catalyst, as can be seen in Figure 4.2 (A and B). Three different acid catalyst samples – ZSM-5 (Si/Al = 40 and 140) and ASA – were used to decompose the two polyethylene samples. The catalyst loading was adjusted for each catalyst so that all the experiments were run with the same total number of Brønsted acid sites, as measured by IPA-TPRx (Figure 4.2.C).

The results from Figure 4.2 (A and B) display different behaviors of catalytic degradation for both polymer samples. HDPE shows much lower conversion to gases than LLDPE after 1 hour at 350 °C: HDPE reached 14% conversion over ZSM-5 (40), 42% over ASA, and 61% over ZSM-5 (140); whereas LLDPE reached 91% conversion over ZSM-5 (40), 92% over ASA, and 82% over ZSM-5 (140). An interesting aspect of these experiments is that the activity of the catalysts followed different trends when using different reactants. For instance, ZSM-5 (140) was the most effective catalyst to convert HDPE; however, when used to decompose LLDPE, ZSM-5 (140) was the least effective catalyst. For easier comparison, curves for both polymer samples according to the type of catalyst are plotted in Figure 4.3.

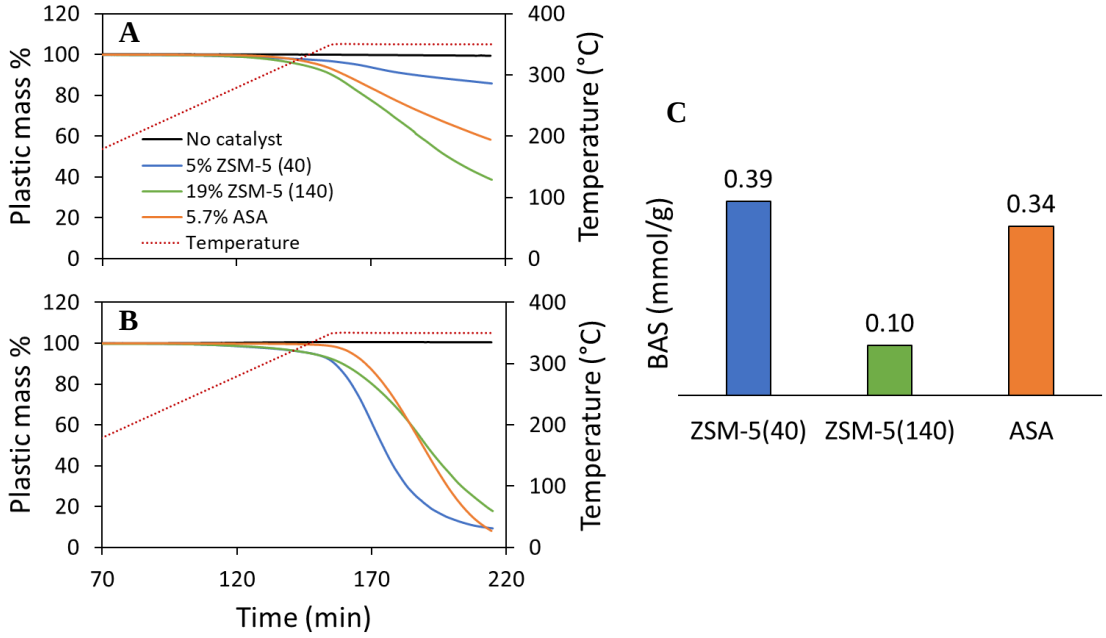

Figure 4.2. TGA thermal and catalytic decomposition curves for (A) HDPE, and (B) LLDPE. Temperature ramp rate = 2 °C /min up to 350 °C, followed by a 1-hour isotherm. (C) Brønsted acid site density measured by IPA-TPRx.

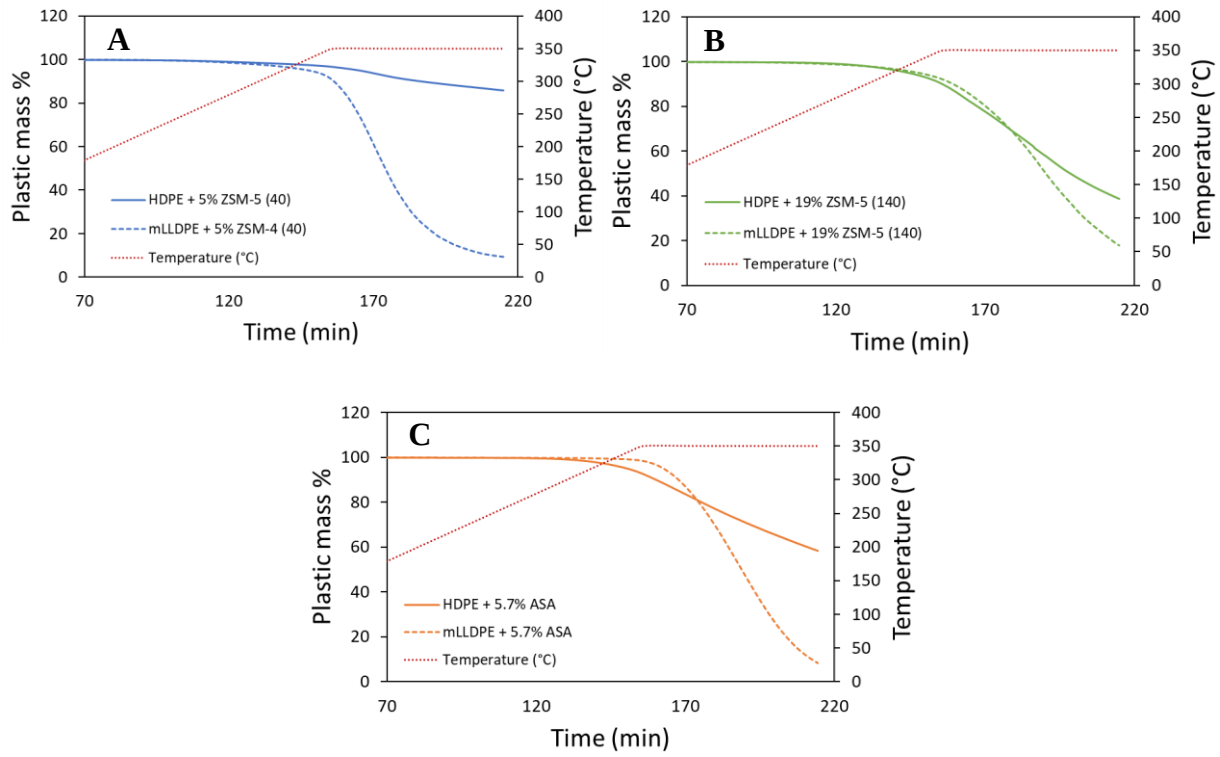

Figure 4.3. TGA decomposition curves comparing HDPE and mLLDPE over (A) ZSM-5 (40), (B) ZSM-5 (140), and (C) ASA. This is the same data shown in Figure 4.2, but organized by catalyst for clarity.

The HDPE curves suggest that cracking may be related to the total surface area available for the polymer to adsorb and react. Textural properties of the catalysts used can be found in Table 4.2. The effectiveness of the catalyst was correlated to the amount introduced to the system, and higher catalyst loadings (higher total surface areas) showed better performance. If we analyze the rates of weight loss (see Figure 4.4) after the temperature reaches the set point and before the inflection point of the TG curve, we notice that the rates of reaction are about 4.1 times faster over MFI (140) *vs.* MFI (40) – this value roughly corresponds to the ratio of catalyst mass added to the system (0.19/0.05 = 3.8), since their specific surface areas are similar. Also, ZSM-5(140) contains fewer aluminum atoms on the external layer, decreasing the overall polarity of the external surface for this catalyst when compared to ZSM-5(40). Therefore, a strongly non-polar molecule such as polyethylene should have better interactions with a less polarized surface, where ensuing

wettability and catalyst/polymer interaction is more favorable with Si/Al = 140 than with Si/Al = 40 which in turn will yield higher rates.

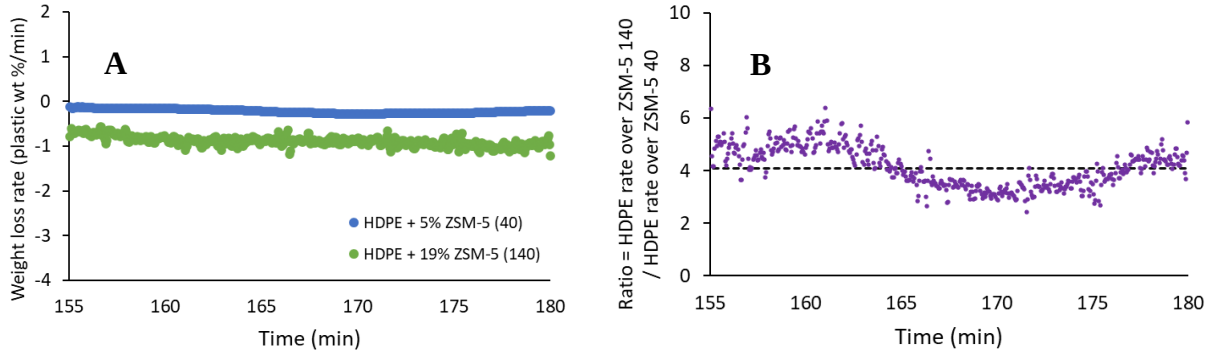

Figure 4.4. (A) Rates of weight loss (derivative of the TGA curve) for HDPE over ZSM-5 (40) and ZSM-5 (140). (B) Ratio of the rates over ZSM-5 (140) and ZSM-5 (40). Average = 4.09

Amorphous silica alumina (ASA), added in a similar amount as ZSM-5(40), presents faster rates that are not simply proportional to the catalyst mass and consequent available surface area. This enhanced activity may be explained either by its mesoporous nature or surface polarity, or a combination of the two. The mesoporous structure of the ASA samples eases diffusion of the polymer into the catalyst particles and allows HDPE to access more acid sites per unit time. It is also important to note that zoning in MFI catalysts is common, often resulting in higher Al concentrations near the surface than in the bulk of the crystal.[93, 96] This could imply that the exposed Al content on the MFI 40 catalyst near the surface could be a bit higher than the Si/Al ratio alone would suggest. Therefore, at a similar Si/Al ratio between MFI 40 and ASA, one might speculate that the surface Al content, and ensuing polarity on the surface may be higher for the former. This could result in decreased wettability with the hydrophobic HDPE polymer chains.

Table 4.2. Textural properties of acid catalysts.

Sample	BET surface area (m^2/g)	External surface area*	Total pore volume (cm^3/g)	Micropore volume* (cm^3/g)
ZSM-5(40)	398.6	113.8	0.231	0.128
ZSM-5(140)	372.7	111.2	0.224	0.114
ASA	509.4	556.9	0.666	0
ZSM-5(40)@Silicalite-1	384.1	106.8	0.205	0.119

*Obtained by t-plot method

LLDPE decomposition curves shown in Figure 4.2, although consistently presenting conversions above 80%, seem to be related to the nature of the catalysts used. Faster rates (steeper inclinations) are achieved with higher acid densities (ZSM-5 40 and ASA). Although ASA possesses acid site densities comparable to those of ZSM-5 (40), its mesoporous nature and arguably weaker BAS (due to its amorphous nature and consequently larger Si-O-Al angles [97] when compared to zeolites) modify polymer-catalyst interactions in such a way that the reaction onset takes longer to appear in the TG plot. It is possible, however, that cracking reactions are still happening at a similar rate but generating long-chain molecules that do not leave the polymer melt and thus cannot be detected by this technique, which would result in an apparent flat line in the TGA curve.

One possible explanation for such differences in decomposition curves according to the acid density of the zeolite might be, in fact, the density of external acid sites. As will be unveiled in Section 4.3.2, LLDPE decomposes mostly on external acid sites only, i.e., it is strongly internal mass diffusion limited. Aluminum zoning, which consists of aluminum being concentrated in the rim of the zeolite particle when compared to the bulk, is known to happen in TPA^+-templated crystals.[98, 99] Al zoning in the more acidic ZSM-5 40 should result in an external surface with very low Si/Al ratio, and the presence of more external acid sites may help explain the faster decomposition rates.

4.3.2. Effect of branching on internal diffusion

In order to assess the polymer's ability to diffuse into microporous catalysts, a core-shell ZSM-5 was prepared. The full procedure can be found in Section 4.2.3, in which an inert, thin silicalite shell was grown on NH_4-ZSM-5 seeds. The purpose of these samples is to help reveal whether the polymer decomposition reactions happen preferentially on the external surface of the catalyst, or the polymer has the ability to diffuse into the microporous channels of the catalyst and access the majority of the acid sites.

IPA-TPRx reveals that the BAS density of the ZSM-5@Silicalite-1 sample is 0.39 mmol/g_{cat}, which is the same acidity as the parent zeolite (see Figure 4.6). This, along with the practically unchanged BET surface area (see Table 4.2), suggests that there was no pore plugging due to deposition of silica. Also, the unchanged BAS density indicates that the silicalite layer is actually quite thin, as the formation of this layer did not add enough mass to decrease the BAS density of the sample. SEM images for ZSM-5 and ZSM-5@Silicalite-1 also support this claim since the average particle size (~1 micron) is unchanged, as shown in Figure 4.5.

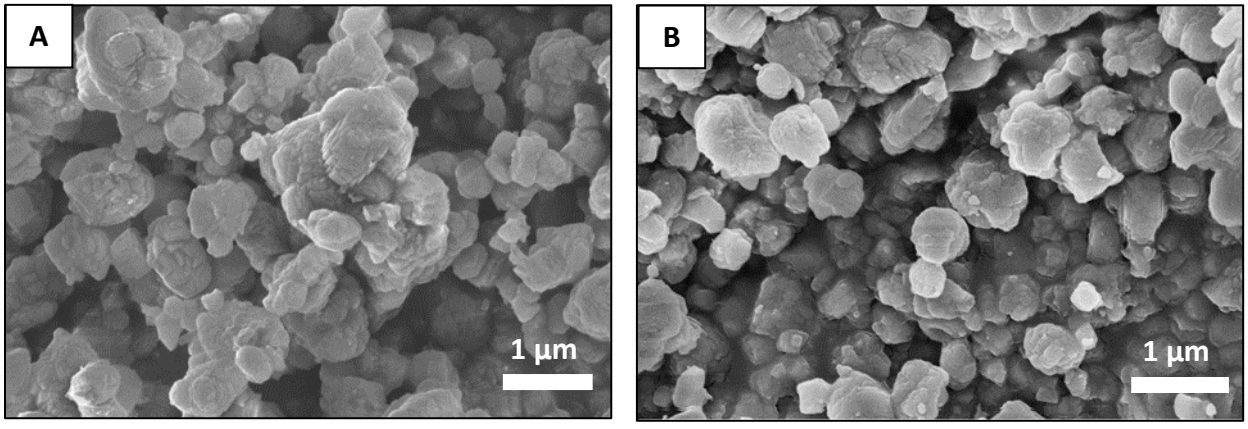

Figure 4.5. SEM images for (A) ZSM-5(40), and (B) ZSM-5(40)@Silicalite-1

Two probe reactions were used as proof of concept for the use of this ZSM-5@Silicalite-1: triisopropylbenzene (TIPB) cracking, which should occur only on the external sites of the catalyst due to shape selectivity constraints; and acetic acid ketonization, which should happen on any acid site of the zeolite since the reactants and products are significantly less bulky thus easily diffusing in and out of the catalyst particle. We note that these two probe reactions have been successfully employed previously to assess the content of internal vs. external acid sites in microporous materials.[93, 100] The turnover frequencies (TOF) for each of these reactions can be found in Figure 4.6. It is noticeable that the TOFs for TIPB cracking over ZSM-5@Silicalite-1 are much lower than the ones over ZSM-5, corresponding to only ~5% of the activity of the parent zeolite. This denotes that the external sites were successfully covered by the inert silicalite, and any activity on the external surface sites should be minimal. On the other hand, the TOFs for acetic acid ketonization are quite similar between the two catalysts: the activity over ZSM-5@Silicalite-1 was, on average, 90% of that over the parent zeolite. This small difference in activity may be due to mass-transfer limitations caused by pore narrowing due to silica deposition.

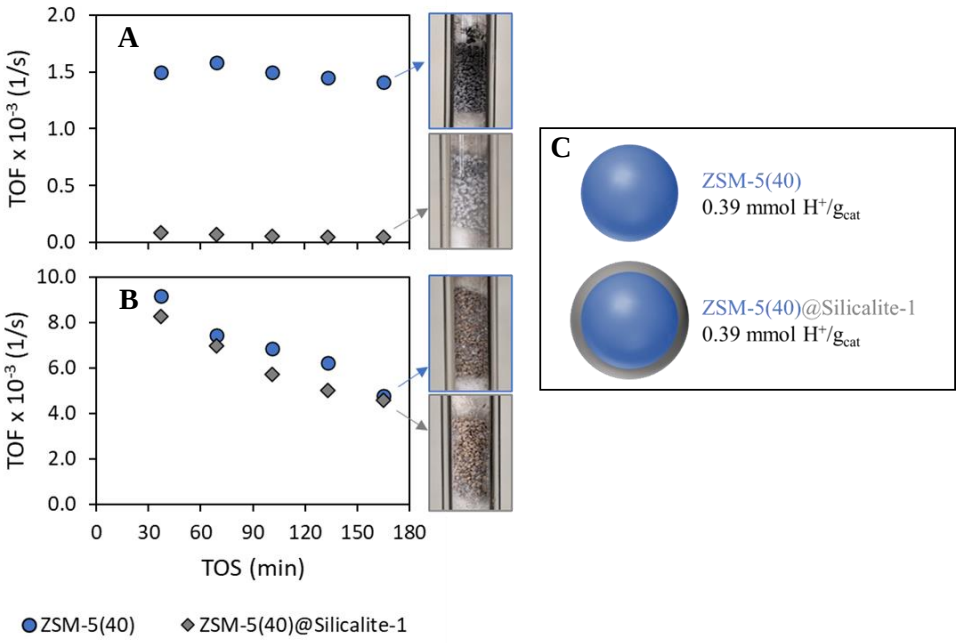

Figure 4.6. Turnover frequencies (TOF, 1/s) vs. time on stream (TOS, min) in a flow reactor for (A) TIPB cracking at 400 °C, and (B) acetic acid ketonization at 320 °C. (C) Visual representation of ZSM-5 and ZSM-5@Silicalite-1 (thickness of inert external shell is exaggerated for better visualization), and the BAS densities as measured by IPA-TPRx.

When used to catalyze the polymer decomposition reaction, ZSM-5@Silicalite-1 shows two different behaviors for the different PE samples. As can be seen in Figure 4.7, HDPE displays nearly identical decomposition curves over regular ZSM-5 and the core-shell catalyst. This indicates that the external layer is not the only surface where the cracking reactions take place: if the polymer molecules can reach any acid site in the zeolite (internal or external), then the total rate should be dependent mostly on the internal sites, as they are more numerous than external ones. Hence, it can be concluded that this HDPE sample can successfully diffuse into the zeolite pores prior to cracking into smaller molecules.

The LLDPE sample, though, displays strikingly different rates over ZSM-5@Silicalite-1 vs. ZSM-5. Whereas the parent zeolite is able to reach 91% conversion to gases after 1 hour of reaction, the silicalite shell catalyst is only able to reach 16% conversion by the end of the

experiment. These curves denote that most of LLDPE decomposition reactions occur on the external sites of the zeolite, since the reaction is much suppressed when the external layer consists of inert silica.

One interesting finding that can be inferred from these experiments as well is the fact that the HDPE and LLDPE TGA profiles appear to be so similar over the silicalite-1 coated catalysts. Because we know that: a) the intrinsic kinetic constant for LLDPE conversion over acid sites is significantly higher than HDPE conversion over acid sites, and b) the rate observed in these materials is proportional to both the rate constant and diffusivity of the polymer within the pores; one might infer that the rate of diffusion of HDPE through the hydrophobic silicalite shell, and possibly through the MFI framework, is faster than the LLDPE diffusion in hydrophobic MFI materials.

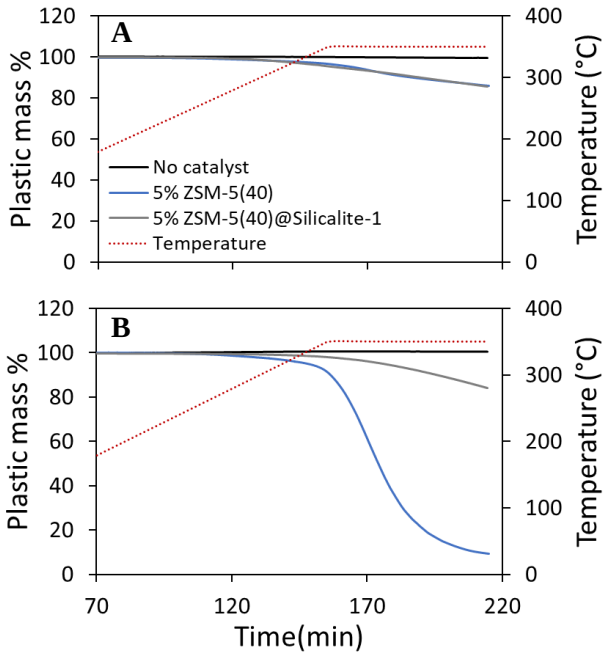

Figure 4.7. TGA curves for polymer decomposition over 5% ZSM-5 (40) and ZSM-5(40)@Silicalite-1 for (A) HDPE, and (B) LLDPE. Temperature ramp rate = 2 °C /min up to 350 °C, followed by a 1-hour isotherm.

It is important to note that the diffusivity of polymer chains through the polymer melt itself may also play an important role in these experiments – the polymer molecules need to be able to reach the catalyst surface. The self-diffusion coefficient tends to be slightly lower for LLDPE when compared to HDPE; also, diffusivity decreases as molecular weight increases.[101] Both of these correlations lead to the conclusion that the self-diffusivity of LLDPE is lower than that for HDPE. Nonetheless, LLDPE displays much higher reactivity when the zeolite external layer is catalytically active – denoting the high importance of tertiary carbons for perceived rates.

The product distribution over ZSM-5 (140) at 350 °C can be found in Figure 4.8. Products were comprised of olefins and paraffins in the range of C_2-C_7. No methane or aromatics were detected. Comparing the carbon number distributions, it is noticeable that the products from LLDPE are heavier than those coming from HDPE. This result is in agreement with the finding that HDPE is decomposed mostly in the internal BAS of MFI, whereas LLDPE decomposes primarily on the external surface. When bulky products are formed inside micropores, as is the case of the HDPE sample, there is a higher probability that they will further decompose into shorter chains during their diffusion out of the pores. [102] In contrast, when products are formed on external sites, they can easily diffuse out and move into the gas phase – this is likely the reason why the gas product formed from the decomposition of LLDPE is richer in the heavier fractions C_5, C_6 and C_7.

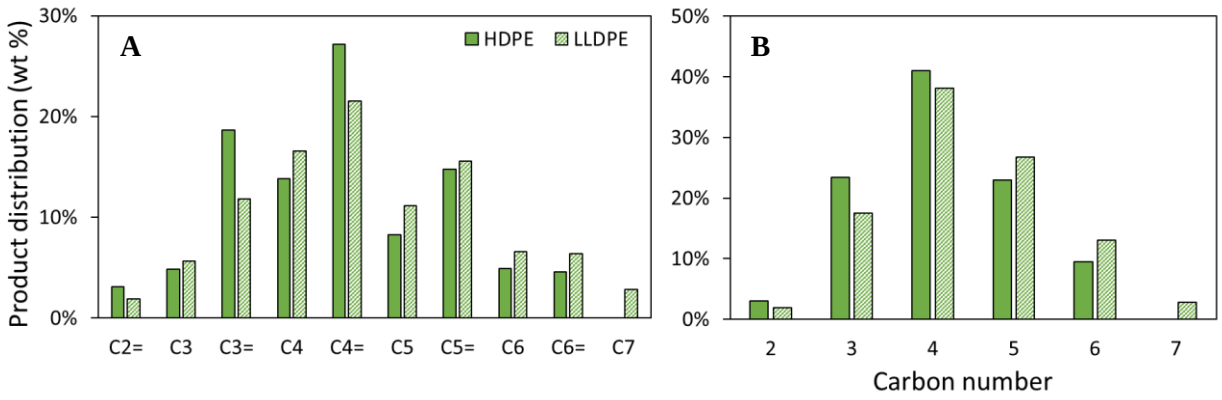

Figure 4.8. (A) Product distribution for polyethylene samples over 19% ZSM-5 (140) at 350 °C. (B) Product distribution lumped by carbon number. Temperature ramp = 2 °C/min up to 350 °C, final temperature held for 30 minutes. Gas products were sampled at the moment when the temperature reached 350 °C. Conversion to gases = 8% at these conditions, according to TGA data.

It can also be noticed that LLDPE produces more light alkanes (C_2-C_4) when compared to HDPE, which yields more light olefins. Total olefin-to-paraffin (O/P) ratio was 2.1 for HDPE, and 1.5 for LLDPE. In these reactions, olefins are formed via β-scission. It might be expected that β-scission would be faster for the branched LLDPE than for the linear HDPE, due to the presence of tertiary carbons, which would form more stable tertiary carbenium ions when compared to secondary carbenium ions in the HDPE. Nevertheless, it is important to notice that isomerization reactions should readily occur for both samples, generating tertiary carbenium ions in both reactions. The difference in structure of these polymers, if anything, would contribute to a higher O/P ratio in the LLDPE sample. However, what we observe is precisely the opposite: $O/P_{HDPE} > O/P_{LLDPE}$. Hence, what controls the O/P ratio difference must be a higher paraffin production in the LLDPE reaction.

There are two main pathways in acid catalysis to generate paraffins: protolytic cracking and hydride transfer.[103] Nonetheless, protolytic cracking is only kinetically relevant at high temperatures and very low concentrations of alkene.[31] The reactions depicted in Figure 4.8 were

performed at considerably low temperature (350 °C), and the concentration of olefins is significant at 8% conversion. Given that the formation of paraffins is then controlled by hydride transfer, one may conclude that hydride transfer occurs more significantly in LLDPE than in HPDE. This may be explained by the fact that branched hydrocarbons are better hydrogen donors than linear ones, since the resulting tertiary carbenium ion is more stable than a secondary one [104, 105]; hence, activation energies are lower for hydride transfer to occur when branched paraffins are present, as is the case of the LLDPE chains.

Based on the findings, Figure 4.9 summarizes the effect of short-chain branching in polyethylene reactions over ZSM-5 zeolites. Although the presence of tertiary carbons increases the perceived rate of decomposition, the presence of short-chain branches strongly hinders diffusion of the polymer molecules into the 5.5 Å-wide micropores of the catalyst. It must be noted that methyl shift isomerization occurs rapidly for both HDPE and LLDPE – comparing the product distributions, the iC_4/nC_4 ratio is 1.3 for both samples. However, methyl branches do not strongly hinder diffusion like the longer branches present in LLDPE do.

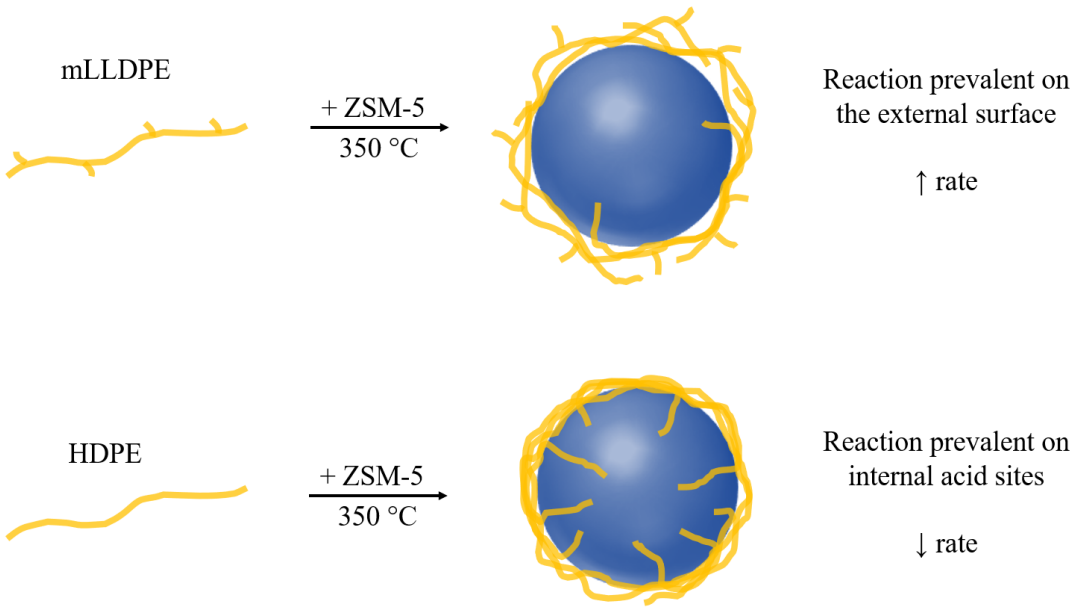

Figure 4.9. Effect of short chain branching on the diffusion of polymer molecules into zeolite micropores.

4.3.3. Effect of degree of unsaturation

To systematically study the role of the unsaturation inherently present in polyethylene samples, the HDPE sample was hydrogenated in order to generate a sample that had exactly the same properties as the original one (same molecular weight distribution and degree of branching) but contains a lower quantity of double bonds. MW characterization comparing the original and hydrogenated sample can be found in Figure 4.10 (A), and Figure 4.10 (B) shows that there is no change in the melting point of the polymer after hydrogenation – both indicating that the nature of the polymer seems to be unchanged except for the degree of unsaturation. The HDPE sample was chosen for this study because it was the one that presented the highest degree of unsaturation (see Table 4.1).

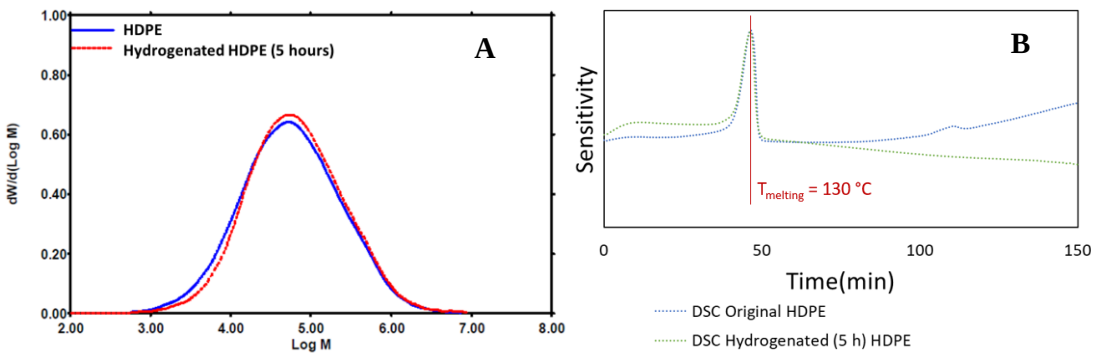

Figure 4.10. (A) GPC data comparing HPDE and 5-hour hydrogenated HDPE. (B) Differential scanning calorimetry (DSC) data (a.u.) acquired during TGA runs for HDPE and Hydrogenated HDPE. Melting point remains unchanged after hydrogenation reaction, showing that no significant hydrogenolysis happened, as lowering MW is expected to also lower the melting point.

Table 4.3 shows the NMR quantification of unsaturation in the original sample and the hydrogenated samples. Performing the hydrogenation reaction for 1 hour reduced the total amount of unsaturation in the sample by 78%. After 1 hour, the hydrogenation reaction seems to have achieved equilibrium, since performing the reaction for 5 hours yields the same total number of double bonds per 10^6 carbons. However, as the reaction is allowed to happen for a longer time, double bond isomerization decreases terminal vinyl groups and increases internal vinylene groups. This isomerization tendency has been previously reported in the literature when hydrogenating polyethylene samples via homogeneous catalysis.[106]

Table 4.3. NMR unsaturation quantification comparing the original HDPE and hydrogenated HDPE samples.

	Unsaturation /10^6 C				
Sample	Vinylene −CH=CH− *internal*	Trisub −C=CH− *internal*	Vinyl −CH=CH2 *terminal*	Vinylidene −C=CH2 *terminal*	**Total**
HDPE	728	4	175	0	**907**
Hydrogenated HDPE (1 hour)	102	0	98	0	**200**
Hydrogenated HDPE (5 hours)	137	0	68	0	**205**
Percent reduction after 1-hour reaction	*86%*	*100%*	*44%*	-	***78%***
Percent reduction after 5-hour reaction	*81%*	*100%*	*61%*	-	***77%***

Among the hydrogenated HDPEs, the 5-hour sample presented a vinyl/vinylene unsaturation ratio that was the closest to the original HDPE sample – this ratio was 0.24 for the original HDPE, 0.96 for the 1-hour hydrogenated HDPE, and 0.50 for the 5-hour hydrogenated HDPE. Therefore, TGA decomposition runs over 5% ZSM-5 were performed for the hydrogenated HDPE (5 hours), and the resulting curves can be seen in Figure. 4.11. The decomposition curves for the hydrogenated sample overlap with those of the original HDPE sample. This denotes that the presence of double bonds at the concentrations present in commercial polyethylene – about 1 double bond for every 1,100 carbons in the chain – is not the controlling factor in the acid-catalyzed pyrolysis. If this cracking reaction were governed by the protonation of unsaturated carbons, then the perceived rates for the hydrogenated samples should be proportionally lower.

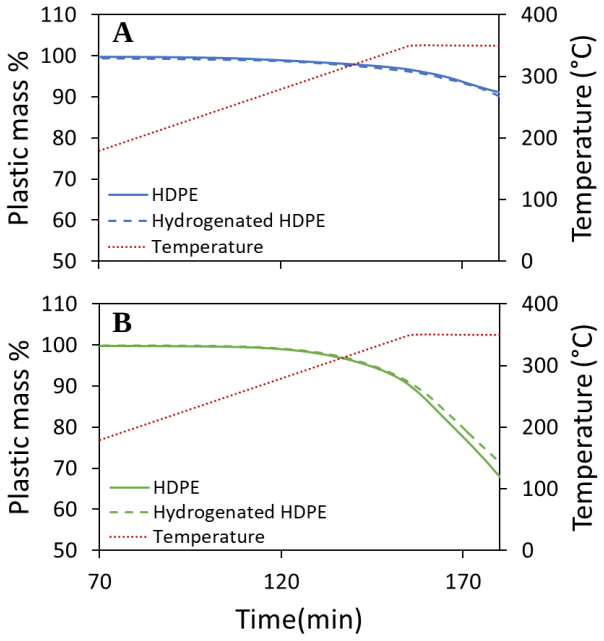

Figure. 4.11. TGA decomposition curves for HDPE and Hydrogenated HDPE (5 hours) over (A) 5% ZSM-5(40), and (B) 19% ZSM-5(140). Temperature ramp rate = 2 °C /min up to 350 °C, followed by a 30-min. isotherm.

These results may suggest that the cracking of HDPE molecules is not limited by protonation of the polymer chain, or that the rates measured are in fact diffusion rates – hydrogenating double bonds should not detrimentally influence the overall diffusivity of these molecules. Comparing this data to the results from Figure 4.6 (A), it is likely that the rates measured in Figure. 4.11 are in fact diffusion-controlled. Hence, removing double bonds does not affect the rate of weight loss.

4.4. Conclusions

We have compared HDPE and LLDPE samples for reactivity over ZSM-5 and amorphous silica alumina. LLDPE displayed much higher reactivity than HDPE, even though most cracking reactions for the linear low density sample occurred only on the external sites of the zeolite. HDPE decomposes mostly in the internal sites, but with much lower reactivity. The region where the cracking reactions take place (internal *vs.* external sites), in turn, is reflected in the product distribution arising from each of the polyethylene samples. LLDPE yields heavier and more paraffinic products, whereas HDPE generates lighter and more olefinic products. Further, comparison of rates over catalysts with varying surface properties suggests that the surface polarity influences polymer-catalyst interactions, with consequences on reaction rates, and that internal diffusion of HDPE is faster than LLDPE within the confined pores of MFI samples.

Hydrogenation experiments were carried out to determine whether the presence of double bonds governs the rate of catalytic cracking of HDPE. We found that lowering the unsaturation levels in the polyethylene sample had no discernible effect on the rate of decomposition.

These findings provide important insight into the factors that govern polyolefin reactivity over acid catalysts, which will support the development of more efficient and sustainable methods for chemically recycling or upcycling polymer waste.

Chapter 5: Strategies to improve polymer decomposition reactions

It has been shown in previous chapters, as well as in extensive literature on plastic recycling reactions, that polymer conversion over traditional catalysts presents many challenges. Most of them are related to the long chains inherent to these macromolecules, which become apparent as very high melt viscosities, and strong external and internal diffusion limitations when heterogeneous catalysts are employed. In this chapter, two strategies to improve reactivity and/or selectivity are presented and discussed: i) the use of carbon nanotubes to interface between catalyst particles and polymer melts, and ii) reactive distillation to narrow product distributions.

5.1. Nanotubes on ECAT

5.1.1. Introduction

It has recently been shown that high molecular weight polymers require much higher temperatures to undergo cracking over acid catalysts than low molecular weight ones.[107] This was attributed to the high viscosity of high MW polymer melts, which implies severe transport limitations and has been shown to impoverish polymer-catalyst contact. In situ optical microscopy observations of this trend are shown in Figure 5.1.

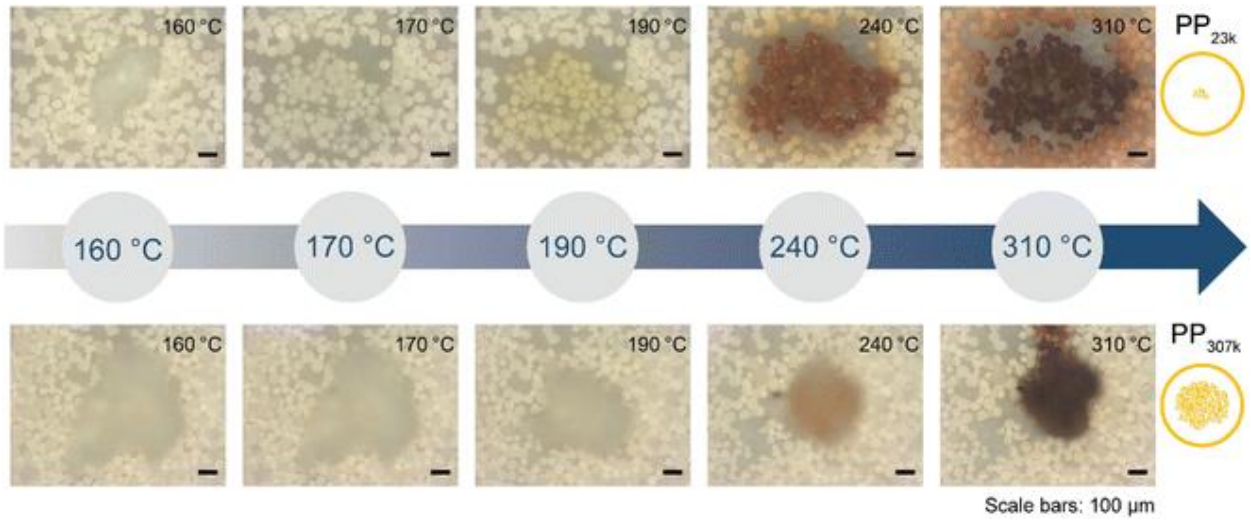

Figure 5.1. Visual indication that low molecular weight polypropylene (M_w = 23,000 Da) displays higher spreading wetting than high molecular weight polypropylene (M_w = 307,000 Da). Source: Ref. [107].

We propose that these different interactions depending on molecular weight are related not only to their zero-shear viscosities, but also to the surface energies of the polymer melts. Wetting depends on three interfacial tensions: solid-air, γ_{SA}; solid-liquid, γ_{SL}; and liquid-air, γ_{LA} (see Figure 5.2). When reaching equilibrium, the contact areas between phases are modified in a way to minimize the total free energy of the system.

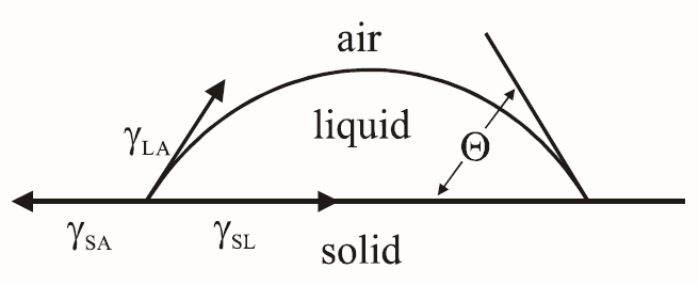

Figure 5.2. Force balance in wetting: $\gamma_{SA} = \gamma_{SL} + \gamma_{LA} \cos \theta$, where θ is the contact angle.

When comparing different MW polymers decomposition over a catalyst bed, the γ_{SA}, which is only dependent on the catalyst and the gas, remains unchanged. The γ_{LA}, on the other hand, is

known to increase with increased molecular weight of polymers.[108-110] Given this trend, it is assumed that the surface energy of higher MW polymers is also higher when compared to lower MW, which in turn may also change the γ_{SL}. This results in higher contact angles, which consequently means that high MW polymers will have more difficulty to spread on the catalyst bed and wet particles.

The study referenced in Figure 5.1 was carried out using equilibrium catalysts (ECAT) from the fluidized catalytic cracking (FCC) process. FCC catalysts are comprised of zeolites, amorphous silica alumina and clay. The ECAT consists of a mixture of differently aged catalyst particles that circulate in the FCC system. These catalysts still hold some acidity but have been considerably deactivated and present high levels of deposited metals due to the continuous contact with the feedstock.

Here, we propose an innovative approach in catalyst design to improve polymer-catalyst contact for depolymerization reactions. The ECAT external surface is composed mainly of aluminosilicates, which are not lipophilic. Since these catalysts inherently present metal particles on them, these metal centers can be used as catalysts for carbon nanotube growth. The goal is to cover the ECAT external surface with carbon nanotubes (CNT), which should present more favorable intermolecular interactions with polyolefins, that are comprised solely of carbon and hydrogen. The nanotubes could then be an attractive surface for polymers to adhere to and could serve as a "highway" for the polymers to diffuse into the catalyst and react with active acid sites.

5.1.2. Experimental

The ECAT sample, "as received", was calcined at 600 °C for 4 hours, under 40 ml/min air flow. The ramp rate used to achieve the calcination temperature was 2 °C/min. Calcination was

carried out to burn off residual coke that could jeopardize both acid and metal activities. This calcined sample will be referred to as *ECAT* henceforth. A visual comparison before and after calcination can be found in Figure 5.4 A.

Nanotubes growth over ECAT samples was performed in a 1 in. ID fritted quartz reactor at atmospheric pressure. 1 gram of ECAT material was added to the quartz tube, and the catalyst was pre-reduced at 850 °C for 30 minutes under 200 ml/min H_2 flow, using a ramp rate of 10 °C/min. The reactor was then cooled down to the reaction temperature of 675 °C under 200 ml/min N_2 flow. After the temperature stabilized at 675 °C, the N_2 flow ceased, and the reaction was initiated by starting 200 ml/min flow of ethylene into the system. The nanotube growth reaction was carried out for 30 minutes, and the reactor was subsequently cooled down under N_2 flow. After growth, the sample was calcined under 100 ml/min air flow at 450 °C for 12 hours to clean the surface from any amorphous carbon deposits that might have been formed during the nanotube growth (see Figure 5.3 for TGA indication that nanotubes should be preserved at 450 °C). This sample is henceforth referred to as *CNT-ECAT*.

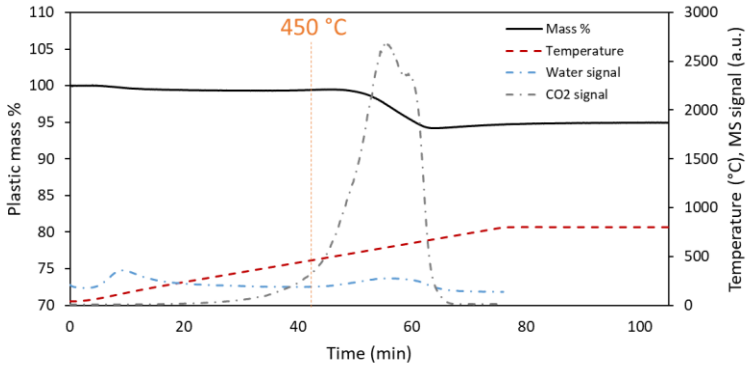

Figure 5.3. TGA analysis of CNT-ECAT under air flow, 40 °C to 800 °C at 10 °C/min, 1 hour isothermal at the final temperature. The curve illustrates that only amorphous carbon should be burned at 450 °C, whereas the carbon nanotubes are only decomposed at higher temperatures.

TGA experiments, as well as IPA-TPRx and SEM images were taken as described in Section 2.2. Here, in addition, gallium focused ion beam (FIB) milling was used to cut a cross section of a CNT ECAT particle.

5.1.3. Results and Discussion

Although some degree of particle size distribution is present, ECAT presents particles of about 50 µm diameter. Brønsted acid site density by IPA-TPRx was 0.021 mmol/g_{cat}. Pictures before and after calcination, as well as IPA-TPRx and particle size characterization can be found in Figure 5.4.

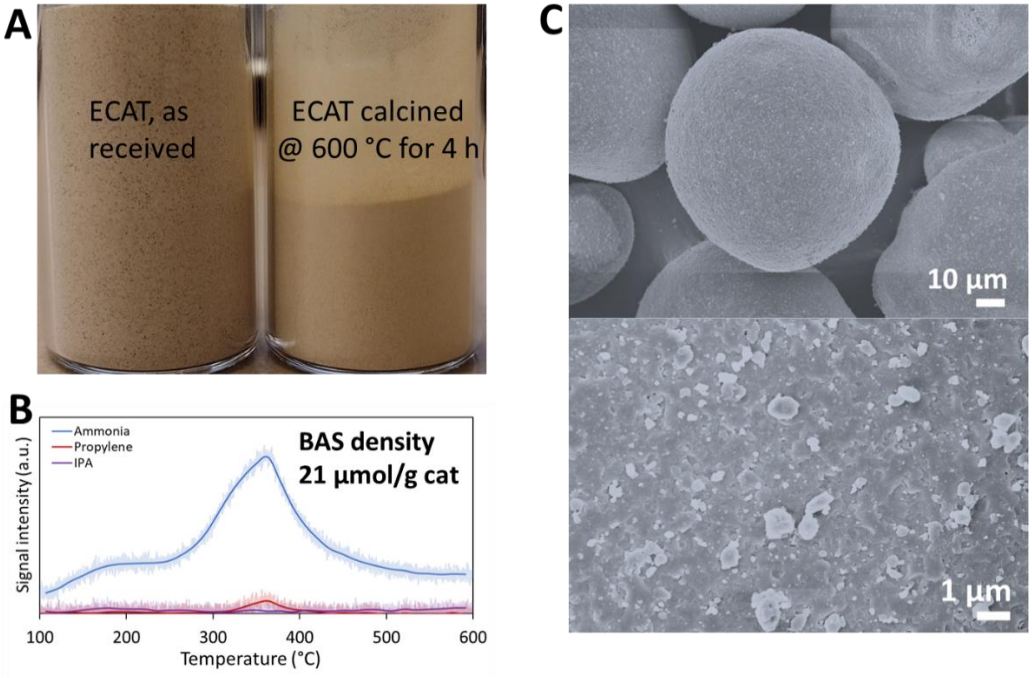

Figure 5.4. (A) ECAT as received and after calcination. (B) IPA-TPRx result for calcined ECAT. (C) SEM images showing approximate particle size and surface morphology.

Elemental composition of the sample was acquired by SEM-EDS, and Table 5.1 shows all identified elements. The main components of an FCC catalyst are aluminosilicates, hence the

elements in highest wt% are oxygen, aluminum, and silicon. Lanthanum is a common additive used in FCC catalysts, which improves the structural stability of zeolites and helps keep more aluminum in the framework.[60, 111] Iron, magnesium, titanium, calcium and sodium are contaminants present in the sample, which together account for 4.6 wt%. Nickel has not been found in enough concentration to be detected by this technique.

Table 5.1. Calcined ECAT elemental composition according to SEM-EDS.

Element	wt %
O	42.3
Al	27.2
Si	24.6
Fe	1.6
La	1.4
Mg	1.2
Ti	0.8
Ca	0.6
Na	0.4
Ni	0.0

Due to titanium's electron distribution, it would not be feasible to grow nanotubes over this surface. Titanium's coordination number is very low (group 4 in the periodic table), resulting in a higher d-band center energy and consequently higher bonding energies[112]. This results in too strong adsorption energies with adsorbates, thus not allowing for proper desorption and halting reaction rates. Hence, the only possible metal for nanotube growth in this ECAT sample is the iron surface.

After nanotube growth and calcination, it was attempted to separate catalysts according to their carbon nanotube content. Based on the separation procedure described by Briggs and Crossley[113], the CNT-ECAT was placed into a biphasic mixture of 150 ml dodecane and 150 ml water. Ideally, the particles containing fewer nanotubes should sink to the bottom of the beaker,

whereas nanotube-rich particles should sit at the oil-water interface. Nonetheless, the particles retrieved from the oil-water interface displayed no nanotubes upon inspection in the SEM – see Figure 5.5.

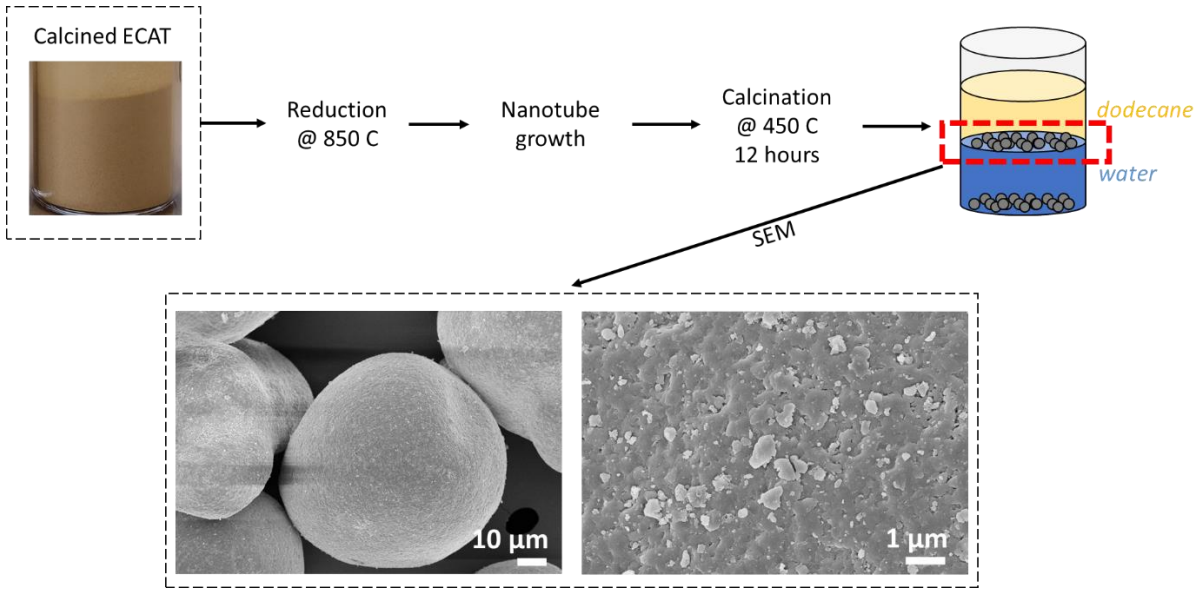

Figure 5.5. ECAT sample procedure for nanotube growth, calcination followed by separation at an oil-water interface. Bottom: SEM images for particles recovered from the oil-water interface, no carbon nanotubes were identified.

The lack of CNT in these samples might be due to the nanotubes detaching from the surface and becoming dispersed in the oil phase. This could happen if the nanotubes had undergone tip growth as opposed to base growth. When base growth takes place, as is the case with nickel on alumina, the nanotubes become anchored to the catalyst surface due to strong metal support interactions. However, the iron present in these catalysts may present weaker interactions with the ECAT surface, hence providing tip growth and a weaker attachment to the surface.

Since the separation by nanotube content had been unsuccessful, CNT-ECAT without any separation was further investigated for polymer decomposition reactions. Figure 5.6 shows SEM

images of the surface of CNT-ECAT, which contains a visual confirmation of the presence of carbon nanotubes. EDS elemental analyses also confirmed the carbon nature of these surface features.

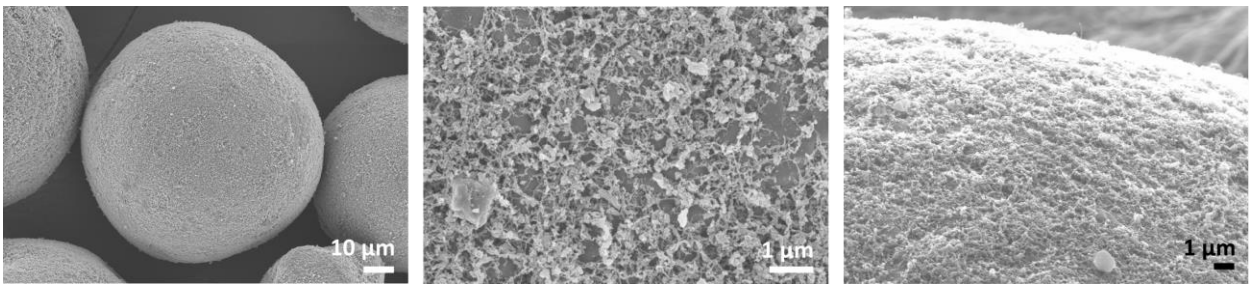

Figure 5.6. SEM images for CNT-ECAT sample. The image on the right was taken with the stub tilted at an angle to improve texture visualization.

FIB milling was used to cut a 10x10 µm cross-section in the CNT-ECAT particle to confirm the presence of CNTs in the pores of the particle (Figure 5.7). Nanotubes were identified within the pore network, and EDS maps confirming the presence of carbon can be found in Figure 5.8. This figure also shows that nanotubes were found up to a depth of 11.82 µm, possibly extending even deeper in the particle. This represents a penetration of at least 47% into the particle radius, which confirms that CNTs can possibly be used as facilitators for non-polar polymers to diffuse into pores of catalysts.

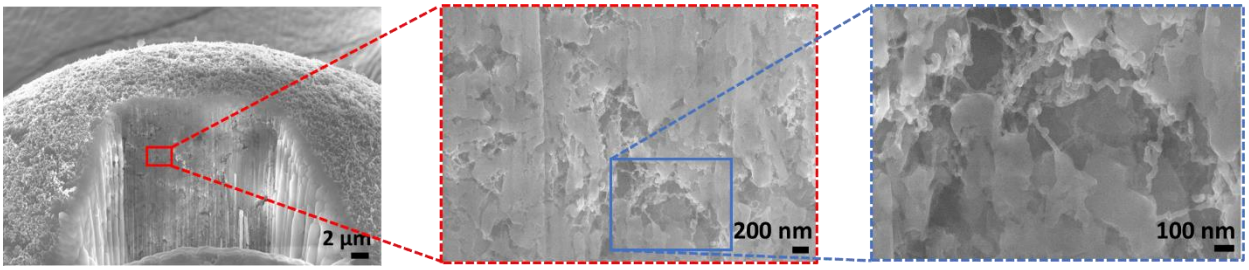

Figure 5.7. Cross-sectional views of CNT-ECAT, showing the presence of nanotubes in the pores of the catalyst. FIB milling was used to finely cut a 10x10 µm section of the sample.

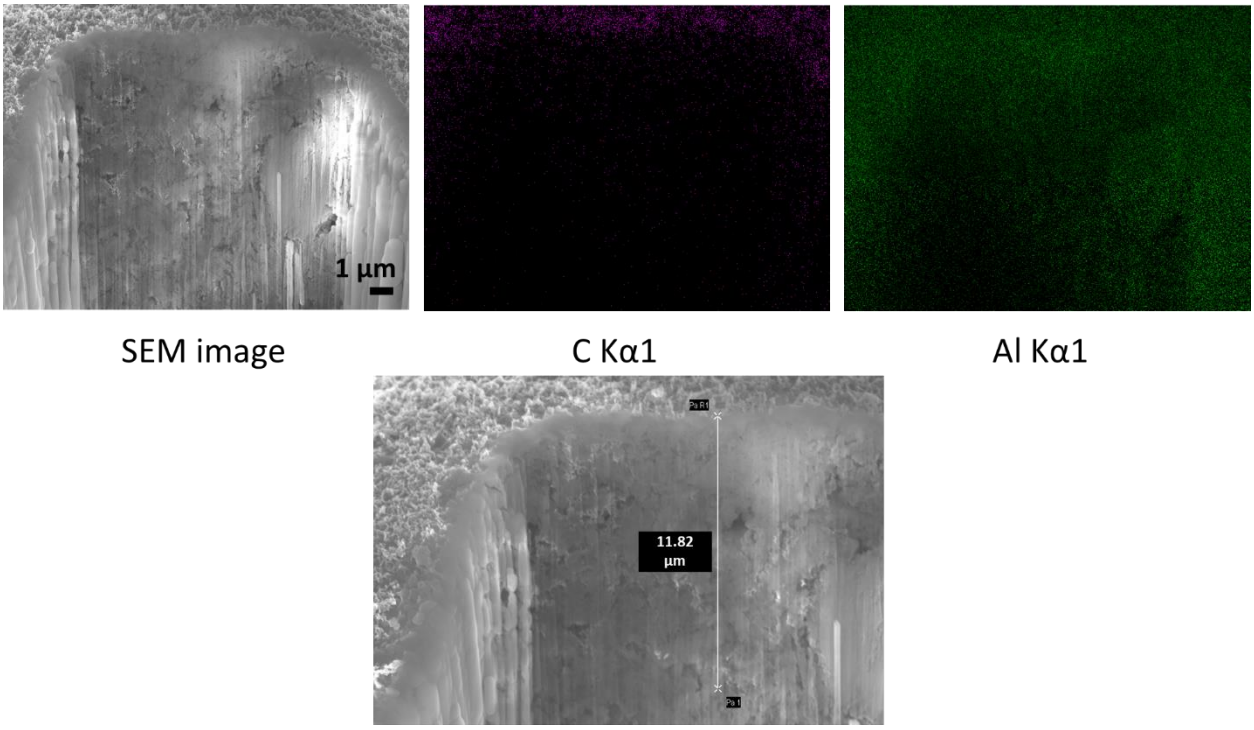

Figure 5.8. Top: SEM image, carbon, and aluminum mapping on CNT-ECAT. Bottom: measured distance from the external surface to the deepest nanotube observed.

ECAT and CNT-ECAT samples were used to convert a polyethylene sample (M_w = 35,000 Da) acquired from Sigma Aldrich. The reaction was carried out at 350 °C (2 °C/min) in a TGA system. Figure 5.9 compares thermal decomposition (black curve), and conversion over 10% ECAT (gray) and 10% CNT-ECAT (blue). It is important to highlight that IPA-TPRx shows that the BAS density remains unchanged after nanotube growth, hence these reactions were run at roughly the same number of acid sites in the system.

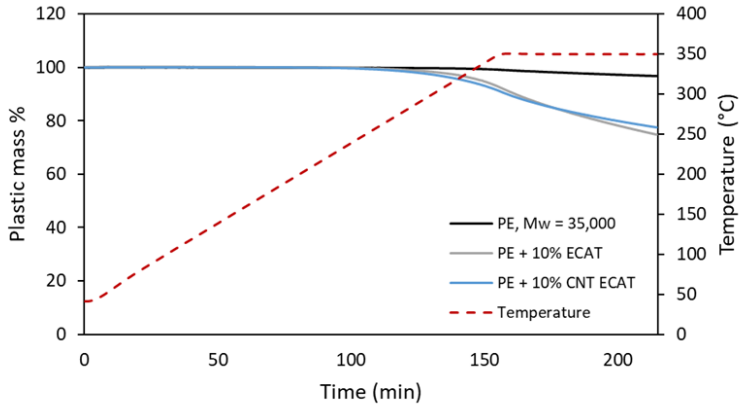

Figure 5.9. Polyethylene (M_w = 35,000) decomposition in the TGA under inert flow, 40 °C to 350 °C at 2 °C/min, 1 hour isothermal at the final temperature.

In the absence of catalysts, there is 3% conversion of PE into vapors after 1 hour at 350 °C, which implies there is a degree of free-radical chemistry taking place, although it should not dominate in the presence of catalysts. In the presence of ECAT or CNT-ECAT, the final conversion is 23% and 20%, respectively. The decomposition curves are highly alike over both catalysts, with the CNTs presence not significantly improving rates of decomposition.

Since wetting effects should be more important when converting high MW polymers, and at higher temperatures (in which diffusion constraints are more pronounced), both ECAT and CNT-ECAT catalysts were used to decompose another polyethylene sample, with M_w = 160,000. The results can be seen in Figure 5.10. CNT-ECAT presents a marginally better performance than ECAT, with temperatures of 50% decomposition at 427.5 °C and 434 °C, respectively, which corresponds to a difference of 1.3 min only. Although these runs show an improvement in the presence of CNTs, the differences are rather small and further experiments are necessary to confirm such trend.

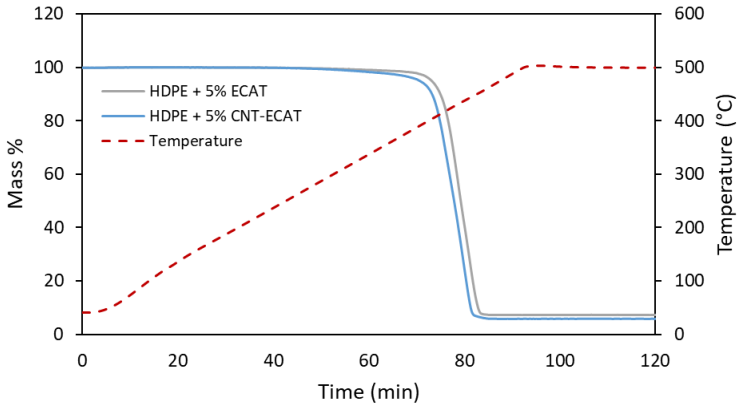

Figure 5.10. Polyethylene (Mw = 160,000) decomposition in the TGA under inert flow, 40 °C to 500 °C at 5 °C/min, 1 hour isothermal at the final temperature.

Possibly, the reason why CNT-ECAT does not present considerable improvements in catalytic performances might be due to the detachment of nanotubes from the catalyst and into the polymer melt. Similarly to what was observed with dodecane in Figure 5.5, the nanotubes will present a high lyophilicity with the polymer melt organic phase during reaction, likely becoming dispersed in it and acting as an inert species in the system.

The CNTs growth approach in ECATs may still be valuable and yield promising results in different ECAT samples. If, for example, nanotubes were grown onto an ECAT sample that had been in contact with a nickel-containing feedstock, then they would likely grow with the metal particle still attached to the catalyst particle (base growth), and thus they would not easily disperse in other phases. In this case, it is likely that the nanotubes would considerably improve wetting of polymer on the catalyst surface. Further investigation is needed to validate this hypothesis.

5.2. Reactive distillation

Often, the goal of polyolefin decomposition reactions is to produce ethylene and propylene, for these are the monomers used to manufacture polyethylene and polypropylene, respectively.

One possible strategy to narrow down the product distribution of catalytic depolymerization into light olefins is to use a reactive distillation system.[114] Here, we explore different combinations of acid catalysts in a reactive distillation system to achieve this goal.

The system consisted of a fritted 1 in. ID quartz reactor tube (in which the 1 g of polyethylene and catalysts were inserted) and a distillation column above the reactor, filled with glass beads for improved heat transport. The insulated outlet tube led to an ice-cooled bubbler filled with a solvent (usually decalin) that should retain heavier liquid products, whereas the gas products flew to the vent. The liquid in the cold trap was analyzed via GC-FID/MS after the end of each experiment, and the gas was collected in gas bags every few minutes while the reaction was taking place. These bags were then analyzed in an offline GC-MS. This semi-batch system is depicted in Figure 5.11.

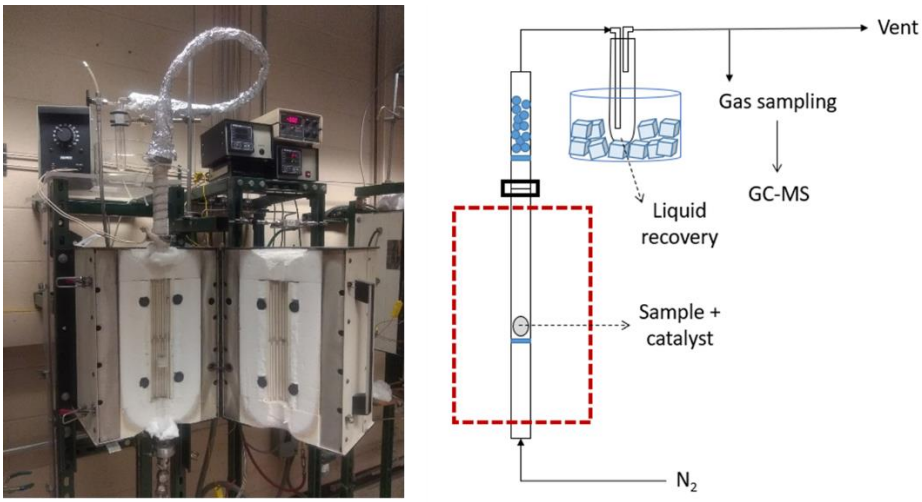

Figure 5.11. Reactive distillation unit.

Catalytic polyethylene depolymerization reactions over ZSM-5, ASA, and a combination of beds (ASA mixed with polymer powder + ZSM-5 bed downstream) were performed under 200

ml/min N_2 flow. Figure 5.12 displays the results for catalytic pyrolysis runs over 2.3% ASA, and 5% ASA (mixed with the plastic) + 5% ZSM-5 (downstream, separated by a layer of quartz wool).

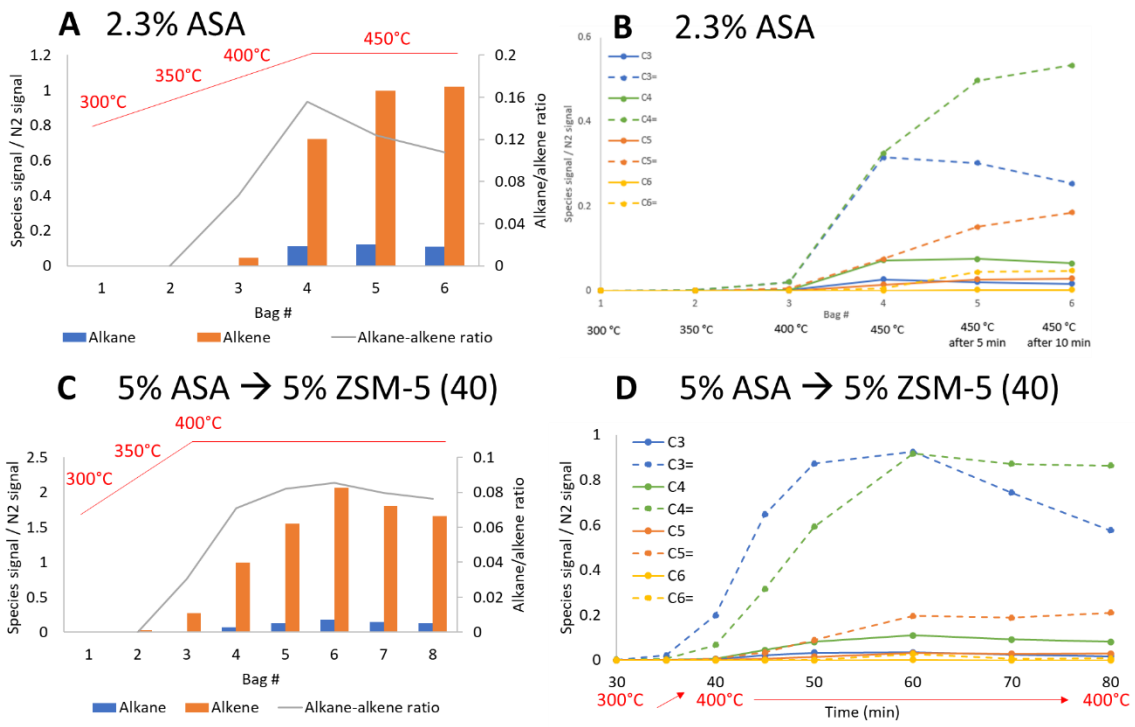

Figure 5.12. Alkane and alkene gas production in the reactive distillation system, per gas bag collected, for runs with (A) 2.3% ASA and (C) 5% ASA + 5% ZSM-5 downstream. Gas evolution distinguished by species for (B) 2.3% ASA and (D) 5% ASA + 5% ZSM-5 downstream. Sample gas bags were collected every 5 minutes.

The system, as expected, favors the production of light gases (C_3, C_4). However, polyethylene converted over 2.3% amorphous silica alumina (Figure 5.12 A and B) also yielded 18% of liquid products, comprising a very complex mixture that spanned from light products such as C_5 up to C_{30}^+.

To further convert these heavy products, the temperature of the distillation column was lowered from 125 °C to room temperature – this change aimed to ease the condensation of heavier products in the distillation column, so that they would flow back into the reactor and be undergo

more cracking reactions. Also, to increase the extent of cracking reactions, a second bed of ZSM-5 was added downstream to the polyethylene + ASA mixture (see Figure 5.12 C and D). After such changes were implemented, the liquid production decreased to less than 1% of the initial mass of polymer in the system, and products consisted mainly of $C_3^=$ and $C_4^=$. These experiments highlight the potential of reactive distillation systems to produce light olefins with high yields starting from well-sorted polyolefins.

5.3. Conclusions

In this chapter, three strategies to improve polymer recycling reactions were presented and discussed. Carbon nanotube growth over ECAT is a promising approach to improve polymer-catalyst contact, although further studies with CNT base growth are still needed to validate its potential. Reactive distillation strategies were shown to produce high yields of C_3 and C_4 olefins, which can then be used in the chemical manufacturing industry.

Chapter 6: Effect of film thickness on polystyrene decomposition

6.1. Introduction

Polystyrene (PS) pyrolysis results in a simple product distribution when compared to polyolefins.[47] Its major products are styrene monomer, dimer and trimer. Minor byproducts include α-methylstyrene, ethylbenzene, and toluene. However, industrial thermal depolymerization processes usually recover styrene monomer in yields of 40-70%.[115]

The styrene monomer is primarily formed by chain unzipping, i.e., end-chain β-scission. It has traditionally been thought that the mechanism by which dimers and trimers form is via backbiting, i.e., intramolecular shift of the radical position and mid-chain β-scission. Nonetheless, recent studies have shown that dimers can also be formed by benzyl radical addition. At higher temperatures, benzyl addition is the most competitive mechanism for dimer formation due to higher concentrations of the benzyl radical.[47]

We hypothesize that, especially at higher temperatures, the yields of byproducts can be controlled by the sample thickness. The thinner the sample, the shorter the diffusion path of a product to reach the gas phase, therefore fewer sequential reactions should take place and the yields of byproducts should be lower. In this work, we monitor the yields of polystyrene decomposition byproducts when varying sample thickness.

6.2. Experimental

Polystyrene sample (M_w = 260,000) was acquired in the form of ~5 mm *spheres* from Scientific Polymer Products, inc. A fraction of this sample was further *ground* into powder form, with grains at about 0.5 mm diameter. In addition, another fraction of this sample was dissolved

in toluene and further spin coated onto glass slides. As the solvent dried, a thin layer of polystyrene was deposited onto the slide. The resulting *thin film* was then scraped out of the glass and used as a sample.

Thermal decomposition reactions were performed in a NETZSCH STA 449 F1 Jupiter TGA coupled to a QMS 403 C Aeolos mass spectrometer. Reactions were carried out using four polystyrene sample loadings (20-100 mg) in the sphere form, under 40 ml/min argon flow, in three ramp rates: 1, 5 and 10 °C/min up to 650 °C.

Reactions were also carried out in a 5250T CDS Pyroprobe microyrolyzer system connected to a Shimadzu QP2010 GCMS/FID system, equipped with a 60-m RESTEK Rtx-1701 column. About 1 mg of ground and thin film polystyrene were loaded into each pyrolysis quartz tube. The pyrolysis program consisted of 1 minute at 500 °C, during which all evolved gases were injected into the GC. After each pyrolysis run, the tube was automatically ejected into a vial with flowing nitrogen, to ensure no reactions with atmospheric oxygen would occur as the tube was cooling down. Tubes were weighted before and after reaction to calculate conversion to vapors.

6.3. Results and Discussion

TGA decomposition curves for polystyrene (Figure 6.1) consist of one single step and are independent of the sample loading. The temperature of maximum degradation, in which the derivative is at its highest, was 395 °C for the ramp rate of 5 °C/min. Conversion levels were near 100% for all loadings, with residual char representing less than 0.2 wt% in all cases.

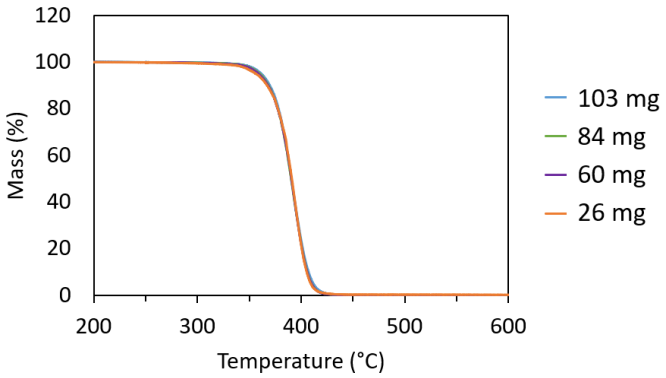

Figure 6.1. TGA degradation profiles for different polystyrene loadings, ramp rate = 5 °C/min.

Evolved products from these TGA runs were analyzed in an online mass spectrometer. Identified byproducts included toluene, ethylbenzene, benzene, cumene, α-methylstyrene and dimers such as 2,4-diphenylbutene and 1,3-diphenylbutene. The MS signals for byproducts fingerprints were integrated and compared to the total area of the styrene fingerprint, m/z = 104. The results can be found in Figure 6.2.

It is noticeable that the dimers/styrene ratio increases linearly as sample loading increases. In these TGA experiments, the crucible cross-sectional area was held constant. Thus, increases in sample loading reflect an increase in sample thickness (height). With that, any products formed would have a longer path toward the polymer melt/argon interface at higher sample loadings. Similar although not so pronounced trends are observed in the yields of α-methylstyrene, and toluene + ethylbenzene. On the other hand, benzene yields seem to be independent of sample thickness.

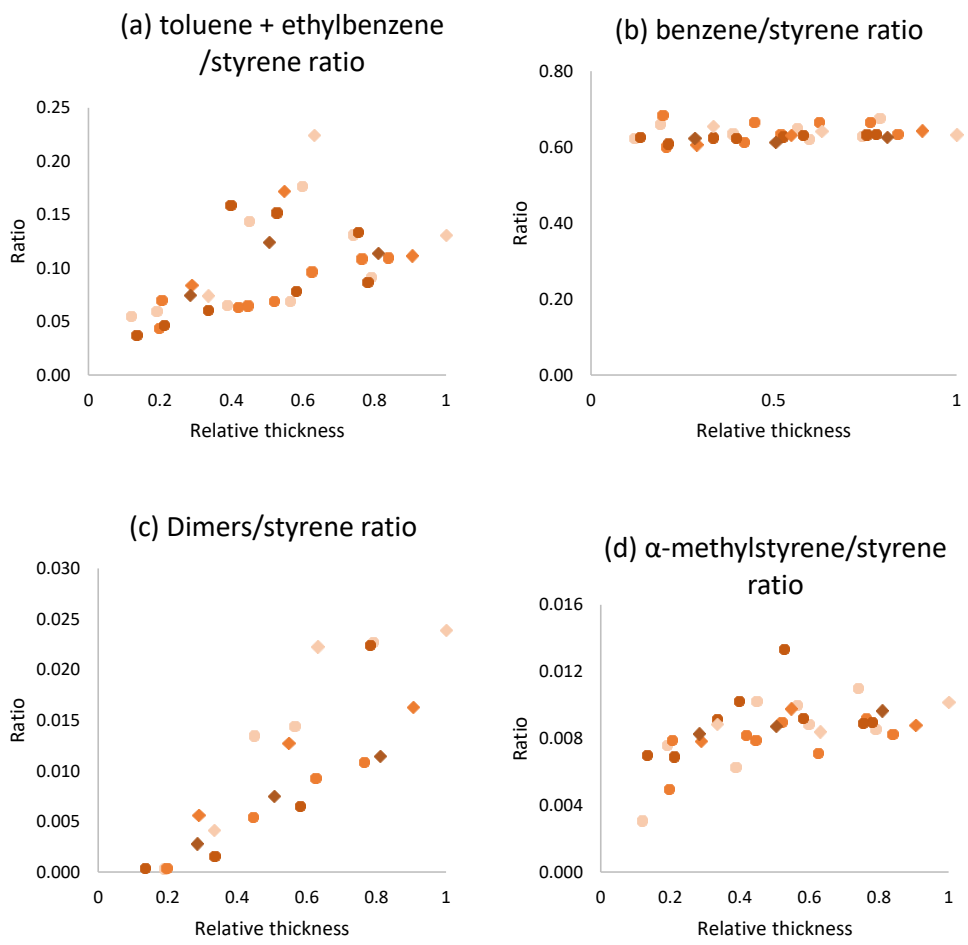

Figure 6.2. m/z signal ratios of different byproducts to the base peak of styrene, as a function of sample thickness, obtained by TGA-MS. Markers: Dark-colored = 10 K/min; Medium-colored = 5 K/min; Light-colored = 1 K/min; Spheres = bead sample; Rhombi = powder sample. (a) m/z = 91/104; (b) m/z = 78/104; (c) m/z = (165+178+193+208)/104, highest peaks for dimers 2,4-diphenylbutene and 1,3-diphenylbutene; (d) m/z = 118/104.

Results from decomposition in the pyrolyzer system are shown in Figure 6.3. Product yields of styrene, dimer and trimer were quantified by an FID detector. After 1 minute at the reaction temperature of 500 °C, the conversion to vapors of the ground PS sample averaged 83%, whereas the thin film samples were 97% converted. Comparing product distributions, the use of thin film as opposed to the ground sample reduced the selectivity to dimers by 5%, while gaining

in styrene yields. Trimer selectivity, on the other hand, did not suffer an appreciable change. This might suggest that the main mechanism of trimer formation under these conditions is via backbiting, which should not change by varying film thickness.

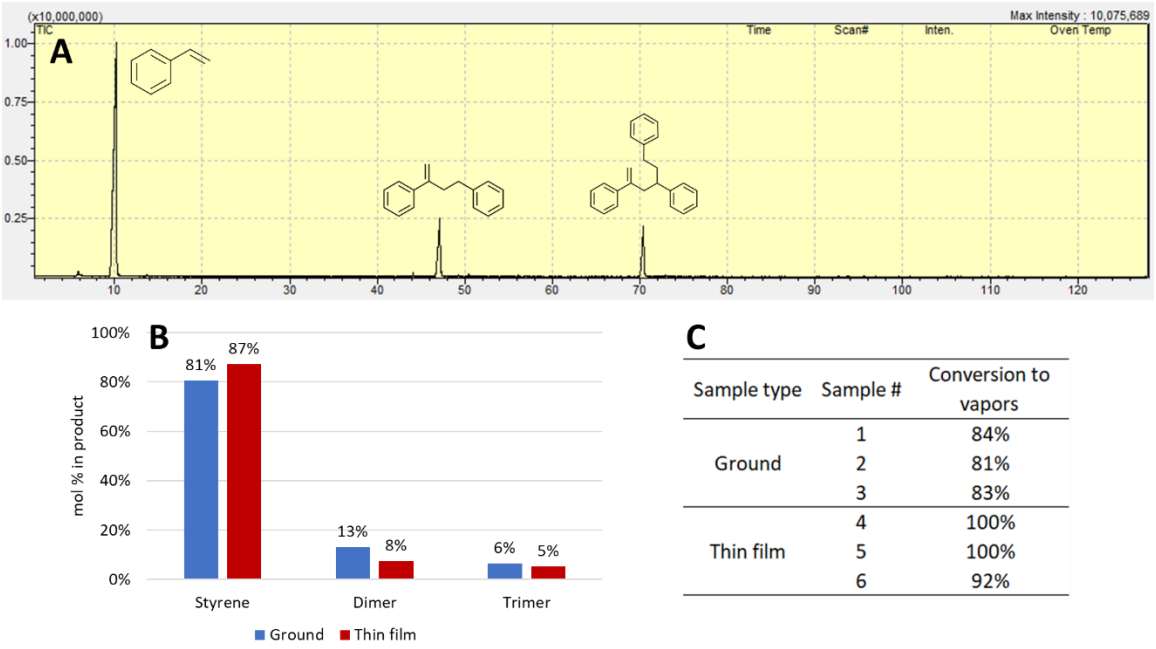

Sample type	Sample #	Conversion to vapors
Ground	1	84%
	2	81%
	3	83%
Thin film	4	100%
	5	100%
	6	92%

Figure 6.3. (A) Typical chromatogram for polystyrene pyrolysis. The major peaks consist of styrene, and its dimer and trimer. (B) Product distribution from polystyrene pyrolysis, ground and thin film samples. (C) Conversion to vapors for ground and thin film polystyrenes, obtained by weighing the pyrolysis tube before and after pyrolysis.

6.4. Conclusions

This work shows that the selectivity towards styrene dimers can be controlled by tuning the sample thickness of polystyrene. The longer the diffusion path for products, more likely they will be to undergo sequential reactions, and higher the selectivity towards dimers will be. Trimers do not seem to follow the same trend, being likely generated by backbiting reactions, which are not dependent on the film thickness. The yield of other byproducts such as α-methylstyrene and toluene + ethylbenzene also seem to present a dependency with film thickness.

Chapter 7: Conclusions and future work

In this work, various aspects of thermal and catalytic polymer decomposition were explored. The insights gained from this research shed light on some previously unexplored questions, such as the effect of the presence of polymer additives during depolymerization reactions or the role of internal vs. external zeolite sites for such reactions.

We have shown that additives, even in high concentrations, do not affect the rates of polyethylene pyrolysis. On the other hand, they play a critical role when the reaction is taking place over the surface of a heterogeneous catalyst. Additives also deposit on zeolites during depolymerization, and their original BAS may or may not be recoverable by calcination. The additives which permanently deposit onto these surfaces are able to modify sites and influence the activity of the modified catalyst. Furthermore, we have shown that zinc from polymer additives can improve alkane cracking capabilities of zeolites in a wide range of pore size, whereas this effect is not observed on mesoporous acid catalysts. On top of that, it was demonstrated that zinc sites are metastable, and their structure and activity change over storage time.

Comparison between HDPE and LLDPE has demonstrated the important role that short chain branches play during reactions over acid catalysts. Tertiary carbons were shown to considerably improve reactivity of the polyethylene sample, although they hinder internal diffusion into micropores. HDPE was found to be able to diffuse into zeolite pores more easily, which resulted in a slightly lighter product distribution than LLDPE. Additionally, it was evidenced that ppm-levels unsaturation in polyethylene samples are not the controlling factor for perceived rates of decomposition.

New approaches to improve polyethylene reactivity and selectivity were explored, including strategies to improve polymer-catalyst contact, and a reactive distillation system to narrow product distribution. Finally, it was shown that the sample thickness plays an important role in the polystyrene pyrolysis selectivity towards dimers and other byproducts.

In conclusion, this work has explored thermal and catalytic conversion of polymers, offering insights on factors that influence reactivity, selectivity, and catalyst behavior. This dissertation contributes to the growing body of knowledge currently being developed on chemical recycling reactions, which aim to tackle the challenge of properly addressing plastic waste and augment circularity of such materials.

Appendix: Ambient temperature moisture effects on phosphorus-modified acid catalysts

A.1. Introduction

The fluid catalytic cracking (FCC) process is widely used to convert heavy hydrocarbons into lighter, more valuable products such as gasoline.[116] Applications of these catalysts for upgrading of biomass based renewable feedstocks[117, 118] and waste plastics[119-121] has also emerged recently. FCC catalysts are primarily comprised of zeolites, amorphous silica alumina and inactive clay. Furthermore, additives can be incorporated into an FCC catalyst to improve its performance[113], such as ZSM-5, used to increase propylene yields and enhance octane numbers[122], and phosphorus, which has been shown to improve hydrothermal stability of such catalysts.[60, 123]

When phosphorus is introduced into zeolites as a post-synthesis modification, it is known to reduce the number of strong acid sites[94, 124], although the exact mechanism of phosphorus-zeolite interaction is still under discussion. Several forms of P-framework interaction have been proposed in the literature. Some propose that this interaction occurs via a covalent bond between the phosphorus (or phosphorus group) and the zeolite framework, sometimes cleaving bonds originally existent in the framework.[124-126] This leads to a partial hydrolysis of the structure, but still the stability of the overall zeolite structure is improved.[57] It has also been proposed that Brønsted acid sites (BAS) can protonate phosphoric acid[60], which would create a more reversible kind of interaction. Further complicating matters, P may get incorporated within zeolites in many forms, interacting in numerous ways with framework atoms as described above, but also interacting with extra lattice Al species, and P may also cluster to form polyphosphates. The nature

of protic species created in P containing zeolites has been shown to shift depending on the relative moisture content present, creating a wide array of prospective active sites.[127, 128]

Phosphorus as a zeolite additive has been extensively explored.[57, 60, 123, 124] However, there is a gap in the literature when it comes to the influence of residual moisture upon storage prior to introduction to the FCC unit. Could ambient moisture play a role in modifying catalyst nature and performance? This work is dedicated to assessing the effects of ambient moisture on P-modified acid catalysts, especially ZSM-5.

A.2. Experimental

ZSM-5 (Si/Al = 11.5) samples were acquired from Zeolyst International in the ammonium form. To render them acidic, the zeolites were calcined for 6 hours at 550 °C under 100 ml/min air flow. The ramp rate used to achieve the calcination temperature was 2 °C/min in order to preserve the zeolite structure. The resulting sample is H-ZSM-5. The sample described as “FCC catalyst” is a fluidized catalytic cracking catalyst provided by Phillips 66. Phosphorus is present in its composition.

Incipient wetness impregnation (IWI) with H_3PO_4 was used to produce the P-modified zeolites. The starting material was H-ZSM-5, and the number in the nomenclature of P-modified samples represents the P/Al ratio used in the IWI process (e.g., 0.4 P-ZSM-5 was prepared using a H_3PO_4 concentration so that the P/Al ratio in the sample was 0.4). After impregnation, the sample was dried at 80 °C under vacuum for 10 hours, and subsequently calcined at 500 °C (ramp rate = 2 °C/min) for 1 hour under 100 ml/min air flow. Finally, catalyst samples were pelletized, crushed and sieved between 90 and 250 microns.

The steaming process was carried out in a horizontal reactor, equipped with an upstream water bubbler. Samples were steamed at 700 °C for 2 hours under nitrogen flow with a relative humidity of 70%. Samples were then dried under nitrogen flow at 250 °C for 6 hours. Catalyst samples that underwent this process are represented by “st” in the sample name.

Steamed samples were then hydrated at room temperature to emulate the effect of ambient air moisture in the storage of acid catalysts. Hydration was conducted by placing catalysts and cups filled with water in a closed box. A hygrometer placed inside the box showed 99% relative humidity (RH) after equilibration. Catalysts were allowed to hydrate under 99% RH for 24 hours inside the box. Samples that underwent this process are denoted by “hyd” in their name. After hydration, a final calcination step was performed at 600 °C for 5 hours (ramp rate = 15 °C/min) under air flow, which is either explicitly denoted in the text or represented with “fast” in sample name.

Thermogravimetric analysis (TGA) was performed in a NETZSCH STA Jupiter 449 F1 system, under 40 ml/min argon flow. The temperature program started with a 10-min isothermal equilibration step at 40 °C to stabilize the initial mass, then the temperature was increased to 500 °C at a rate of 10 °C/min. 20 mg of catalyst were loaded in each run.

Isopropylamine temperature programmed reaction (IPA-TPRx) was performed as described in Section 2.2.3.1. Fourier-Transform Infrared Scpectroscopy (FTIR) spectra were acquired in a PerkinElmer Spectrum 100 system equipped with a high-temperaure diffuse reflection (DRIFTS) chamber. Background measurements were obtained using KBr powder. Catalysts were pretreated in situ under helium flow at 300 °C prior to spectrum acquisition.

To probe alkane cracking capabilities, nC_7 cracking was performed over the different catalyst samples prepared. Reactions were carried out in a 0.25 in. OD quartz tube in a pulse reactor. The reaction temperature was 480 °C, n-heptane pulse size was 6 μmol, and the carrier gas (helium) flow rate was 80 mL/min. Catalysts were diluted with inert glass beads, and the catalyst loadings for each experiment are explicit in the corresponding figure captions. Effluent gases were analyzed in a HP 5890 Series II gas chromatograph equipped with an HP-PLOT column and a flame ionization detector.

A.3. Results and Discussion

In order to systematically study these catalysts, phosphorus-modified samples were prepared via incipient wetness impregnation. In the sample nomenclature, the number preceding the "P" is the P/Al ratio. The synthesized catalyst samples were steamed at 700 °C and dried in N_2 (this process is denoted by "st" in the sample name). After steaming, the samples were exposed to ambient temperature moisture (denoted by "hyd" in the sample name) and finally calcined in air ("calc"). This process was designed to simulate a steamed FCC catalyst sample being stored under ambient conditions and then being calcined prior to use in the FCC unit.

Various ZSM-5 (Si/Al = 11.5) samples were exposed to ambient moisture for 24 hours, then dehydrated in a thermogravimetric analysis (TGA) system under inert gas flow. (Figure A.0.1) Three regions of weight loss can be observed: i) the initial equilibration phase, which consists of 10 min at 40 °C; ii) the 10 °C/min heating ramp rate, between 40 °C and 250 °C (loosely bound water); and iii) temperatures above 250 °C (chemisorbed water). The total weight loss for the untreated ZSM-5, ZSM-5-st-hyd and 1P-ZSM-5-st-hyd were, respectively, 7.8%, 9.5% and 11.3%.

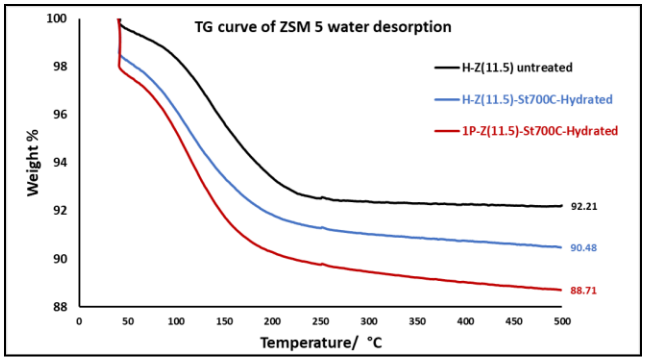

Figure A.0.1. TGA curves under inert environment for untreated and hydrated catalyst samples; ramp rate = 10 °C/min, final temperature = 500 °C.

Phosphorous-containing zeolite retained 19% more water than a regular zeolite that underwent the same processes – indicating that phosphorus groups formed on the surface of the zeolite are hydrophilic as expected. It is also noteworthy that the 1P-ZSM-5-st-hyd sample retained more strongly bound water at T range > 250 °C.

Figure A.0.2 displays Brønsted acid densities measured by isopropylamine temperature programmed reaction (IPA-TPRx) for different ZSM-5 (Si/Al = 11.5) samples. It can be noticed that in fresh samples the BAS density decreases with increasing phosphorus loading. This trend has been reported in the literature[57] and is also supported by infrared spectroscopy data (see Figure A.0.3). Steaming the zeolites at 700 °C considerably lowers the total acidity for all samples, ranging from 74% to 78% site loss. If, after steaming, the zeolites are exposed to room temperature moisture for 24 hours and then calcined in air at 600 °C, an untreated sample displays a further loss of 29% of its acid sites. However, P-ZSM-5 (0.15 P and 0.4 P) both regained acid sites after exposure to moisture and subsequent calcination. This interesting effect was more prominent with an increased amount of exchanged phosphorus – 0.15 P shows an increase of 26% in Brønsted acidity, whereas 0.4 P shows an increase of 41%.

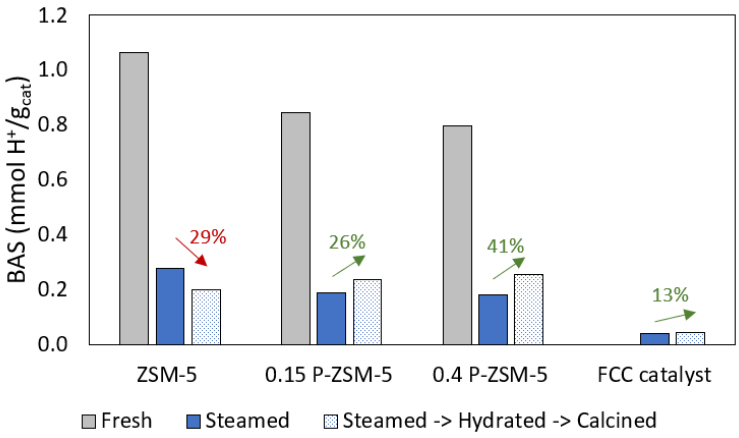

Figure A.0.2. Brønsted acid site densities calculated by IPA-TPRx for different catalyst samples.

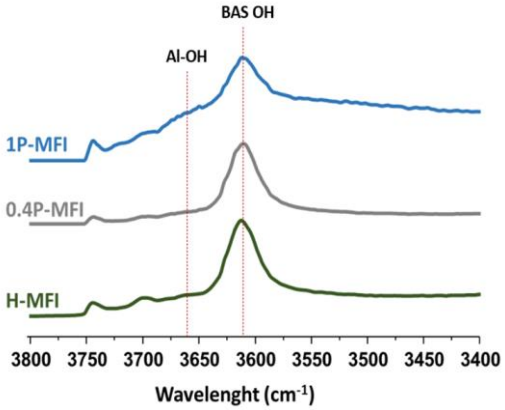

Figure A.0.3. BAS density decreases with increasing P-loading due to P-O-Al bonds formation as apparent from both IPA-TPRx (Figure A.0.2) and OH band intensity around 3600 cm^{-1}.

This is an intriguing result, as catalysts are often pre-steamed prior to storage and eventual use in FCC reactors. The re-hydration that causes activity differences upon simple storage and thermal heating (as would occur in an FCC regenerator upon catalyst introduction), may play an important role that is often overlooked when analyzing the ultimate catalyst activity.

This result denotes that the effects of phosphorus to directly protect the catalyst upon steaming are less pronounced than the residual site recovery. All samples presented 74-78% BAS

reduction after steaming, but incorporation of additional P loadings does generate significant enhancements in the capability of recovering Brønsted acidity after exposure to room temperature moisture and subsequent calcination. The same trend was observed for a commercial FCC catalyst that contained phosphorus (Figure A.0.2), indicating that these effects occur in industrial samples as well as those synthesized here.

Cracking of n-heptane in a micropulse reactor, in a system described in prior reports[67, 129], was used as a probe reaction to compare the activity and selectivity of these ZSM-5 samples. When using the same amount of catalyst, 0.4P-ZSM-5-st-hyd-calc yielded 2.4x times more conversion than 0.4P-ZSM-5-st, suggesting that not only did the hydration process increase the number of BAS (1.4x more) but it also enhanced the cracking capabilities of the BAS present in the sample.

Comparing n-heptane conversions per proton (Figure A.0.4), as quantified via IPA TPRx, it can be seen that the presence of phosphorus protects the activity of Brønsted acid sites for alkane cracking after samples undergo steaming. Conversion/H^+ for fresh ZSM-5 was 0.192%, and decreased to 0.075% after steaming. When exchanging a small amount of P (0.15 P), the activity per proton remains the same as fresh ZSM-5 (0.193%), which demonstrates that phosphorus protects the activity of acid sites. 0.4 P-ZSM-5 also displays maintained activity after steaming, which supports this claim.

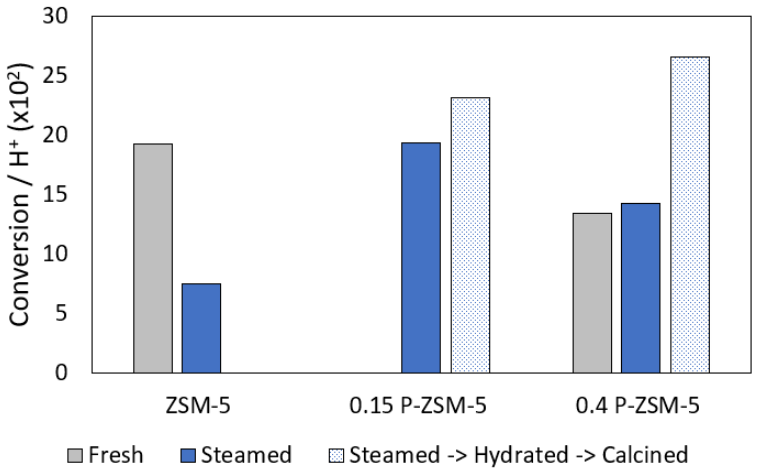

Figure A.0.4. Cracking conversion of n-heptane, in a micropulse reactor, normalized by the number of Brønsted acid sites as calculated by IPA-TPRx, with different catalyst samples.

Interestingly, if the P-modified steamed samples are subsequently submitted to ambient temperature moisture and calcination, the rates per proton increase substantially – 20% for 0.15 P-ZSM-5, and 87% for 0.4 P-ZSM-5. This effect is more prominent with higher loadings of phosphorus, as illustrated in Figure A.0.4.

Figure A.0.5 displays possible interactions between phosphorus species and the zeolite framework. After ion exchange with phosphoric acid, a cationic phosphorus species is formed during calcination.[60] Then, moisture exposure at ambient temperature increases the number of BAS – which indicates that water promotes phosphorous mobilization into polyphosphates, restoring original acidity. It is worth mentioning that this BAS recovery is independent of the temperature heating rate of the last calcination step. Varying the calcination ramp from 1°C/min to 15°C/min reveals identical results. We propose that this process of ambient moisture exposure followed by calcination increases cracking activity per BAS by restoring original acid sites, which consists of stronger acids than P-OH groups. Also, site proximity and high concentrations of paired

sites in low Si/Al samples allow for interaction of the polyphosphate species with nearby BASs, which we hypothesize may further enhance their activity.

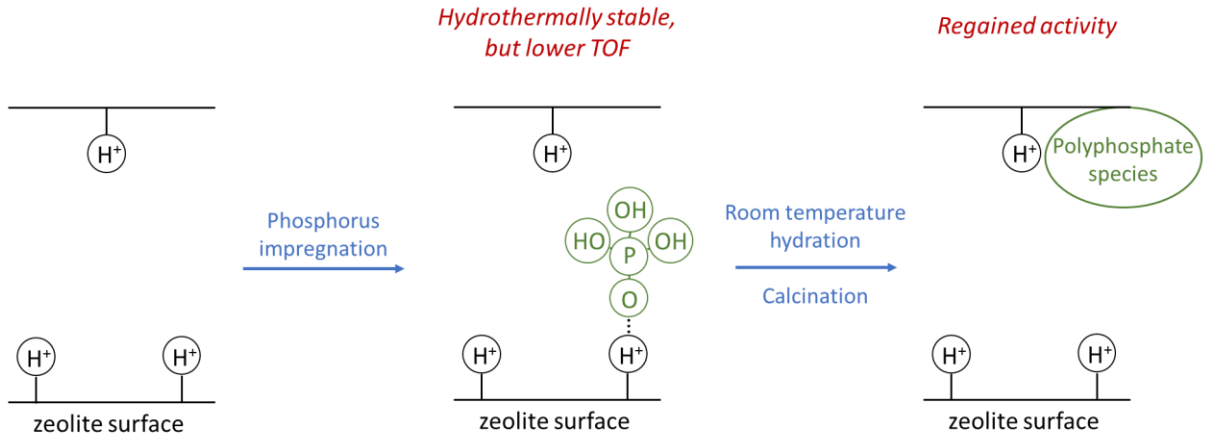

Figure A.0.5. Proposed phosphorus species interactions with zeolites.

Conversion and selectivity for n-heptane cracking over ZSM-5 samples are shown in Figure A.0.6. Comparing samples that were not subject to hydrothermal treatment (Figure A.0.6A), it can be noticed that the product distribution remains very similar between 0.4P-ZSM-5 and the parent zeolite, even though the activity per BAS is decreased for the phosphorus-containing sample. However, when comparing steamed samples (Figure A.0.6B), it can be noted that addition of 0.15P significantly increases the C_4 alkenes / C_4 alkanes ratio ($C_4^=/C_4$), which is often reported as a fingerprint for hydride transfer when compared at constant conversion, with lower ratios indicating more selectivity toward hydride transfer reactions. Hence, addition of small amounts of phosphorus suppresses the apparent hydride transfer selectivity. We note that this could also be a consequence of diminished sequential reactions of produced olefins along the diffusion path of the zeolite with less active P species. With a higher P loading (0.4 P ZSM-5), the $C_4^=/C_4$ ratio is still

higher than that on the parent zeolite, but less pronounced when compared with the sample of lower P loading.

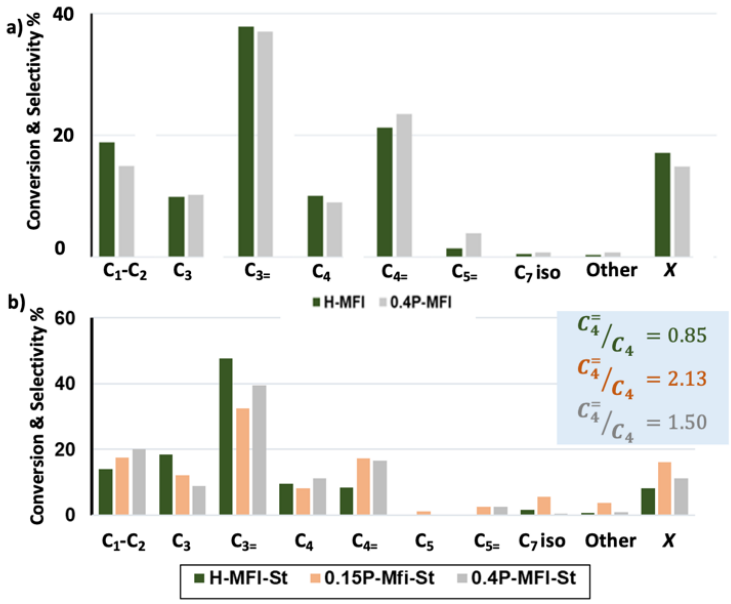

Figure A.0.6. (A) Conversions and selectivity for H-ZSM-5 (8.4 mg catalyst loading) and 0.4 P-ZSM-5 (14.5 mg) at 480 °C. (B) Conversions and selectivity for steamed samples: H-ZSM-5-St (42.5 mg catalyst loading), 0.15 P-ZSM-5-St (44.3 mg), and 0.4 P-ZSM-5-St (43.9 mg). Box indicates hydride transfer coefficient, defined as: i_{HT} = $C4^{=}$/C4.

Figure A.0.7 compares phosphorus-modified samples that were steamed and subsequently subject to ambient temperature moisture (as is the case with FCC catalyst sample storage) followed by a final calcination step. Rate per BAS significantly increases after hydration and calcination, along with no significant changes in selectivity. Similar results are observed at high and low P loadings.

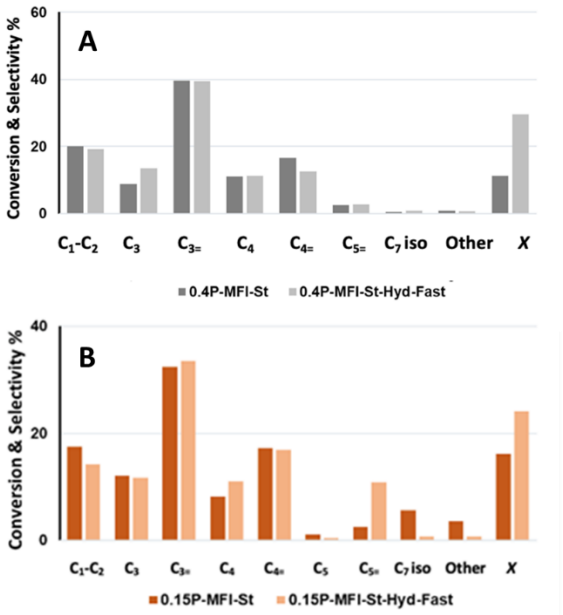

Figure A.0.7. Conversions and selectivity for n-heptane cracking over (A) 0.4 P-ZSM-5-st and 0.4 P-ZSM-5-st-hydr-calc, and (B) 0.15 P-ZSM-5-st and 0.15 P-ZSM-5-st-hydr-calc.

nte that the enhancement in rate alongside minimal changes in cracking selectivity for n-heptane cracking mimics results obtained for n-hexane cracking in the presence of varying amounts of "synergistic sites", or framework Brønsted sites with extra lattice Al species in the vicinity which modify the local confining environment. A similar phenomenon may be present here. It is known that modifying the local environment surrounding an active site by adding species that either modify the confining environment or partially polarizes adsorbed molecules and transition state can significantly modify reaction rates. The increase in strong BAS density reported in Figure A.0.2 upon hydration followed by calcination implies that some P species appear to migrate away from surface Brønsted acid sites. This releases stronger acid sites, such as synergistic sites, which would otherwise be more susceptible to hydrothermal attack. In other words, P appears to protect the most active framework species, and room temperature exposure to ambient humidity appears to aggregate these P species, revealing the most active framework Brønsted acid sites.

An additional role may be played by P species nearby active sites. They can modify the local confining environment in a similar way as Al species are able to, enhancing the catalytic activity. This is an interesting topic that should be further explored. The findings in this work elucidate the P-ZSM-5 interactions with water under ambient conditions and show that the storage conditions of P-modified FCC catalysts may play a significant role in their final activity.

References

[1] R. Geyer, A Brief History of Plastics, in: M. Streit-Bianchi, M. Cimadevila, W. Trettnak (Eds.) Mare Plasticum - The Plastic Sea: Combatting Plastic Pollution Through Science and Art, Springer International Publishing, Cham, 2020, pp. 31-47.
[2] D.M. Mitrano, M. Wagner, A sustainable future for plastics considering material safety and preserved value, Nature Reviews Materials, 7 (2022) 71-73.
[3] R. Geyer, J.R. Jambeck, K.L. Law, Production, use, and fate of all plastics ever made, Science Advances, 3 (2017) e1700782.
[4] L. Lebreton, A. Andrady, Future scenarios of global plastic waste generation and disposal, Palgrave Communications, 5 (2019) 6.
[5] H. Millet, P. Vangheluwe, C. Block, A. Sevenster, L. Garcia, R. Antonopoulos, The nature of plastics and their societal usage, Plastics and the Environment, 2018 (2018) 1-20.
[6] D.K. Barnes, F. Galgani, R.C. Thompson, M. Barlaz, Accumulation and fragmentation of plastic debris in global environments, Philosophical transactions of the royal society B: biological sciences, 364 (2009) 1985-1998.
[7] S.C. Gall, R.C. Thompson, The impact of debris on marine life, Marine Pollution Bulletin, 92 (2015) 170-179.
[8] S. Franzellitti, L. Canesi, M. Auguste, R.H.G.R. Wathsala, E. Fabbri, Microplastic exposure and effects in aquatic organisms: A physiological perspective, Environmental Toxicology and Pharmacology, 68 (2019) 37-51.
[9] S.L. Wright, D. Rowe, R.C. Thompson, T.S. Galloway, Microplastic ingestion decreases energy reserves in marine worms, Current Biology, 23 (2013) R1031-R1033.
[10] Y. Wang, J. Huang, F. Zhu, S. Zhou, Airborne Microplastics: A Review on the Occurrence, Migration and Risks to Humans, Bulletin of Environmental Contamination and Toxicology, 107 (2021) 657-664.
[11] R. Geyer, Production, use, and fate of synthetic polymers, Plastic waste and recycling, Elsevier2020, pp. 13-32.
[12] P. Oblak, J. Gonzalez-Gutierrez, B. Zupančič, A. Aulova, I. Emri, Processability and mechanical properties of extensively recycled high density polyethylene, Polymer Degradation and Stability, 114 (2015) 133-145.
[13] Z.O. Schyns, M.P. Shaver, Mechanical recycling of packaging plastics: A review, Macromolecular rapid communications, 42 (2021) 2000415.
[14] S. Liu, P.A. Kots, B.C. Vance, A. Danielson, D.G. Vlachos, Plastic waste to fuels by hydrocracking at mild conditions, Science Advances, 7 (2021) eabf8283.
[15] G. Celik, R.M. Kennedy, R.A. Hackler, M. Ferrandon, A. Tennakoon, S. Patnaik, A.M. LaPointe, S.C. Ammal, A. Heyden, F.A. Perras, M. Pruski, S.L. Scott, K.R. Poeppelmeier, A.D. Sadow, M. Delferro, Upcycling Single-Use Polyethylene into High-Quality Liquid Products, ACS Central Science, 5 (2019) 1795-1803.
[16] F. Zhang, M. Zeng, R.D. Yappert, J. Sun, Y.-H. Lee, A.M. LaPointe, B. Peters, M.M. Abu-Omar, S.L. Scott, Polyethylene upcycling to long-chain alkylaromatics by tandem hydrogenolysis/aromatization, Science, 370 (2020) 437-441.

[17] M.N. Dunkle, P. Pijcke, W.L. Winniford, M. Ruitenbeek, G. Bellos, Method development and evaluation of pyrolysis oils from mixed waste plastic by GC-VUV, Journal of Chromatography A, 1637 (2021) 461837.
[18] M.P. McDaniel, Chapter 3 - A Review of the Phillips Supported Chromium Catalyst and Its Commercial Use for Ethylene Polymerization, in: B.C. Gates, H. Knözinger (Eds.) Advances in Catalysis, Academic Press2010, pp. 123-606.
[19] D.G. Dikobe, A.S. Luyt, Thermal and mechanical properties of PP/HDPE/wood powder and MAPP/HDPE/wood powder polymer blend composites, Thermochimica Acta, 654 (2017) 40-50.
[20] K.S. Kanaga Karuppiah, A.L. Bruck, S. Sundararajan, J. Wang, Z. Lin, Z.-H. Xu, X. Li, Friction and wear behavior of ultra-high molecular weight polyethylene as a function of polymer crystallinity, Acta Biomaterialia, 4 (2008) 1401-1410.
[21] A. Bhattacharya, J.W. Rawlins, P. Ray, Polymer grafting and crosslinking, John Wiley & Sons2008.
[22] N. Salmen, E. Back, The influence of water on the glass transition temperature of cellulose, Tappi, 60 (1977) 137-140.
[23] M.R. Mackley, A. Keller, Flow induced crystallization of polyethylene melts, Polymer, 14 (1973) 16-20.
[24] J. Scheirs, W. Kaminsky, Feedstock recycling and pyrolysis of waste plastics, Chichester, UK; Hoboken, NJ: J. Wiley & Sons2006.
[25] M.L. Poutsma, Reexamination of the Pyrolysis of Polyethylene: Data Needs, Free-Radical Mechanistic Considerations, and Thermochemical Kinetic Simulation of Initial Product-Forming Pathways, Macromolecules, 36 (2003) 8931-8957.
[26] S.E. Levine, L.J. Broadbelt, Detailed mechanistic modeling of high-density polyethylene pyrolysis: Low molecular weight product evolution, Polymer Degradation and Stability, 94 (2009) 810-822.
[27] H.S. Fogler, Elements of Chemical Reaction Engineering, 1999.
[28] R. Prins, A. Wang, X. Li, F. Sapountzi, Introduction to heterogeneous catalysis, World Scientific2022.
[29] V.B. Kazansky, Adsorbed carbocations as transition states in heterogeneous acid catalyzed transformations of hydrocarbons, Catalysis Today, 51 (1999) 419-434.
[30] A. Corma, A.V. Orchillés, Current views on the mechanism of catalytic cracking, Microporous and Mesoporous Materials, 35-36 (2000) 21-30.
[31] S. Kotrel, H. Knözinger, B.C. Gates, The Haag–Dessau mechanism of protolytic cracking of alkanes, Microporous and Mesoporous Materials, 35-36 (2000) 11-20.
[32] F.C. Jentoft, B.C. Gates, Solid-acid-catalyzed alkane cracking mechanisms: evidence from reactions of small probe molecules, Topics in Catalysis, 4 (1997) 1-13.
[33] R. Gounder, E. Iglesia, The catalytic diversity of zeolites: confinement and solvation effects within voids of molecular dimensions, Chemical Communications, 49 (2013) 3491-3509.
[34] J. Hagen, Industrial catalysis: a practical approach, John Wiley & Sons2015.
[35] D.D. Hibbitts, D.W. Flaherty, E. Iglesia, Effects of Chain Length on the Mechanism and Rates of Metal-Catalyzed Hydrogenolysis of n-Alkanes, The Journal of Physical Chemistry C, 120 (2016) 8125-8138.
[36] D.W. Flaherty, D.D. Hibbitts, E.I. Gürbüz, E. Iglesia, Theoretical and kinetic assessment of the mechanism of ethane hydrogenolysis on metal surfaces saturated with chemisorbed hydrogen, Journal of Catalysis, 311 (2014) 350-356.

[37] D.W. Flaherty, E. Iglesia, Transition-State Enthalpy and Entropy Effects on Reactivity and Selectivity in Hydrogenolysis of n-Alkanes, Journal of the American Chemical Society, 135 (2013) 18586-18599.
[38] J. Francis, E. Guillon, N. Bats, C. Pichon, A. Corma, L.J. Simon, Design of improved hydrocracking catalysts by increasing the proximity between acid and metallic sites, Applied Catalysis A: General, 409-410 (2011) 140-147.
[39] M.A. Camblor, A. Corma, A. Martínez, V. Martínez-Soria, S. Valencia, Mild Hydrocracking of Vacuum Gasoil over NiMo-Beta Zeolite Catalysts: The Role of the Location of the NiMo Phases and the Crystallite Size of the Zeolite, Journal of Catalysis, 179 (1998) 537-547.
[40] S. Helmcke, T. Hundertmark, C. Musso, W.J. Ong, J. Oxgaard, J. Wallach, Climate impact of plastics, McKinsey & Company, 2022.
[41] P. Djinović, T. Tomše, J. Grdadolnik, Š. Božič, B. Erjavec, M. Zabilskiy, A. Pintar, Natural aluminosilicates for catalytic depolymerization of polyethylene to produce liquid fuel-grade hydrocarbons and low olefins, Catalysis Today, 258 (2015) 648-659.
[42] R. Bagri, P.T. Williams, Catalytic pyrolysis of polyethylene, Journal of Analytical and Applied Pyrolysis, 63 (2002) 29-41.
[43] Z. Peng, T.J. Simons, J. Wallach, A. Youngman, Advanced recycling: Opportunities for growth, McKinsey & Company, McKinsey & Company, McKinsey & Company, 2022.
[44] I. Vollmer, M.J.F. Jenks, M.C.P. Roelands, R.J. White, T. van Harmelen, P. de Wild, G.P. van der Laan, F. Meirer, J.T.F. Keurentjes, B.M. Weckhuysen, Beyond Mechanical Recycling: Giving New Life to Plastic Waste, Angewandte Chemie International Edition, 59 (2020) 15402-15423.
[45] A. Demirbas, G. Arin, An overview of biomass pyrolysis, Energy sources, 24 (2002) 471-482.
[46] T.W. Walker, N. Frelka, Z. Shen, A.K. Chew, J. Banick, S. Grey, M.S. Kim, J.A. Dumesic, R.C. Van Lehn, G.W. Huber, Recycling of multilayer plastic packaging materials by solvent-targeted recovery and precipitation, Science Advances, 6 (2020) eaba7599.
[47] S.E. Levine, L.J. Broadbelt, Reaction pathways to dimer in polystyrene pyrolysis: A mechanistic modeling study, Polymer Degradation and Stability, 93 (2008) 941-951.
[48] S.C. Kosloski-Oh, Z.A. Wood, Y. Manjarrez, J.P. de los Rios, M.E. Fieser, Catalytic methods for chemical recycling or upcycling of commercial polymers, Materials Horizons, 8 (2021) 1084-1129.
[49] A. Tennakoon, X. Wu, A.L. Paterson, S. Patnaik, Y. Pei, A.M. LaPointe, S.C. Ammal, R.A. Hackler, A. Heyden, I.I. Slowing, G.W. Coates, M. Delferro, B. Peters, W. Huang, A.D. Sadow, F.A. Perras, Catalytic upcycling of high-density polyethylene via a processive mechanism, Nature Catalysis, 3 (2020) 893-901.
[50] I. Vollmer, M.J.F. Jenks, R. Mayorga González, F. Meirer, B.M. Weckhuysen, Plastic Waste Conversion over a Refinery Waste Catalyst, Angewandte Chemie International Edition, 60 (2021) 16101-16108.
[51] J.N. Hahladakis, C.A. Velis, R. Weber, E. Iacovidou, P. Purnell, An overview of chemical additives present in plastics: Migration, release, fate and environmental impact during their use, disposal and recycling, Journal of Hazardous Materials, 344 (2018) 179-199.
[52] L.D. Ellis, N.A. Rorrer, K.P. Sullivan, M. Otto, J.E. McGeehan, Y. Román-Leshkov, N. Wierckx, G.T. Beckham, Chemical and biological catalysis for plastics recycling and upcycling, Nature Catalysis, 4 (2021) 539-556.

[53] A. Parrondo, N.S. Allen, M. Edge, C.M. Liauw, E. Fontán, T. Corrales, Additive interactions in the stabilization of film grade high-density polyethylene. Part I: Stabilization and influence of zinc stearate during melt processing, Journal of Vinyl and Additive Technology, 8 (2002) 75-89.
[54] J.G. Tittensor, R.J. Gorte, D.M. Chapman, Isopropylamine adsorption for the characterization of acid sites in silica-alumina catalysts, Journal of Catalysis, 138 (1992) 714-720.
[55] R.J. Gorte, S.P. Crossley, A perspective on catalysis in solid acids, Journal of Catalysis, 375 (2019) 524-530.
[56] H. Zweifel, R.D. Maier, M. Schiller, Plastics Additives Handbook, 6th ed.2009.
[57] H.E. van der Bij, B.M. Weckhuysen, Phosphorus promotion and poisoning in zeolite-based materials: synthesis, characterisation and catalysis, Chemical Society Reviews, 44 (2015) 7406-7428.
[58] S. Tamiyakul, T. Sooknoi, L.L. Lobban, S. Jongpatiwut, Generation of reductive Zn species over Zn/HZSM–5 catalysts for n–pentane aromatization, Applied Catalysis A: General, 525 (2016) 190-196.
[59] A. Mehdad, R.F. Lobo, Ethane and ethylene aromatization on zinc-containing zeolites, Catalysis Science & Technology, 7 (2017) 3562-3572.
[60] T. Blasco, A. Corma, J. Martínez-Triguero, Hydrothermal stabilization of ZSM-5 catalytic-cracking additives by phosphorus addition, Journal of Catalysis, 237 (2006) 267-277.
[61] J. Valecillos, E. Epelde, J. Albo, A.T. Aguayo, J. Bilbao, P. Castaño, Slowing down the deactivation of H-ZSM-5 zeolite catalyst in the methanol-to-olefin (MTO) reaction by P or Zn modifications, Catalysis Today, 348 (2020) 243-256.
[62] F.-M. Chang, S. Brahma, J.-H. Huang, Z.-Z. Wu, K.-Y. Lo, Strong correlation between optical properties and mechanism in deficiency of normalized self-assembly ZnO nanorods, Scientific Reports, 9 (2019) 905.
[63] M. Wang, L. Jiang, E.J. Kim, S.H. Hahn, Electronic structure and optical properties of Zn(OH)2: LDA+U calculations and intense yellow luminescence, RSC Advances, 5 (2015) 87496-87503.
[64] A. Rahman, G. Lemay, A. Adnot, S. Kaliaguine, Spectroscopic and catalytic study of P-modified ZSM-5, Journal of Catalysis, 112 (1988) 453-463.
[65] N. Comini, T. Huthwelker, J.T. Diulus, J. Osterwalder, Z. Novotny, Factors influencing surface carbon contamination in ambient-pressure x-ray photoelectron spectroscopy experiments, Journal of Vacuum Science & Technology A, 39 (2021) 043203.
[66] F.C.-Y. Wang, Polymer additive analysis by pyrolysis–gas chromatography: IV. Antioxidants, Journal of Chromatography A, 891 (2000) 325-336.
[67] T.N. Pham, V. Nguyen, B. Wang, J.L. White, S. Crossley, Quantifying the influence of water on the mobility of aluminum species and their effects on alkane cracking in zeolites, ACS Catalysis, 11 (2021) 6982-6994.
[68] Y. Ono, Transformation of Lower Alkanes into Aromatic Hydrocarbons over ZSM-5 Zeolites, Catalysis Reviews, 34 (1992) 179-226.
[69] Y. Wang, L. Cheng, J. Gu, Y. Zhang, J. Wu, H. Yuan, Y. Chen, Catalytic Pyrolysis of Polyethylene for the Selective Production of Monocyclic Aromatics over the Zinc-Loaded ZSM-5 Catalyst, ACS Omega, 7 (2022) 2752-2765.
[70] D. Nozik, F.M.P. Tinga, A.T. Bell, Propane Dehydrogenation and Cracking over Zn/H-MFI Prepared by Solid-State Ion Exchange of ZnCl2, ACS Catalysis, 11 (2021) 14489-14506.
[71] X. Liu, S. Liu, Y. Liu, A potential substitute for CeY zeolite used in fluid catalytic cracking process, Microporous and Mesoporous Materials, 226 (2016) 162-168.

[72] N. Kumar, L.E. Lindfors, R. Byggningsbacka, Synthesis and characterization of H-ZSM-22, Zn-H-ZSM-22 and Ga-H-ZSM-22 zeolite catalysts and their catalytic activity in the aromatization of n-butane, Applied Catalysis A: General, 139 (1996) 189-199.
[73] Y. Yuan, R.F. Lobo, Zinc Speciation and Propane Dehydrogenation in Zn/H-ZSM-5 Catalysts, ACS Catalysis, 13 (2023) 4971-4984.
[74] A. Clark, J. Hogan, R. Banks, W. Lanning, Marlex catalyst systems, Industrial & Engineering Chemistry, 48 (1956) 1152-1155.
[75] A.J. Martín, C. Mondelli, S.D. Jaydev, J. Pérez-Ramírez, Catalytic processing of plastic waste on the rise, Chem, 7 (2021) 1487-1533.
[76] R.E. Harmon, G. SriBala, L.J. Broadbelt, A.K. Burnham, Insight into Polyethylene and Polypropylene Pyrolysis: Global and Mechanistic Models, Energy & Fuels, 35 (2021) 6765-6775.
[77] A. Marcilla, M.I. Beltrán, F. Hernández, R. Navarro, HZSM5 and HUSY deactivation during the catalytic pyrolysis of polyethylene, Applied Catalysis A: General, 278 (2004) 37-43.
[78] M.A. Uddin, K. Koizumi, K. Murata, Y. Sakata, Thermal and catalytic degradation of structurally different types of polyethylene into fuel oil, Polymer Degradation and Stability, 56 (1997) 37-44.
[79] G. Manos, A. Garforth, J. Dwyer, Catalytic Degradation of High-Density Polyethylene over Different Zeolitic Structures, Industrial & Engineering Chemistry Research, 39 (2000) 1198-1202.
[80] D.W. Park, E.Y. Hwang, J.R. Kim, J.K. Choi, Y.A. Kim, H.C. Woo, Catalytic degradation of polyethylene over solid acid catalysts, Polymer Degradation and Stability, 65 (1999) 193-198.
[81] Y. Wang, Y. Zhang, H. Fan, P. Wu, M. Liu, X. Li, J. Yang, C. Liu, P. Bai, Z. Yan, Elucidating the structure-performance relationship of typical commercial zeolites in catalytic cracking of low-density polyethylene, Catalysis Today, 405-406 (2022) 135-143.
[82] G. Elordi, M. Olazar, G. Lopez, P. Castaño, J. Bilbao, Role of pore structure in the deactivation of zeolites (HZSM-5, Hβ and HY) by coke in the pyrolysis of polyethylene in a conical spouted bed reactor, Applied Catalysis B: Environmental, 102 (2011) 224-231.
[83] D.P. Serrano, J. Aguado, J.M. Escola, Catalytic Cracking of a Polyolefin Mixture over Different Acid Solid Catalysts, Industrial & Engineering Chemistry Research, 39 (2000) 1177-1184.
[84] D.P. Serrano, J. Aguado, J.M. Escola, J.M. Rodriguez, A. Peral, Catalytic properties in polyolefin cracking of hierarchical nanocrystalline HZSM-5 samples prepared according to different strategies, Journal of Catalysis, 276 (2010) 152-160.
[85] J. Aguado, D.P. Serrano, G.S. Miguel, J.M. Escola, J.M. Rodríguez, Catalytic activity of zeolitic and mesostructured catalysts in the cracking of pure and waste polyolefins, Journal of Analytical and Applied Pyrolysis, 78 (2007) 153-161.
[86] R.J. Conk, S. Hanna, J.X. Shi, J. Yang, N.R. Ciccia, L. Qi, B.J. Bloomer, S. Heuvel, T. Wills, J. Su, A.T. Bell, J.F. Hartwig, Catalytic deconstruction of waste polyethylene with ethylene to form propylene, Science, 377 (2022) 1561-1566.
[87] J.E. Rorrer, C. Troyano-Valls, G.T. Beckham, Y. Román-Leshkov, Hydrogenolysis of Polypropylene and Mixed Polyolefin Plastic Waste over Ru/C to Produce Liquid Alkanes, ACS Sustainable Chemistry & Engineering, 9 (2021) 11661-11666.
[88] A. Thevenon, I. Vollmer, Towards a Cradle-to-Cradle Polyolefin Lifecycle, Angewandte Chemie International Edition, 62 (2023) e202216163.
[89] B.C. Vance, P.A. Kots, C. Wang, J.E. Granite, D.G. Vlachos, Ni/SiO2 catalysts for polyolefin deconstruction via the divergent hydrogenolysis mechanism, Applied Catalysis B: Environmental, 322 (2023) 122138.

[90] V. Busico, R. Cipullo, N. Friederichs, H. Linssen, A. Segre, V. Van Axel Castelli, G. van der Velden, H NMR analysis of chain unsaturations in ethene/1-octene copolymers prepared with metallocene catalysts at high temperature, Macromolecules, 38 (2005) 6988-6996.
[91] Y. He, X. Qiu, J. Klosin, R. Cong, G.R. Roof, D. Redwine, Terminal and internal unsaturations in poly (ethylene-co-1-octene), Macromolecules, 47 (2014) 3782-3790.
[92] T.J. Hermel-Davidock, M. Demirors, S.M. Hayne, R. Cong, Ethylene-based polymer compositions, Google Patents, 2013.
[93] A. Ghorbanpour, A. Gumidyala, L.C. Grabow, S.P. Crossley, J.D. Rimer, Epitaxial Growth of ZSM-5@Silicalite-1: A Core–Shell Zeolite Designed with Passivated Surface Acidity, ACS Nano, 9 (2015) 4006-4016.
[94] A.C. Jerdy, T. Pham, M.Á. González-Borja, P. Atallah, D. Soules, R. Abbott, L. Lobban, S. Crossley, Impact of the presence of common polymer additives in thermal and catalytic polyethylene decomposition, Applied Catalysis B: Environmental, 325 (2023) 122348.
[95] X. Zhou, L.J. Broadbelt, R. Vinu, Chapter Two - Mechanistic Understanding of Thermochemical Conversion of Polymers and Lignocellulosic Biomass, in: K.M. Van Geem (Ed.) Advances in Chemical Engineering, Academic Press2016, pp. 95-198.
[96] R. Althoff, B. Schulz-Dobrick, F. Schüth, K. Unger, Controlling the spatial distribution of aluminum in ZSM-5 crystals, Microporous Materials, 1 (1993) 207-218.
[97] J.A. van Bokhoven, B.A. Williams, W. Ji, D.C. Koningsberger, H.H. Kung, J.T. Miller, Observation of a compensation relation for monomolecular alkane cracking by zeolites: the dominant role of reactant sorption, Journal of Catalysis, 224 (2004) 50-59.
[98] N. Danilina, F. Krumeich, S.A. Castelanelli, J.A. van Bokhoven, Where Are the Active Sites in Zeolites? Origin of Aluminum Zoning in ZSM-5, The Journal of Physical Chemistry C, 114 (2010) 6640-6645.
[99] T. Li, F. Krumeich, M. Chen, Z. Ma, J.A. van Bokhoven, Defining aluminum-zoning during synthesis of ZSM-5 zeolites, Physical Chemistry Chemical Physics, 22 (2020) 734-739.
[100] A. Corma, U. Diaz, V. Fornés, J.M. Guil, J. Martínez-Triguero, E.J. Creyghton, Characterization and Catalytic Activity of MCM-22 and MCM-56 Compared with ITQ-2, Journal of Catalysis, 191 (2000) 218-224.
[101] G. Fleischer, The chain length dependence of self-diffusion in melts of polyethylene and polystyrene, Colloid and Polymer Science, 265 (1987) 89-95.
[102] S.P. Crossley, D.E. Resasco, G.L. Haller, Clarifying the multiple roles of confinement in zeolites: From stabilization of transition states to modification of internal diffusion rates, Journal of Catalysis, 372 (2019) 382-387.
[103] A. Corma, P.J. Miguel, A.V. Orchillés, Can Macroscopic Parameters, Such as Conversion and Selectivity, Distinguish between Different Cracking Mechanisms on Acid Catalysts?, Journal of Catalysis, 172 (1997) 355-369.
[104] A.T. To, D.E. Resasco, Hydride transfer between a phenolic surface pool and reactant paraffins in the catalytic cracking of m-cresol/hexanes mixtures over an HY zeolite, Journal of Catalysis, 329 (2015) 57-68.
[105] P.V. Shertukde, G. Marcelin, G.A. Sill, W. Keith Hall, Study of the mechanism of the cracking of small alkane molecules on HY Zeolites, Journal of Catalysis, 136 (1992) 446-462.
[106] D. Witt, J. Hogan, Double-bond isomerization and hydrogenation in polyethylene with soluble nickel catalysts, Journal of Polymer Science Part A-1: Polymer Chemistry, 8 (1970) 2689-2701.

[107] S. Rejman, I. Vollmer, M.J. Werny, E.T. Vogt, F. Meirer, B.M. Weckhuysen, Transport limitations in polyolefin cracking at the single catalyst particle level, Chemical Science, (2023).
[108] V.S. Minnikanti, L.A. Archer, Entropic attraction of polymers toward surfaces and its relationship to surface tension, Macromolecules, 39 (2006) 7718-7728.
[109] B.B. Sauer, G.T. Dee, Molecular weight and temperature dependence of polymer surface tension: comparison of experiment with theory, Macromolecules, 24 (1991) 2124-2126.
[110] D.G. Legrand, G.L. Gaines, The molecular weight dependence of polymer surface tension, Journal of Colloid and Interface Science, 31 (1969) 162-167.
[111] F. Lemos, F. Ramoˆa Ribeiro, M. Kern, G. Giannetto, M. Guisnet, Influence of lanthanum content of LaHY catalysts on their physico-chemical and catalytic properties: Comparison with CeHY catalysts, Applied Catalysis, 39 (1988) 227-237.
[112] I. Chorkendorff, J.W. Niemantsverdriet, Concepts of modern catalysis and kinetics, John Wiley & Sons2017.
[113] N.M. Briggs, S.P. Crossley, Equilibrium catalyst from a fluidized catalytic cracking unit separated by metal content by using carbon nanotubes and a biphasic system, AIChE Journal, 67 (2021) e17260.
[114] E. Santos, B. Rijo, F. Lemos, M.A.N.D.A. Lemos, A catalytic reactive distillation approach to high density polyethylene pyrolysis – Part 1 – Light olefin production, Chemical Engineering Journal, 378 (2019) 122077.
[115] J. Kijeński, T. Kaczorek, Catalytic degradation of polystyrene-Rapid Communication, Polimery, 50 (2005) 60-63.
[116] Y.-M. Chen, Recent advances in FCC technology, Powder Technology, 163 (2006) 2-8.
[117] A. Corma, G.W. Huber, L. Sauvanaud, P. O'connor, Processing biomass-derived oxygenates in the oil refinery: Catalytic cracking (FCC) reaction pathways and role of catalyst, Journal of Catalysis, 247 (2007) 307-327.
[118] S. Wan, C. Waters, A. Stevens, A. Gumidyala, R. Jentoft, L. Lobban, D. Resasco, R. Mallinson, S. Crossley, Decoupling HZSM-5 catalyst activity from deactivation during upgrading of pyrolysis oil vapors, ChemSusChem, 8 (2015) 552-559.
[119] I. Vollmer, M.J. Jenks, M.C. Roelands, R.J. White, T. van Harmelen, P. de Wild, G.P. van Der Laan, F. Meirer, J.T. Keurentjes, B.M. Weckhuysen, Beyond mechanical recycling: Giving new life to plastic waste, Angewandte Chemie International Edition, 59 (2020) 15402-15423.
[120] H.K. Chau, Q.P. Nguyen, A.C. Jerdy, D.-P. Bui, L.L. Lobban, B. Wang, S.P. Crossley, Role of Water on Zeolite-Catalyzed Dehydration of Polyalcohols and EVOH Polymer, ACS Catalysis, 13 (2023) 1503-1512.
[121] A.C. Jerdy, L. Trevisi, M. Monwar, M.Á. González-Borja, R. Abbott, L. Lobban, S. Crossley, Deconvoluting the roles of polyolefin branching and unsaturation on depolymerization reactions over acid catalysts, Applied Catalysis B: Environmental, (2023) 122986.
[122] T. Degnan, G. Chitnis, P.H. Schipper, History of ZSM-5 fluid catalytic cracking additive development at Mobil, Microporous and Mesoporous materials, 35 (2000) 245-252.
[123] G. Caeiro, P. Magnoux, J. Lopes, F.R. Ribeiro, S. Menezes, A. Costa, H. Cerqueira, Stabilization effect of phosphorus on steamed H-MFI zeolites, Applied Catalysis A: General, 314 (2006) 160-171.
[124] J. Lercher, G. Rumplmayr, Controlled decrease of acid strength by orthophosphoric acid on ZSM5, Applied catalysis, 25 (1986) 215-222.
[125] W.W. Kaeding, S.A. Butter, Production of chemicals from methanol: I. Low molecular weight olefins, Journal of Catalysis, 61 (1980) 155-164.

[126] N. Xue, X. Chen, L. Nie, X. Guo, W. Ding, Y. Chen, M. Gu, Z. Xie, Understanding the enhancement of catalytic performance for olefin cracking: Hydrothermally stable acids in P/HZSM-5, Journal of catalysis, 248 (2007) 20-28.
[127] D.E. Resasco, S.P. Crossley, B. Wang, J.L. White, Interaction of water with zeolites: a review, Catalysis Reviews, 63 (2021) 302-362.
[128] K. Chen, A. Zornes, R. Bababrik, J. Crouch, W. Alvarez, M. Wulfers, D. Resasco, B. Wang, S. Crossley, J.L. White, First-Formed Framework Species and Phosphate Structure Distributions in Phosphorus-Modified MFI Zeolites, The Journal of Physical Chemistry C, 126 (2021) 227-238.
[129] T.N. Pham, V. Nguyen, H. Nguyen-Phu, B. Wang, S. Crossley, Influence of Brønsted Acid Site Proximity on Alkane Cracking in MFI Zeolites, ACS Catalysis, 13 (2023) 1359-1370.